

Spring 1989

Ground-level atmospheric gamma-ray flux measurements in the 1-6 MeV range

Parameswaran Sreekumar
University of New Hampshire, Durham

Follow this and additional works at: <https://scholars.unh.edu/dissertation>

Recommended Citation

Sreekumar, Parameswaran, "Ground-level atmospheric gamma-ray flux measurements in the 1-6 MeV range" (1989). *Doctoral Dissertations*. 1579.
<https://scholars.unh.edu/dissertation/1579>

This Dissertation is brought to you for free and open access by the Student Scholarship at University of New Hampshire Scholars' Repository. It has been accepted for inclusion in Doctoral Dissertations by an authorized administrator of University of New Hampshire Scholars' Repository. For more information, please contact nicole.hentz@unh.edu.

INFORMATION TO USERS

The most advanced technology has been used to photograph and reproduce this manuscript from the microfilm master. UMI films the text directly from the original or copy submitted. Thus, some thesis and dissertation copies are in typewriter face, while others may be from any type of computer printer.

The quality of this reproduction is dependent upon the quality of the copy submitted. Broken or indistinct print, colored or poor quality illustrations and photographs, print bleedthrough, substandard margins, and improper alignment can adversely affect reproduction.

In the unlikely event that the author did not send UMI a complete manuscript and there are missing pages, these will be noted. Also, if unauthorized copyright material had to be removed, a note will indicate the deletion.

Oversize materials (e.g., maps, drawings, charts) are reproduced by sectioning the original, beginning at the upper left-hand corner and continuing from left to right in equal sections with small overlaps. Each original is also photographed in one exposure and is included in reduced form at the back of the book. These are also available as one exposure on a standard 35mm slide or as a 17" x 23" black and white photographic print for an additional charge.

Photographs included in the original manuscript have been reproduced xerographically in this copy. Higher quality 6" x 9" black and white photographic prints are available for any photographs or illustrations appearing in this copy for an additional charge. Contact UMI directly to order.

U·M·I

University Microfilms International
A Bell & Howell Information Company
300 North Zeeb Road, Ann Arbor, MI 48106-1346 USA
313/761-4700 800/521-0600

Order Number 8921940

**Ground level atmospheric gamma ray flux measurements in the
1-6 MeV range**

Sreekumar, Parameswaran, Ph.D.

University of New Hampshire, 1989

U·M·I
300 N. Zeeb Rd.
Ann Arbor, MI 48106

**GROUND LEVEL ATMOSPHERIC GAMMA RAY FLUX
MEASUREMENTS IN THE 1-6 MEV RANGE**

BY

PARAMESWARAN SREEKUMAR

B.Sc., Kerala University, India, 1979

M.Sc., Indian Institute of Technology, Bombay, 1981

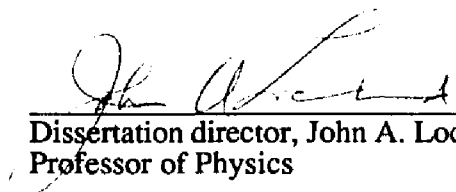
DISSERTATION

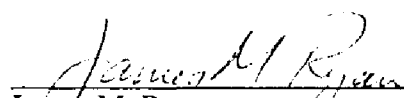
**Submitted to the University of New Hampshire
in Partial Fulfillment of
the Requirements for the Degree of**

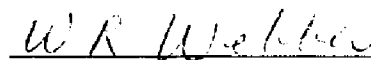
**Doctor of Philosophy
in
Physics**

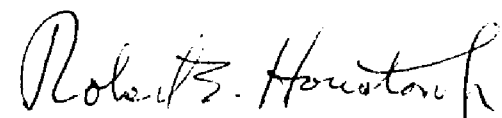
May, 1989


This dissertation has been examined and approved.


Dissertation director, John A. Lockwood
Professor of Physics


James M. Ryan
Research Associate Professor


William R. Webber
Professor of Physics


Robert Houston Jr.
Professor of Physics


Martin A. Lee
Research Professor

1992 1989
Date

ABSTRACT

GROUND LEVEL ATMOSPHERIC GAMMA RAY FLUX MEASUREMENTS IN THE 1-6 MEV RANGE

by

Parameswaran Sreekumar

University of New Hampshire, May, 1989

This thesis deals with the measurement of atmospheric gamma ray flux in the 1-6 MeV range at ground level. These measurements were carried out using a Compton gamma ray telescope, developed at the University of New Hampshire. It utilizes the Compton scattering principle to detect and image gamma ray sources. The telescope was used to measure ground level atmospheric gamma rays at four locations (Leadville (10200 ft), Boulder (5430 ft), Mt. Washington (6072 ft) and Durham (80 ft)) which ranged in atmospheric depth from 720 - 1033 g/cm² and in local cutoff rigidity from 1.4 - 2.9 GV. Data was collected over a two week period at each location during 1987. The results yielded for the first time statistically significant atmospheric gamma ray flux values at large depths in the atmosphere.

The analysis provided differential energy flux (photon/cm²-s-sr-MeV) at various zenith angles (10°-40°) in the 1-6 MeV energy range. The zenith angle dependence of the differential energy flux indicated a $\cos^n \theta$ dependence where $n \approx 2.8$ at higher altitudes (Leadville and Mt. Washington) and $n \approx 2.0$ deeper in the atmosphere (Boulder and Durham). The vertical intensity fitted a power law spectrum of index ≈ 1.2 , with the

spectrum softening at large atmospheric depths. The atmospheric depth dependence shows an e-folding depth of 153 g/cm^2 . Using this depth dependence, all existing measurements below 700 g/cm^2 were normalized to sea level. Good agreement is seen among the normalized sea level flux corresponding to different experiments. Comparing experimental results with existing theoretical and Monte Carlo calculations in the 1-10 MeV range, the measurements indicate a softer power law spectrum, indicating the need to further examine the calculations. Combining UNH results with University of California (Riverside), measurements, indicate a weak rigidity dependence in the vertical atmospheric gamma ray intensity.

*This dissertaion is dedicated to my family
who provided constant encouragement throughout my life.*

ACKNOWLEDGEMENTS

I wish to sincerely thank my thesis advisor Professor John A. Lockwood for his encouragement and guidance throughout this project at the University of New Hampshire as well as his assistance in the preparation of this thesis. I am also extremely grateful to Dr. James M. Ryan who has constantly assisted me with the day to day scientific and experimental aspects of the program. Special thanks to our former electronics engineer Alan Weidknecht for his patience and untiring assistance with the instrumentation and in building my electronics background. Warmest thanks to John Macri, Paul Marshall, Dave Vollmer, Stan Ellis, Paul Vachon, Neil Schönwald, Matt Burke, Jim Jedrey and Matt Loomis who not only assisted technically but also provided a stimulating and entertaining atmosphere during my stay at UNH. Our wide ranging discussions on social, moral and political issues have indeed given me a better understanding of the culture and people of this country. I would like to express my thanks to Dr. George Simpson who was always available to answer my questions, for providing me with the Monte Carlo simulation code which was essential in arriving at the results presented in this work and to Drs. Daniel Morris and Peter von Ballmoos for their help and encouragement during the course of this project. I am grateful to Rita Freuder for all the computational help I received during the early stages of the project and for those wonderful home cooked meals and entertaining times on the squash court. I deeply appreciate the assistance from John Levasseur, the extremely talented Senior Project Machinist of the Space Science Center in the construction of the telescope. To the members of the physics faculty and particularly members of my thesis committee, I extend my gratitude and respect for providing me this experience. Warmest thanks to our librarian Becky Marden for her assistance and cheerful countenance, to the Physics department and the Space Science Center for the financial support and the departmental staff for all their assistance during my stay at UNH.

I express my sincere thanks to my good friends Dr. Alphonse Sterling, Jim Connelly, Ping Ping Chih, Keyun Tang, Dr. Tom Milliman, Dr. Mark McConnell, Dr. Craig Pollock, Renu Saxena, Dipen Bhattacharya and Deb Thomas for their co-operation, encouragement and entertaining companionship during these years at UNH.

I have been away from India for several years and I must sincerely thank my family for their understanding and encouragement in spite of the large physical distance that separated us. I would also like to thank Drs. Tim O'Gorman and Tim Sullivan of the IBM Corporation, Burlington for their help and entertaining company during our data collection trips to Leadville and Boulder and the crew of the Mt. Washington Observatory for the hospitality and assistance with measurements on top of Mt. Washington. Special thanks to Jim Kish and Dave Schrier of Spectra Research Inc. for their assistance with various hardware and software problems.

I would like to thank NASA for their continuing support of this work through grant #NSG-7481 and the IBM for their support through the Shared University Research Project SL149 in completing this project.

List of Tables

Table 2-1 Properties of scintillators.....	28
Table 2-2 Radioactive sources used during efficiency measurements	40
Table 2-3 Telescope efficiency (%) determined from Monte Carlo simulations. These agree to within 10% to efficiency measurements carried out in the laboratory.....	41
Table 3-1 Data on observation sites.....	57
Table 4-1 Radioactive sources used in energy calibration.....	62
Table 4-2 Correction factors used to account for background contributions from K^{40} (1.46 MeV) and Th^{228} (2.61 MeV) lines in the (1-2) and (2-3) MeV energy bins respectively. Corrected flux = correction factor * measured flux.....	76
Table 5-1 Variation of exponent 'n' of $\cos \theta$ angular distribution as a function of atmospheric depth.	85
Table 5-2 Vertical intensity spectral index of atmospheric gamma rays at various depths	86

List of Figures

Fig. 1	Cosmic ray interactions in the atmosphere.....	2
Fig. 1-1	Photoelectric process.....	16
Fig. 1-2	Compton scattering.....	18
Fig. 1-3	Pair production in the field of a nucleus.	21
Fig. 1-4	The mass attenuation coefficient (cm^2/g) for sodium iodide.....	24
Fig. 2-1	Telescope configuration.....	26
Fig. 2-2	Principle of Compton telescope.....	30
Fig. 2-3	The TOF spectra is over a wide energy range of 1-12 MeV and has no PSD selection imposed upon it.....	36
Fig. 2-4	The PSD spectra is over a wide energy range of 1-12 MeV and has no TOF selection imposed upon it.....	37
Fig. 2-5	Telescope efficiency as a function of zenith angle for fixed photon energies. Monte Carlo (MC) results (interpolation line drawn through them) are compared with measured (UNH) efficiencies (20% error in activity).....	43
Fig. 2-6	Telescope efficiency as a function of energy for fixed zenith angles (20 deg). Monte Carlo (MC) results are compared with measured efficiencies (UNH).....	44
Fig. 2-7	Principle of Time of Flight (TOF) measurement.....	51
Fig. 2-8	Timing signals involved with the Track & Hold circuit.....	52
Fig. 2-9	Fast logic layout and data acquisition system.	55
Fig. 4-1	Energy calibration in NE213.....	65
Fig. 4-2	Energy calibration in NaI(Tl).....	66
Fig. 4-3	The energy loss spectrum (E1+E2) without any TOF or PSD selection.....	67

Fig. 4-4 Energy loss spectrum in NE213 and NaI(Tl) along with the summed total energy spectrum (Na ²² source - 1.275 MeV ; 20 degree scatter).....	68
Fig. 4-5 Time of flight calibration setup.....	69
Fig. 4-6 Time of Flight windows for downward(good events) and accidental events.	70
Fig. 4-7 PSD walk correction plot. A quadratic fit is indicated for the all energies except for the smallest D1 energy deposits.....	71
Fig. 4-8 PSD - D1 (energy deposit) scatter plot indicating PSD selection window.....	72
Fig. 4-9 Comparison of energy loss spectrum in the downward TOF window at Boulder (dotted line) and at Mt. Washington (solid line). Enhanced presence of K-40 at Boulder can be clearly observed.....	77
Fig. 4-10 The energy loss spectrum is plotted with and without selection in TOF.....	78
Fig. 4-11 The energy loss spectrum corresponding to events in the upward and downward TOF windows (24 hr run). There are significant differences between the spectral shapes of the two distributions..	79
Fig. 4-12 The energy loss spectrum corresponding to the downward TOF window is fitted using a (polynomial + gaussian) distribution.....	80
Fig. 5-1 Flux integrated over (10-40) degrees uncorrected for K-40 (1-2) MeV and Th-228 (2-3) MeV..	83
Fig. 5-2 Zenith angle dependence (cos ⁿ θ) in the 3-6 MeV range. These can be compared with cos ² θ and sec θ distributions (scale factor A=0.05).....	84

Fig. 5-3 Vertical intensity fitted to a power law using (3-6) MeV data (ref. Table 5-2). Corrected (1-2) and (2-3) MeV bins for K-40 and Th-228.....	87
Fig. 5-4 Vertical intensity measurements at various atmospheric depths (>600 g/cm ²) are plotted together. Least square fit is drawn on calculations of Daniel et al. (1974) (1000 g/cm ²).....	88
Fig. 5-5 Exponential dependence of vertical intensity on atmospheric depth. Attenuation mean free path (g/cm ²) is 145 (3500 keV; 150 (4500 keV) and 127 (5500 keV).....	90
Fig. 5-6 Integrated downward moving gamma ray flux growth curve.....	93
Fig. 5-7 Vertical intensity measurements normalized to sea level. The least square fit is carried out only on calculations of Daniel et al. (1974) at 1000 g/cm ²	94
Fig. 5-8 Comparing normalized vertical intensity measurements (UNH, Ryan, Beuermann) with calculations (Daniel, Morris).....	96
Fig. 5-9 Observed rigidity dependence in the normalized vertical gamma ray intensity is compared with sea level neutron counting rate (Potgieter, 1979). A 25% error is indicated for the UNH-Durham data point to represent uncertainty in efficiency.	99

TABLE OF CONTENTS

DEDICATION	iii
ACKNOWLEDGEMENTS	iv
LIST OF TABLES.....	vi
LIST OF FIGURES.....	vii
ABSTRACT.....	x

CHAPTER	PAGE
INTRODUCTION.....	1
Production of Atmospheric Gamma Rays	3
Interest in Atmospheric Gamma Rays.....	4
Geomagnetic Effects on Cosmic Rays	6
Review of Atmospheric Gamma Ray Measurements	9
1). Experimental Investigations	9
2). Theoretical Calculations.....	11
3). Monte Carlo Simulations	12
1 : GAMMA RAY INTERACTIONS IN MATTER.....	16
Photoelectric Effect	16
Compton Scattering.....	17
Pair production.....	20
2 : DESCRIPTION OF THE TELESCOPE	26
Detection Mechanism.....	29
Principal Telescope Parameters	31
1). Energy Resolution.....	31
2). Angular Resolution.....	33

3). Background Reduction Methods.....	35
a). Time of Flight (TOF) Discrimination.....	35
b). Pulse shape Discrimination (PSD).....	37
c). $\bar{\theta}$ Criterion	38
4). Efficiency of Compton Telescopes.	38
a). Monte Carlo Calculation	39
b). Determination with a Radioactive Source.....	39
Advantages of a Compton Telescope.....	42
Disadvantages of Compton Telescopes	45
Electronics Hardware.....	48
1). Front End Electronics (FEE).....	48
2). Coincidence Circuit.....	49
3). Time of Flight Circuit	50
4). Pulse shape Discrimination Circuit.....	50
5). Track and Hold Circuit.....	52
6). Data Acquisition System.....	53
 3 : ASPECTS OF DATA COLLECTION.....	 56
Leadville, Colorado.....	56
Boulder, Colorado.....	58
Mt. Washington, New Hampshire	59
Durham, New Hampshire	59
 4 : ANALYSIS PROCEDURE.....	 61
Energy Calibration.....	62
1). Energy Calibration of NE213 Detector.....	63
2). Energy Calibration of NaI(Tl) Detector	64
TOF Calibration.....	67

Accidental TOF Event Correction.....	69
PSD Calibration.....	71
Event Selection Criterion.....	73
Observational Difficulties.....	74
5 : RESULTS AND DISCUSSION.....	81
Angular distribution	82
Vertical Intensity	86
Atmospheric Depth Dependence	89
Rigidity Dependence.....	97
CONCLUSIONS.....	100
REFERENCES	103

INTRODUCTION

Atmospheric gamma rays are produced from interaction of primary cosmic rays in the Earth's atmosphere. Primary cosmic rays incident on top of the atmosphere are mostly comprised of protons and alpha particles. They interact with nitrogen and oxygen nuclei present in the atmosphere producing a variety of secondary particles. The secondaries include pions, kaons, nucleons, electrons and photons which emerge from the interaction site at various angles carrying away different amounts of energy. Often an emerging nucleon preserves the direction of the incident proton carrying away approximately one-half of the proton energy. The nucleon mean free path is $\approx 60.3 \text{ g/cm}^2$ (Kelley *et al.*, 1980) and $\approx 44 \text{ g/cm}^2$ for heavier particles. The energetic nucleon undergoes further interactions with the medium including nucleon-nucleon (elastic and inelastic) and nucleon-nuclei interactions, creating more secondary particles and the process is repeated (Figure 1). Thus the secondary population of each particle type builds up rapidly with depth in the atmosphere. The number density soon reaches a maximum at residual atmospheric depths of approximately 100 g/cm^2 , called the Pfozter maximum. Below the Pfozter maximum, the primary cosmic ray particle density and average particle energy decreases rapidly with a consequent reduction in the secondary production rate. In addition, there are various attenuation processes in the medium contributing further to the reduction of the secondary particle flux such as Compton scattering and pair production.

Since the early 1930s it has been observed that cosmic rays at ground level are characterized by an abrupt change in their absorption coefficients as the thickness of the absorber increases. On this basis, ground level cosmic rays were believed to be made up of a *soft* component that is absorbed within 10 cm of lead and a *hard* component that penetrates deeper. Later studies indicate that the *soft* component consists mainly of electrons and photons which in general create lower energy secondary particle showers

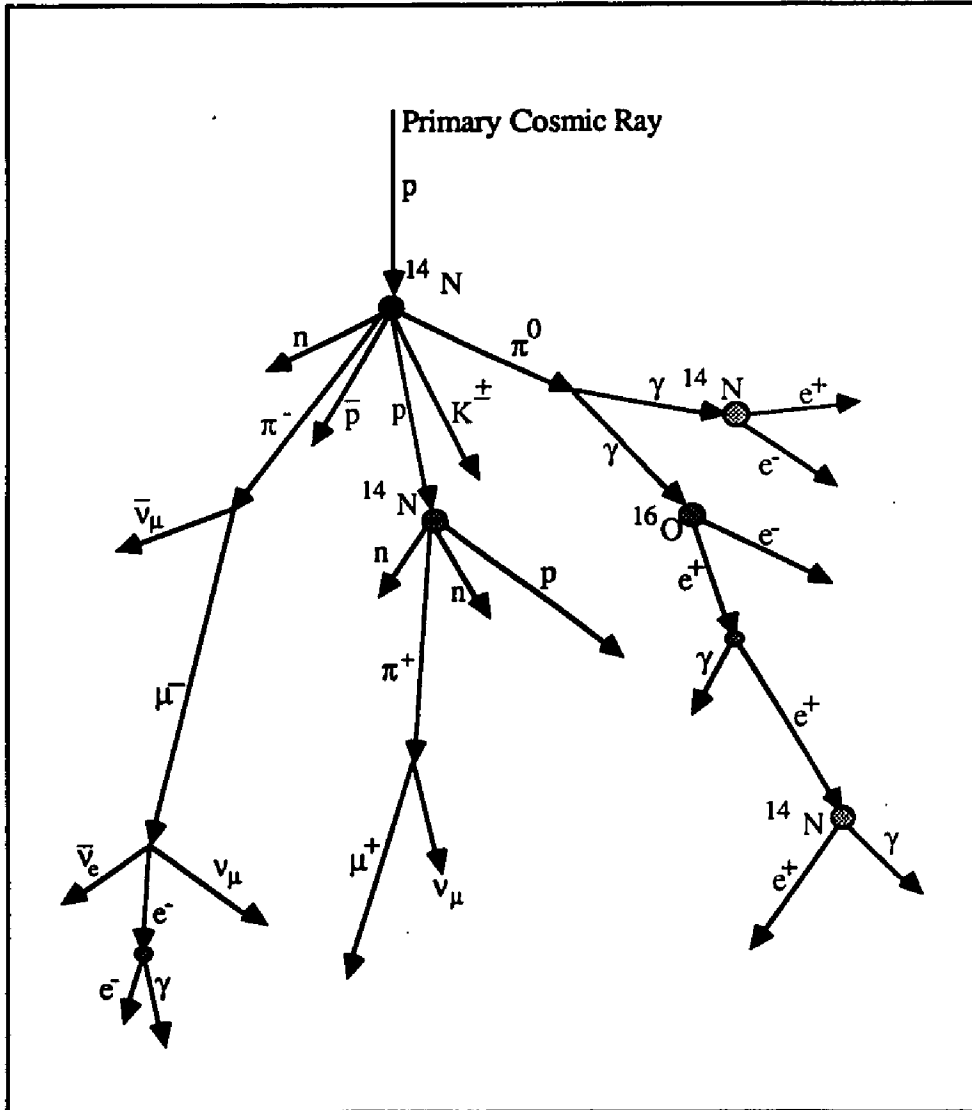


Fig. 1: Cosmic ray interactions in the atmosphere.

within small atmospheric depths with the secondaries emitted at large angles and absorbed rapidly in the medium. The *hard* component is generally composed of nucleons, pions, muons and heavier particles characterized by large interaction mean free paths and by secondary production predominantly in the forward direction. We shall now examine in detail, the processes that lead to the production of secondary photons in the atmosphere.

Production of Atmospheric Gamma Rays

Cosmic rays interacting in the atmosphere produce gamma rays through various mechanisms such as bremsstrahlung, pair annihilation, pion decay, inverse Compton scattering and synchrotron emission. The latter two processes contribute negligibly to the observed atmospheric gamma ray spectrum. Gamma rays from highly excited nuclei or spallation products also seem to produce a negligible contribution (Peterson *et al.*, 1973). Charged and neutral pions emerging from a cosmic ray interaction site are unstable particles which soon decay into more stable states. Neutral pions have a short lifetime of $\approx 1.78 \times 10^{-16}$ s decaying into two photons of energy ≈ 67.5 MeV in the pion rest frame.



These photons initiate electron-photon cascades through pair production Compton scattering and bremsstrahlung. Since atmospheric gamma rays lose energy mostly through Compton scattering or pair production processes, atmospheric electrons and photons in the 1-50 MeV range are closely coupled. At high altitudes and high energies (> 10 MeV) the pion decay contribution to the atmospheric gamma ray spectrum is significant. Contributions from electron/positron bremsstrahlung dominate at lower energies and at atmospheric depths greater than ≈ 600 g/cm² (Morris, 1984). Charged pions decay in flight with a mean half-life of 2.551×10^{-8} s into muons which are less interactive allowing them to reach the deeper regions of the atmosphere.

$$\pi^+ \rightarrow \mu^+ + \nu_\mu$$

$$\pi^- \rightarrow \mu^- + \bar{\nu}_\mu$$

Pion decays are isotropic in the rest frame but in the laboratory frame they emerge generally in the forward direction of the parent particle. Muons lose energy by ionization, undergo bremsstrahlung and eventually decay into electrons or positrons with the emission of neutrinos.

$$\mu^- \rightarrow e^- + \bar{\nu}_e + \nu_\mu$$

$$\mu^+ \rightarrow e^+ + \nu_e + \bar{\nu}_\mu$$

In the muon rest frame they decay with a mean lifetime of 2.2001×10^{-6} s but in the laboratory frame the lifetime is given by $(2.2 \times 10^{-6} \gamma)$ s where $\gamma \equiv (1 - v^2/c^2)^{-1/2}$ is the Lorentz factor for the muon. Thus, time dilation permits energetic muons ($\gamma > 20$) to survive down to sea level. Muons observed at ground level can often be used to monitor cosmic ray intensity at the top of the atmosphere. The decay electrons/positrons are in general emitted in the forward direction of the muon trajectory with the directional correlation becoming less significant at lower energies. They undergo bremsstrahlung producing photons which then soon produce electron-positron pairs and form part of the electron-photon electromagnetic cascade which extending down to sea level. The ground level atmospheric gamma rays in the few MeV range being studied in this work arise primarily from the muon decay electron/positron bremsstrahlung process. Albedo electrons and re-entrant albedo electrons also contribute through the bremsstrahlung process to the atmospheric gamma ray emission but are mostly restricted to the upper atmosphere where the albedo flux is significant.

Interest in Atmospheric Gamma Rays

The study of the atmospheric gamma ray flux as a function of photon energy and incident zenith angle at various atmospheric depths provides an effective means to understand the mechanisms involved in the production of these photons and their

propagation through the atmosphere. The relative contributions from the major production mechanisms such as pion decay, electron bremsstrahlung and albedo electron component can be determined indirectly from the depth dependence of the total gamma ray flux. The atmosphere with its properties and composition being well known, provides us with a good laboratory to carry out this study in detail and will eventually give us an accurate model of cosmic ray interactions in such a medium. This can be important in examining similar astrophysical situations of interest. Energetic cosmic rays produced in supernova explosions interact with the interstellar medium producing various secondary products, cosmic ray interaction with the lunar surface and cosmic rays interacting with giant molecular clouds are examples where this study can be applied and extended to obtain realistic estimates of gamma ray emission from theoretical models.

The study of atmospheric gamma rays have been further motivated by the need to separate the atmospheric contribution of photons from those of astrophysical and solar origin. Gamma ray astronomy in the last twenty years has developed into an exciting area of astrophysical research providing information about some of the most energetic processes in the universe. With the advent of new, improved gamma ray telescopes in recent years, great progress has been made in the study of galactic and extragalactic gamma ray emission. A great majority of these observations were made from balloon platforms which carry instruments to the uppermost regions of the atmosphere. COS-B, SAS-2 and the various Kosmos satellite experiments have also contributed significantly to the rapidly growing wealth of knowledge in this field. The upcoming Gamma Ray Observatory (GRO) satellite due to be launched in April 1990 will carry instruments that cover the entire gamma ray energy range providing simultaneous observations of the celestial sky. This will be a tremendous step in improving our knowledge and understanding of the various processes in our universe. Observations made from balloon platforms are often limited by instrumental background and by the presence of large amounts of atmospheric gamma rays produced locally through cosmic ray interactions. The residual atmosphere of $\approx 3 \text{ gm/cm}^2$

that exists at balloon float altitudes acts as a source of secondary photons. A similar atmospheric component is also observed by satellite experiments carrying gamma ray detectors and is often used as a calibration source. A good estimate of the atmospheric component may improve the minimum detectable flux for gamma ray detectors from extraterrestrial source of gamma rays. The design of Compton telescopes in the early 1970s (Schönfelder *et al.* ,1973, Herzo *et al.* , 1975) was a significant step forward in reducing background contribution in gamma ray telescopes. The problem of atmospheric gamma rays was generally approached using a growth curve generated during the ascent of the instrument on the balloon platform. The principle behind the growth curve technique is that atmospheric gamma rays and primary photons incident at the top of the atmosphere have clearly different dependences on atmospheric depth. The primary gamma ray flux decreases exponentially with depth with a characteristic energy dependent e-folding depth. The atmospheric component is often approximated to grow linearly with depth near float altitudes ($<10 \text{ gm/cm}^2$). Thus the total gamma ray flux measured near the top of the atmosphere can be fitted using the relation

$$R(t) = at + be^{t/\tau}$$

\uparrow
 Atmospheric

\uparrow
 Primary

.....(1)

where τ is the e-folding depth for primary photons in the atmosphere. The depth dependence of atmospheric gamma rays at depths below 10 g/cm^2 is reasonably well understood as a result of various balloon experiments carried out over the years. However, deeper in the atmosphere the dependence is not very well known due to the availability of limited observational data. Hence, it is necessary to obtain information about the intensity of all secondary particle types as a function of energy and angle at all depths in the atmosphere. Our measurements add to the existing data, improving our understanding of the atmospheric gamma ray component.

Geomagnetic Effects on Cosmic Rays

The Earth's magnetic field plays a dominant role in determining the motion of cosmic ray charged particles near the Earth. The force acting on a particle carrying a charge ze in a static magnetic field is given by

$$\frac{d}{dt}(\gamma m_0 \bar{v}) = ze (\bar{v} \times \bar{B}) \quad \dots(2)$$

where γ is the Lorentz factor corresponding to the particle velocity. The particle momentum is usually expressed in terms of rigidity defined as

$$R = \frac{pc}{|ze|} \quad \dots(3)$$

where pc has dimensions of energy (GeV) and R is expressed in gigavolts (GV). For a given magnetic field and pitch angle, the dynamical properties of a charged particle are characterized by its rigidity. Particles with low rigidity are reflected by the field unless they arrive along the magnetic poles, while particles with high rigidity undergo only minor deflection. Thus, 'allowed' and 'forbidden' trajectories exist corresponding to particle rigidity, pitch angle and field configuration.

Three observational effects that are produced by the geomagnetic field on primary cosmic rays are

- 1). Latitude effect
- 2). East-West asymmetry
- 3). North-South anisotropy

Every point on the Earth's surface is characterized by a local vertical cutoff rigidity which defines the minimum rigidity of particles that can arrive vertically at this location. The cutoff rigidity is a function of the geomagnetic latitude (λ), with the rigidity decreasing with increasing latitude.

$$R(\lambda) = 14.9 \cos^4 \lambda (1 + 0.018 \sin \lambda)^2 \text{ GV} \quad (\text{Thompson, 1973}) \quad \dots(4)$$

This directly translates into larger cosmic ray intensities at lower energies at locations of high geographic latitudes.

The East-West effect arises primarily from the fact that cosmic rays are mostly composed of positively charged particles. From equation (1) it can be seen that the Lorentz force act in opposite directions for positive and negative charges. Thus, there is a significantly larger number of cosmic ray primaries incident on the atmosphere from West than from East giving rise to East-West asymmetry. This effect is most pronounced at the equator where the magnetic field is aligned parallel to the Earth's surface.

The cutoff rigidity at any location depends on the particle arrival direction. In the northern hemisphere the cutoff rigidity is smaller at northern locations and larger at southern locations relative to the local vertical cutoff value. This implies more primary cosmic rays enter the atmosphere at northern locations. Consequently, at any location in the northern hemisphere there is a larger secondary particle flux arriving from the North than from the South, giving rise to the North-South anisotropy and vice-versa in the southern hemisphere. A 6% anisotropy in the North-South direction was reported by Fishman *et al.* (1976) at energies above 500 keV. Ryan *et al.* (1979) found a northward anisotropy of 4% in the energy range 2-10 MeV and a depth of 4 gm/cm² while O'Neill (1987) using the same telescope reported similar results from the southern hemisphere.

The geomagnetic effects influencing primary cosmic rays are also observed in the secondaries. These effects become weaker as the average secondary particle energy decreases with atmospheric depth and scattering processes isotropize the distribution. The decrease in the latitude effect with depth in the atmosphere was shown by various secondary measurements including ground level neutron measurements by Potgieter *et al.* (1979). At sea level, we do not expect to measure any of the above mentioned features unambiguously but interestingly, our gamma ray measurements seem to indicate a weak latitude dependence.

Review of Atmospheric Gamma Ray Measurements

Several measurements of atmospheric gamma rays in the MeV region have been performed (Vette, 1962; Chupp *et al.*, 1967; Beuermann *et al.*, 1968; Apparao *et al.*, 1968; Fichtel *et al.*, 1969; Kasturirangan *et al.*, 1972; Peterson *et al.*, 1973; Schönfelder and Lichti (1975); Ryan *et al.*, 1979). These measurements have been complimented by theoretical investigations (Puskin, 1970; Beuermann, 1971; Daniel and Stephens, 1974; Ling, 1975) and Monte Carlo simulations (Thompson, 1974; Morris, 1981). An overwhelming majority of these studies were carried out at small atmospheric depths and at high energies. Our work at UNH provides useful gamma ray data at low energies and large atmospheric depths and can be used to improve existing models. Some of these investigations are briefly discussed below.

Experimental Investigations

Attempts were made in the early as 1960s to detect and understand gamma rays resulting from cosmic ray interactions in the atmosphere. Unfortunately, these early experiments only provided count rate spectra due to complications that arose in determining good detector response functions. One of earliest experiments to detect low energy atmospheric gamma rays was carried out by Vette (1962) using two NaI(Tl) crystals (one with lead shielding) in the energy range of 25-1060 keV. The unshielded detector indicated an e-folding depth of 163 g/cm² from the count rate spectrum. Chupp *et al.* (1967) used a CsI gamma ray spectrometer to conduct a series of experiments to study the time variation of atmospheric 0.511 MeV annihilation line at small depths. They made no attempt to separate the extraterrestrial and atmospheric components from the continuous energy loss spectra. Measurements on secondary electron and photon spectra deeper in the atmosphere (Mt. Zugspitze: 760 g/cm²: 4.5GV; Garmisch-Partenkirchen: 955 g/cm²: 4.5GV) were conducted by Beuermann and Wibberenz (1968) using an ionization spectrometer over an energy range extending from 12 MeV to a few GeV in the vertical direction. The angular

distribution was determined by inclining the telescope axis with respect to the vertical. For energies above 100 MeV, they found that the zenith angle (θ) distribution for electrons and photons obeyed a $\cos \theta$ law. It is interesting to point out that, Beuermann and Wibberenz obtained angular distributions that were similar for electrons and photons with the intensity of both components decreasing with increasing zenith angles. Peterson *et al.* (1973) used a NaI crystal with an anticoincidence shield to study atmospheric gamma rays in the 0.2-10 MeV range. Counting rate spectra were obtained down to a depth of 350 g/cm² with an e-folding length of 180 g/cm² below the Pftzler maximum. However, the photon attenuation mean free path measured by Apparao *et al.* (1968) was 247 g/cm² for 1-5 MeV gamma rays between 400 and 700 millibars. In most of these cases, serious difficulties often arose with the problem of partial energy absorption in the detector. In the high energy range ($E > 50$ MeV) Staib *et al.* (1974) carried out observations from balloon altitudes (3 millibars) at 4.5 GV and 12 GV and at sea level (200 m; cutoff rigidity 1.7 GV) using a spark chamber. At float altitudes they obtained a spectral shape steeper than that predicted by Beuermann (1971) in the 10-1000 MeV range with the measured intensity at 100 MeV being larger by a factor of 2. It was suggested that the difference occurs probably from uncertainties in the pion production spectrum and albedo intensity in Beuermann's calculation. The angular distribution obtained (for $E > 50$ MeV) was fitted using a $\sum_{n=1}^{\infty} \cos n\theta$ series function where n goes from 1 to 5. Measurements using a double Compton telescope (1.5-10 MeV) by the MPI group (Schönfelder and Lichti, 1973) succeeded in reducing general background events and carrying out directional imaging at MeV energies but was troubled by the presence of neutron activation in the organic scintillators. The best experimental estimates to date of low energy gamma ray flux at all atmospheric depths were produced by the UCR Compton telescope experiment (Ryan *et al.*, 1979). They also obtained the zenith angle dependence over various depths in the atmosphere. The earliest study on the rigidity dependence of atmospheric 0.511 MeV line was carried out by Kasturirangan *et al.* (1972) when they observed a decrease in the flux by a factor of 9 from 1.3GV to 16.9GV cutoff

rigidity at 6 g/cm^2 . They found a similar variation in the continuum atmospheric gamma ray flux. Golenetskiy *et al.* (1975) using measurements from the Kosmos 461 satellite reported an exponential dependence in the continuum given by $\exp(R/85)$ in the energy range of 28 keV to 4.1 MeV over a rigidity range of 3-17.5 GV.

Theoretical Calculations

Beuermann (1971) developed the first atmospheric gamma ray production and propagation model which included energy dependent cross sections for particle interaction and contributions from primary and reentrant albedo electrons. The calculations were restricted to energies above 4 MeV and atmospheric depths below 400 g/cm^2 and included bremsstrahlung and pion decay as the major interaction processes. The results indicated that electron bremsstrahlung contributions were large enough to mask the pion decay peak at $\approx 68 \text{ MeV}$ in the energy spectrum. Calculations by Daniel and Stephens (1974) were an improvement over Beuermann's in many respects. The significant changes were that Daniel and Stephens did not treat bremsstrahlung as a continuous process and allowed Compton interactions a greater role at lower gamma ray energies and large atmospheric depths. The calculation was carried out by solving simultaneously diffusion equations for various secondaries (electrons, positrons and photons), primaries (electrons and positrons) and reentrant electrons and positrons at a given atmospheric depth. The primary electron spectrum used as input was based on electron observations made by Daniel and Stephens (1970). The model provided a complete estimate of the secondary soft cosmic ray flux at various energies and rigidities. The calculations were made for the period of minimum solar activity period. The case of maximum solar activity was examined only at zero cutoff rigidity. The calculations indicate that spectral shape of electrons and photons become nearly the same around 100 g-cm^{-2} but at large depths, the low energy spectra deviate considerably from each other. They also concluded that the angular dependence is similar for electrons and photons at large atmospheric depths. Using an isotropic source function

determined from measured flux, Ling (1975) produced the only theoretical calculations of zenith angle distribution at low energies (0.3-10 MeV) and large depths (0-500 g/cm²) at $\lambda = 40^\circ$. The model failed to reproduce the observed peak in the angular distribution near horizon at float altitudes which is partly explained by the assumption of an isotropic source function.

Model calculations by Beuermann (1971) and Daniel and Stephens (1974) can be closely compared near float altitudes with the large number of measurements made at small atmospheric depths. The results of calculations by Graser *et al.* (1977) in the 4-10 MeV energy range at float altitudes are larger than Beuermann's (1971) results by a factor of 2.5 while they are larger than Daniel and Stephens (1974) predictions by a factor of 7-30, depending on the photon energy in the 1-10 MeV range. Graser *et al.* (1977) suggests that, the albedo electron flux used by Daniel and Stephens is ≈ 7 times lower than that used in their calculation and could partly explain the difference. The incorrect estimates of Daniel and Stephens albedo electron flux should not influence their results at large atmospheric depths where the albedo electron contribution is negligible. However, it needs to be emphasized that models of atmospheric gamma ray production have yet to attain very good agreement with measurements even at float altitudes where significant amount of study has already been carried out.

Monte Carlo Simulations

With the availability of improved particle interaction cross sections from accelerators and faster computers, simulation models using Monte Carlo techniques have made significant advancement in our attempts to understand the role of various production and attenuation processes in our atmosphere. The energy spectrum of atmospheric gamma rays in the range 0.3-10 MeV at small atmospheric depths (3.5 millibars) and at latitude \approx

42° was calculated by Puskin (1970) from the measured particle intensity as a function of depth and he found electron bremsstrahlung to be a dominant source of low energy photons. Thompson (1974) carried out three dimensional Monte Carlo calculations of high energy gamma ray production in the atmosphere at all atmospheric depths and energies greater than 30 MeV. The downward moving photons exhibit a steeper energy spectrum with increasing depth. The most recent calculations were carried out by Morris (1984) who extended Thompson's model down to 10 MeV and also included particle azimuth information. A new computer model was incorporated to simulate high energy nucleon-nuclei interactions. The results of the calculation are in reasonable agreement with the observations near the Pfozter maximum. Upward flux estimates are larger than that observed with the discrepancy increasing with atmospheric depth. The predicted intensity also falls more rapidly with depth when compared with the results published by Ryan *et al.* (1979). Zenith angle dependence were estimated at high altitudes but, no estimates were made deeper in the atmosphere. No predictions on the rigidity dependence of atmospheric gamma rays were made since the model does not incorporate geographical variations in cutoff rigidity.

The work presented here, deals with the study of low energy atmospheric gamma rays at sea level and at mountain altitudes. It attempts to improve upon the results of Ryan *et al.* (1979) measurements with a similar instrument but with a statistically enhanced dataset in the deepest regions of the atmosphere. The measurements were carried out in the 1-12 MeV region using a Compton gamma ray telescope which provides good background suppression and directional sensitivity. Slow muons that are stopped in the lower detector and are hence not vetoed out contribute significantly to the measured flux beyond 7 MeV. Thus, the data presented here is restricted to observations in the energy range of 1-6 MeV. The details of the UNH Compton telescope is described in chapter 2 along with an outline of the associated electronics and data acquisition system. The telescope is of a simple

design with an upper NE213A detector and a lower NaI(Tl) crystal with a large plastic detector placed below to act as an anti-coincidence unit. The telescope provides good energy resolution of $\approx 17\%$ at an energy of 1.275 MeV and a scatter angle of 25° and angular resolution of 7.5° at 3 MeV and 20° scatter. The data acquisition system is designed to be rugged and flexible for modifications with customized cards that provided specific functions. An IBM XT personal computer forms the control and real time data display system and data storage. The complete system was built to be portable and easy to assemble.

Ground level atmospheric gamma ray data were collected at four locations around the country viz., Leadville (10,200 ft), Boulder (5430 ft), Mt. Washington (6200 ft) and Durham (80 ft) over two week periods at each location during 1987. The details of data collection stations are summarized in chapter 3 (table 3-1). Measurements were carried out inside shelters with minimal overhead material which would attenuate or scatter photons. The data analysis procedure is discussed in detail in chapter 4. The energy calibration was carried out using radioactive sources. Calibration of the NaI(Tl) crystal was straightforward while the liquid scintillator cell required some extrapolation using studies by Dietze *et al.* (1982) to determine a proper conversion of pulse height to energy deposit. The procedure used to select time of flight (TOF) and pulse shape discrimination (PSD) windows are also discussed. These parameters are crucial in the event selection criterion imposed on all accepted telescope events. The results from the four ground stations are reduced to integral and differential intensities and are presented in chapter 5. The angle dependence of the differential data is fitted using a $\cos^n\theta$ function. Our angular dependence is used to determine the vertical incident differential gamma ray flux at each location. Using the vertical intensity estimates at all four sites, the atmospheric depth dependence is determined. Normalizing all existing atmospheric gamma ray data (depth $> 600 \text{ g/cm}^2$) to sea level facilitates comparison of calculated (simulations & numerical calculations) results with existing measurements. Finally, the UNH data along with measurements by Ryan *et*

al. (1979) are used to examine any rigidity dependence of the vertical gamma ray intensity. Since the normalized vertical intensity was found to increase slightly at lower rigidities, it is concluded that the data indicate a weak dependence within the limits of the data.

CHAPTER 1

GAMMA RAY INTERACTIONS IN MATTER

Gamma rays interact with matter primarily through these following processes.

- 1). photoelectric absorption
- 2). Compton scattering
- 3). pair production

In the photoelectric and pair production processes the photon is completely eliminated while Compton scattering degrades the incident photon energy. The theories underlying these processes are extensively treated in various textbooks (e.g. Evans, 1955). The salient features can be summarised as follows.

Photoelectric Effect

Photoelectric effect occurs when an incident photon is completely absorbed by a bound electron in an atom. A photon cannot undergo absorption by a free electron since it violates the principle of simultaneous conservation of energy and momentum. The photon

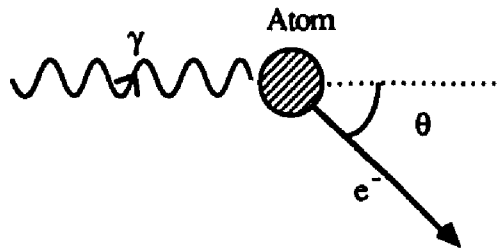


Fig. 1-1 Photoelectric process.

energy is transferred to the electron which subsequently escapes (Figure 1-1) with a kinetic energy given by

$$(K.E.)_e = E_\gamma - \Phi \quad \dots(1-1)$$

where Φ is the work function or binding energy associated with the electron. Thus there is a minimum photon energy given by Φ , below which there will be no electron emission. The liberated electron quickly loses its energy in the medium primarily through ionization. The probability for a photon to undergo photoelectric effect is a strong function of the atomic number of the medium. The photoelectric cross-section (in units of cm^2/atom) can be expressed as (Hayakawa, 1969),

$$\sigma_{\text{photo}} = \sigma_{\text{Th}} \frac{3}{2} Z^5 \alpha^4 \left(\frac{m_0 c^2}{E_\gamma} \right)^5 (\gamma^2 - 1)^{3/2} \left\{ \frac{4}{3} + \frac{\gamma(\gamma-2)}{\gamma+1} \left[1 - \frac{1}{2\gamma\sqrt{\gamma^2-1}} \ln \left(\frac{\gamma+\sqrt{\gamma^2-1}}{\gamma-\sqrt{\gamma^2-1}} \right) \right] \right\} \quad \dots(1-2)$$

where $\gamma = (1-\beta^2)^{-1/2} = \frac{E_\gamma + m_0 c^2}{m_0 c^2}$; $\alpha = \frac{1}{137}$ is the fine structure constant

$$\sigma_{\text{Th}} = \frac{8\pi}{3} r_e^2 = 6.65 \times 10^{-25} \text{ cm}^2 \quad \text{is the Thomson scattering cross-section, } Z \text{ is}$$

the atomic number of the medium and $m_0 c^2$ is the electron rest mass.

Compton Scattering

In a Compton scattering process, an incident photon undergoes scattering with a loosely bound electron in an atom. It is assumed that the electron binding energy is small compared to the energy of the incident photon. The emerging scattered photon suffers a loss in energy as well as a change in the direction while the electron gains kinetic energy. The scattering process is illustrated in Figure 1-2. The plane containing the incident and scattered photon define the scattering plane. Since there is zero momentum normal to this plane, the scattered electron must also lie within the same scattering plane. Photon polarization does not influence the coplanar nature of

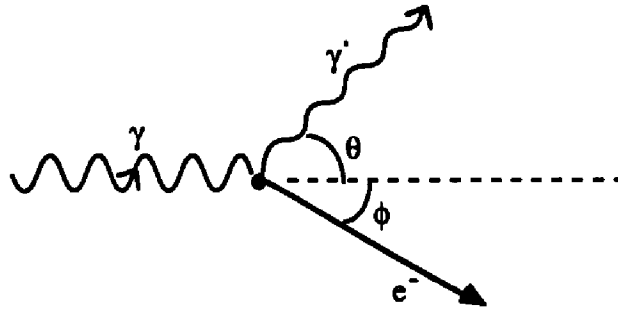


Fig. 1-2 Compton scattering.

momentum distribution (Evans, 1955). The scattered electron energy is given by

$$E_e = \frac{E_\gamma}{1 + \frac{m_0 c^2}{E_\gamma (1 - \cos\theta)}} \quad \dots(1-3)$$

where θ is the photon scatter angle and m_0 is the electron rest mass. The scattered photon energy is given by

$$E_{\gamma'} = E_\gamma - E_e \quad \dots(1-4)$$

It is of interest to note that the shift in the wavelength between the scattered and incident photon, as expressed by

$$\lambda' - \lambda = \frac{h}{m_0 c^2} (1 - \cos\theta) = \lambda_c (1 - \cos\theta) \quad \dots(1-5)$$

is independent of incident photon energy. Here $\lambda_c = 2.426 \times 10^{-10}$ cm is called the Compton wavelength. The maximum energy that can be transferred to the electron is obtained when $\theta = 180^\circ$.

$$E_{e_{\max}} = \frac{E_\gamma}{1 + \frac{m_0 c^2}{2E_\gamma}} \quad \dots(1-6)$$

Scatter angles θ and ϕ are related to each other as

$$\cot \phi = \left(1 + \frac{E_\gamma}{m_0 c^2}\right) \left(\frac{1 - \cos \theta}{\sin \theta}\right) = \left(1 + \frac{E_\gamma}{m_0 c^2}\right) \tan \frac{\theta}{2} \quad \dots(1-7)$$

The relativistic treatment of Compton scattering yields the Klien-Nishina differential cross section formula. For the case of linearly polarized incident photons, the differential scattering cross section is given by,

$$\frac{\partial \sigma}{\partial \Omega} = r_e^2 \frac{1}{[1 + \Gamma(1 - \cos \theta)]^2} \left\{ \sin^2 \xi + \frac{\Gamma^2 (1 - \cos \theta)^2}{2[1 + \Gamma(1 - \cos \theta)]} \right\} \quad \dots(1-8)$$

where $\Gamma \equiv \frac{E_\gamma}{m_0 c^2}$

and ξ is the angle between the electric field vector of incident photon and scattered photon direction (Evans, 1955). The cross section is a maximum when $\xi = 90^\circ$ i.e., when the electric field vector of the incident photon is normal to the scattering plane. So there is greater probability for the scattered photon and electron tend to be ejected at right angles to the electric field vector of the incident polarized photon. Photon polarizations at MeV energies have always been difficult to detect and measure. The dependence of the differential cross section on the scattered photon direction can be used to measure the polarization of gamma ray photons. The upcoming COMPTEL experiment on the Gamma Ray Observatory satellite plans to use this principle in studying photon polarization at gamma ray energies. For the case of unpolarized photons, the differential cross section for collision is given by the expression,

$$\frac{\partial \sigma}{\partial \Omega} = \frac{1}{2} r_e^2 \frac{1 + \cos^2 \theta}{[1 + \Gamma(1 - \cos \theta)]^2} \left\{ 1 + \frac{\Gamma^2 (1 - \cos \theta)^2}{(1 + \cos^2 \theta)[1 + \Gamma(1 - \cos \theta)]} \right\} \quad \dots(1-9)$$

Integrating over all solid angles, one obtains the total cross section for Compton scattering (in units of cm²/electron) as,

$$\sigma_{\text{Compton}} = 2\pi r_e^2 \left\{ \frac{1+\Gamma}{\Gamma^2} \left[\frac{2(1+\Gamma)}{1+2\Gamma} - \frac{1}{\Gamma} \ln(1+2\Gamma) \right] + \frac{1}{2\Gamma} \ln(1+2\Gamma) - \frac{1+3\Gamma}{(1+2\Gamma)^2} \right\} \dots(1-10)$$

It is significant to note that the Compton cross-section is independent of atomic number Z of medium. In the non relativistic limit, the Compton cross-section reduces to the Thomson cross-section. The cross-section has an angular dependence which is a function of photon energy. At low energies, the cross-section is similar in the forward and backward scattering directions. At higher energies the forward scattering cross-section increases at the expense of backward angles and becomes strongly peaked in the forward direction at larger photon energies.

Pair production

As the photon energy exceeds 1022 keV the process of pair production begins and becomes increasingly important with energy. The gamma ray photon materializes into an electron and a positron (Figure 1-3). This process takes place only in the presence of a third particle like a nucleus in order to simultaneously conserve energy and momentum.

$$h\nu = m_0c^2 + m_0c^2 + T_e + T_{e^+} \dots(1-11)$$

where T_e and T_{e⁺} are the kinetic energies associated with the electron and positron respectively. The angular distribution of the emitted electron and positron are generally in the forward direction for an incident photon of high energy, the emphasis being less marked at lower photon energies.

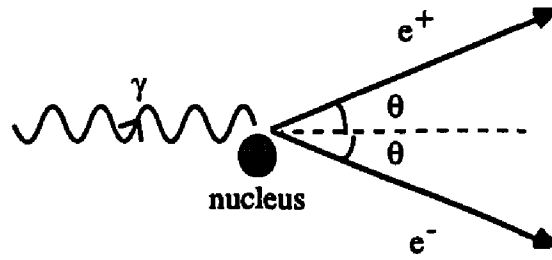


Fig. 1-3 Pair production in the field of a nucleus.

The differential cross section for the creation of a positron of kinetic energy T_+ (and an electron of energy $E_\gamma - 2m_0c^2 - T_+$) is given by

$$\frac{\partial \sigma_{\text{pair}}}{\partial T_+} = \alpha r_e^2 Z^2 \frac{P}{E_\gamma - 2m_0c^2} \quad (\text{Evans, 1955}) \dots (1-12)$$

where P is a dimensionless quantity, depending on E_γ and Z . Analytical integration of the above expression is possible for the extreme relativistic cases to obtain total pair production cross section.

For $m_0c^2 \ll E_\gamma \ll 137m_0c^2Z^{-1/3}$,

$$\sigma_{\text{pair}} = r_e^2 4\alpha Z^2 \left(\frac{7}{9} \ln 2\Gamma - \frac{109}{54} \right) \dots (1-13)$$

For $E_\gamma \gg 137m_0c^2Z^{-1/3}$,

$$\sigma_{\text{pair}} = r_e^2 4\alpha Z^2 \left[\frac{7}{9} \ln (183Z^{-1/3}) - \frac{109}{54} \right] \dots (1-14)$$

It can be seen from (1-14) that at very high energies the cross section is independent of photon energy. The pair production cross section rises monotonically from zero at threshold of 1022 keV, increasing with photon energy. For high Z material, it levels off near 50 MeV and at higher energies for low Z materials.

Each of these processes has different probabilities for interaction at any given energy and each dominates at different energies. In NaI(Tl) the photoelectric absorption dominates below 250 keV while at higher energies the Compton scattering cross-section increases and remains dominant until around 7 MeV when pair production cross-section takes over (Figure 1-4). In our energy range of interest viz., 1-6 MeV the Compton scattering cross-section dominates and a Compton telescope is suitable for detection of these gamma rays. It is important to note that the three processes have different dependences on the atomic number Z of the medium.

$$\begin{aligned}\sigma_{\text{photo}} &\propto Z^5 && \text{cm}^2/\text{atom} \\ \sigma_{\text{Compton}} &\propto Z^0 && \text{cm}^2/\text{electron} \quad \dots(1-15) \\ \sigma_{\text{pair}} &\propto Z^2 && \text{cm}^2/\text{atom}\end{aligned}$$

A gamma ray photon traversing a medium could undergo any one of these interaction depending upon the various cross-sections or any combination of these processes in the case of multiple interactions. The attenuation of the incident beam is given by

$$I = I_0 e^{-\mu x} \quad \dots(1-16)$$

where μ_1 is the linear attenuation coefficient characteristic of the interaction process. The attenuation coefficients for various processes are related to the cross sections as shown below.

$$\begin{aligned}\mu_{\text{photo}} &= \sigma_{\text{photo}} n && (\text{cm}^{-1}) \\ \mu_{\text{Compton}} &= \sigma_{\text{Compton}} nZ && (\text{cm}^{-1}) \quad \dots(1-17) \\ \mu_{\text{pair}} &= \sigma_{\text{pair}} n && (\text{cm}^{-1})\end{aligned}$$

where n is the number density of atoms in the medium. The total attenuation coefficient at any given energy is the linear sum of the individual attenuation coefficients associated with each of these three processes.

$$\mu_1 = \mu_{\text{photo}} + \mu_{\text{Compton}} + \mu_{\text{pair}} \quad (\text{cm}^{-1}) \dots\dots(1-18)$$

The mass attenuation coefficient is defined as

$$\mu_m = \frac{\mu_1}{\rho} \quad (\text{g/cm}^2) \dots\dots(1-19)$$

where ρ is the density of the medium. μ_m allows easy comparison of attenuation properties of gamma rays in various materials since they are independent of actual density and physical state of the material. The mass attenuation coefficients corresponding to different materials is extensively listed in various books (Hubbell, 1969).

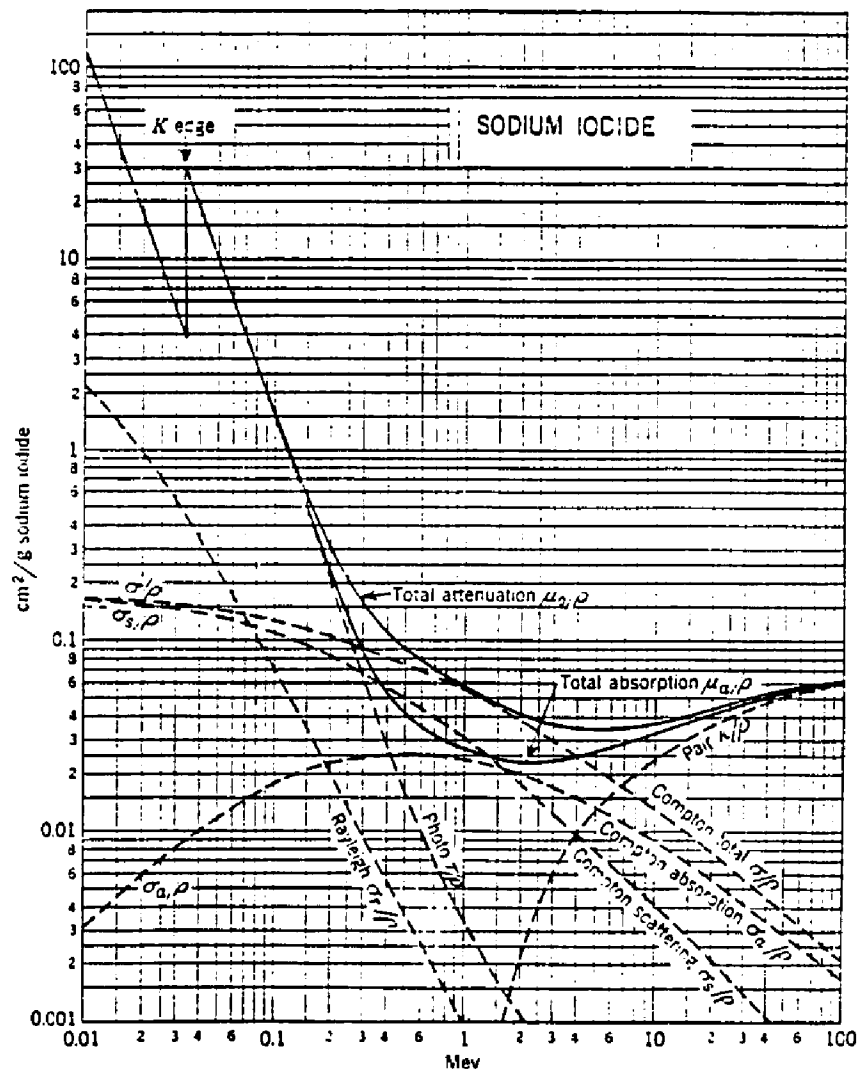


Fig. 1-4 : Mass attenuation coefficient (cm²/g) for sodium iodide. (From R.D. Evans 'The atomic nucleus', 1955; reproduced with permission from McGraw-Hill publishing company).

CHAPTER 2

DESCRIPTION OF THE TELESCOPE

The UNH Compton gamma ray telescope consists of an upper detector (D1), 28 cm in diameter and 8.5 cm thick, filled with liquid scintillator NE213A and a lower NaI(Tl) crystal (D2), 10 inches in diameter and 5 inches thick. The two detectors are separated center to center by a distance of 102 cm (Figure 2-1). A large plastic scintillator, 44 cm in diameter and 11 cm thick made of NE102, acts as a veto shield and is placed below the NaI(Tl) detector.

The organic scintillator NE213A is a pseudocumene (1,2,4 Tri Methylbenzene $(\text{CH}_3)_3\text{C}_6\text{H}_3$) based liquid with a hydrogen to carbon ratio of 1.213. NE213A is made of low Z materials and has the chemical composition $\text{H} : \text{C} : \text{O} : \text{N} = 1 : 0.82 : 2.5 \times 10^{-4} : 2.5 \times 10^{-4}$. It has good timing characteristics with a decay time of about 3.6 ns. The detector is viewed by eight photomultiplier tubes (EMI D363B) and works on the Anger camera principle. This differs from the commonly used array of independent detector cells, each viewed by a PMT where the minimum spatial resolution is equal to the physical dimensions of the cell. An Anger camera on the other hand, provides a large detector volume viewed by fewer PMTs and imposes no intrinsic restriction on the spatial resolution that can be achieved within the detector volume. The scintillators respond to both charged particles, neutrons and photons. Relativistic charged particles lose energy through ionization at a rate of ≈ 2 MeV per cm in the scintillator. In the presence of large charged particle background, as is the case at the top of the atmosphere, these events can be rejected if anti-coincidence shields surround the scintillator. Photons in the MeV range mostly deposit energy via Compton scattering of the orbital electrons in the scintillator. The scintillator is sensitive to neutrons due to presence of hydrogen. The neutrons scatter off hydrogen nuclei resulting in

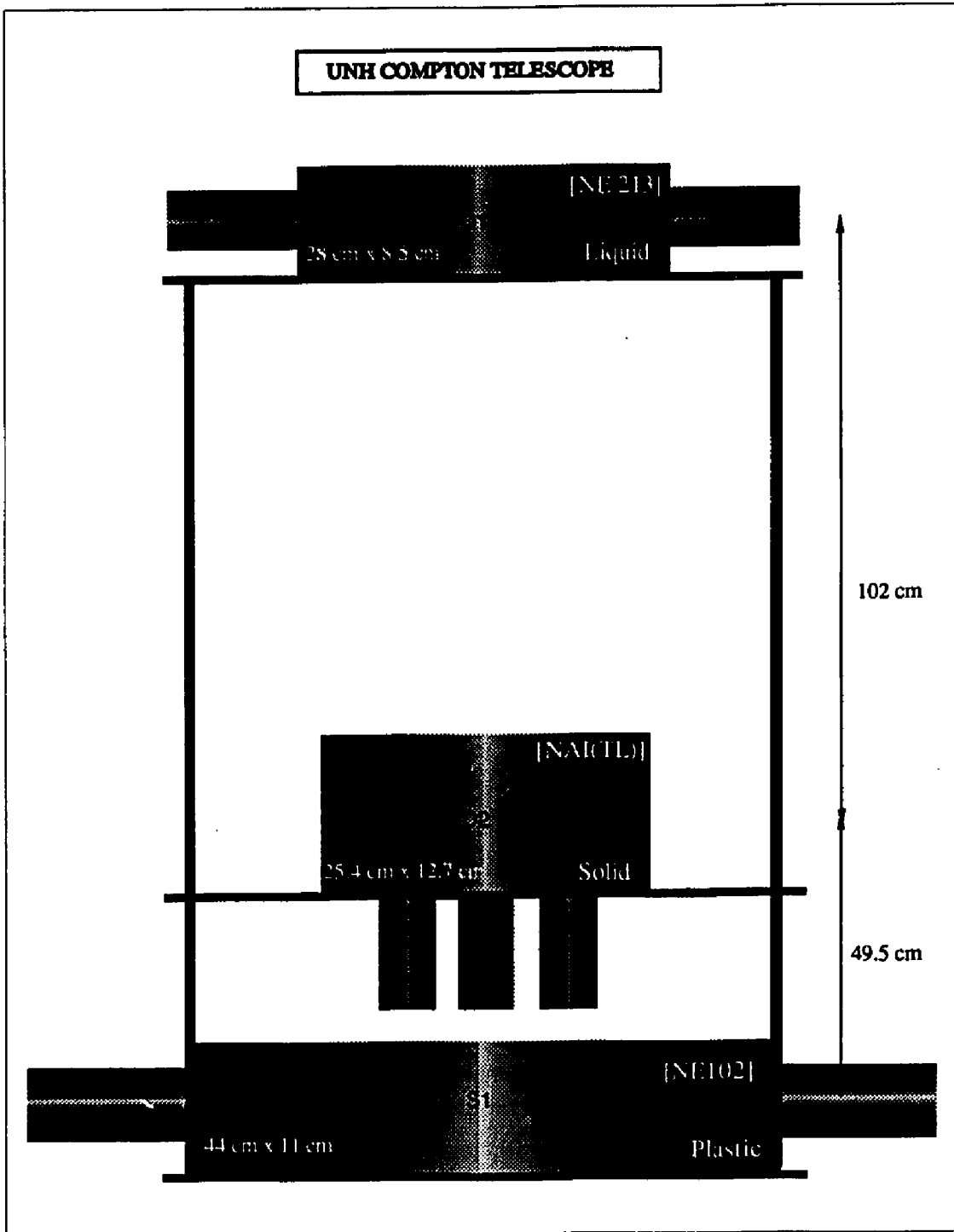


Fig. 2-1 : Telescope configuration

an energetic proton which deposits its energy via ionization. The signal produced by an ionizing electron differs from that due to a proton in its faster rise time. This characteristic forms the basis for pulse shape discrimination technique (PSD) used to separate gamma and neutron events in the upper detector.

The lower NaI(Tl) detector is a high density inorganic single crystal where photons undergo Compton scattering and photoelectric absorption. The high Z material has good photoelectric absorption efficiency to stop the scattered photon. The crystal is viewed by five PMTs (Hamamatsu R1307) mounted at the bottom. It has a linear pulse height response to gamma rays above ≈ 400 keV. The decay time is ≈ 230 ns significantly greater than that for organic scintillators.

The NE102 plastic scintillator also has a fast response time with a decay time of 2.4 ns and a hydrogen to carbon ratio of 1.104. The scintillator has eight PMTs (EMI 9821B) mounted radially and symmetrically along the side wall. For calibration purposes, LEDs are attached to upper NE213A and lower NaI(Tl) detectors. The LEDs are connected to a pulse generator and produce pulses at the rate of about 1 Hz within the detectors through small glass windows. During data collection runs when the LEDs are operating, the LED events are tagged. The LED peak provides a means to calibrate and monitor PMT gains, and along with a variable nanosecond delay facilitates calibration of the time of flight scale.

The UNH Compton telescope provides the following parameters for each accepted event:

- a). energy deposits in the upper and lower detectors.
- b). individual PMT signals necessary for event location.
- c). pulse shape discrimination signal separating photons from neutron events.

- d). time of flight value used to separate downward scattering from upward scattering events.
- e). LED flag indicating an LED calibration event.

Table 2-1
Properties of scintillators

Properties	Scintillators		
	NE213	NaI(Tl)	NE102
Type	Liquid	Solid	Plastic
Density	0.874	3.67	1.032
Refractive index	1.508	1.775	1.580
Light output *	78 %	230 %	65 %
Decay constant (ns)	3.7	230	2.4
Wave length of max. emission (nm)	425	413	423
H atoms / C atoms	1.213	----	1.104

* % Anthracene

Manual recording of the local temperature was carried out periodically during all observations and atmospheric pressure was constantly monitored by a precision barometer. The count rates of each detector were recorded frequently during observation times using a scalar. Energy calibration runs were conducted twice daily using radioactive sources.

Detection Mechanism

An incoming photon incident on the upper NE213A detector undergoes Compton scattering with the bound electrons of the scintillator material, imparting part of its energy to the electron. The scattered photon can travel to the lower detector where it may deposit the rest of its energy by photoelectric absorption or multiple Compton scattering. The sum of the energy deposits in the two detectors provides a measure of the energy of the incident photon. If the photon is only partially absorbed in NaI(Tl) this summed total energy will be less than the incident photon energy. A 6 MeV photon has an attenuation length of 7.8 cm in NaI(Tl) less than the D2 thickness. Hence, in the energy range of 1-6 MeV with the veto shield located just below the lower detector, the probability of partial absorption events being included is considered small. The angle between the scattered photon and the incident photon direction is completely determined by the energy deposits in the two detectors. It is given by

$$\cos(\theta) = 1 - m_0c^2 \left(\frac{1}{E_{\gamma'}} - \frac{1}{(E_{\gamma'} + E_e)} \right) \quad \dots(2-1)$$

where $m_0c^2 = 511$ keV, is the rest mass of the electron and $E_{\gamma'}$ and E_e are the energy deposits in D2 and D1 respectively. The scattered photon direction is defined by the interaction sites in D1 and D2. Thus, the incident photon can be determined to lie on the surface of a cone, centered about the scattered photon direction with a half-opening angle given by the scatter angle (Figure 2-2). The projection of the cone onto the sky produces a circle called the event circle. For any given event, the probability of source location is spread uniformly around the event circle. The source location can be located more precisely if there are many events from the same source. Individual event circles intersect within a region of maximum probability for finding the source. The detectors have minimum thresholds for detection below which they will not be triggered. This is very useful in keeping the large, low energy background event rate down, thus minimizing dead time loss

in the data acquisition system. On the other hand, it is clear from expression (2-1) that, minimum acceptable values of E_e and E_γ directly translates into a θ_{\min} and θ_{\max} respectively. For an incident photon of energy E_γ , the D1 minimum threshold determines the smallest scatter angle allowed while the D2 threshold determines the maximum scatter angle permissible. Thus,

$$\theta_{\min} = \cos^{-1} \left[1 - 511 \left(\frac{1}{[E_\gamma - (E_{th})_{D1}] - \frac{1}{E_\gamma}} \right) \right] \quad \dots\dots(2-2)$$

$$\theta_{\max} = \cos^{-1} \left[1 - 511 \left(\frac{1}{(E_{th})_{D2} - \frac{1}{E_\gamma}} \right) \right] \quad \dots\dots(2-3)$$

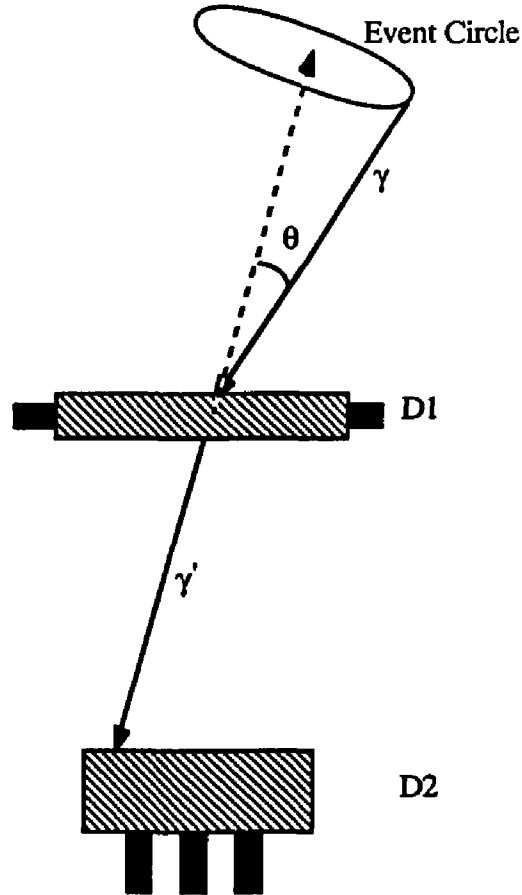


Fig. 2-2 : Principle of Compton telescope.

It is assumed here that the incident photon energy is completely deposited among the two detectors. Hardware thresholds of 150 keV and 500 keV were imposed on D1 and D2. For a 3 MeV photon, these threshold settings imply that $\theta_{\min} \approx 7.7^\circ$ and $\theta_{\max} \approx 82^\circ$. The scatter angle range used in the event acceptance criterion is 10-40 degrees. The restriction of the scatter angle to a value far below that given by (2-3) has been found to reduce false events improving the signal to noise ratio (Schönfelder *et al.*, 1982).

Principal Telescope Parameters

The principal parameters defining the operating characteristics of a Compton telescope are the following:

- 1). energy resolution
- 2). angular resolution
- 3). background rejection techniques
- 4). telescope efficiency

1). Energy Resolution

A monoenergetic source of gamma rays incident on a scintillation detector does not reproduce the input energy spectrum as a sharp δ -function peak in the output pulse height spectrum. In inorganic crystals as in NaI(Tl), the output resembles a broadened peak, the FWHM being determined by various parameters. In organic scintillators one usually observes only the Compton edge spectrum since the Compton scattering probability is high and the photon only deposits part of its energy within the detector. The important causes of line broadening are:

- a) total emission efficiency of the scintillator.
- b) inhomogenities in the scintillation media, light pipes, etc.
- c) variations in the amount of light seen by the PMT for different interaction locations.

- d) nonuniform response along the PMT cathode surface.
- e) presence of dark current in PMT.

The resulting pulse height is a measure of the number N of secondary electrons impinging on the PMT anode. The corresponding statistical error in N , is given by $\sigma = \sqrt{N}$. Since the dynode cascade is a multiplicative phenomenon, $\sigma \propto \sqrt{\text{Energy deposit}}$. This results in an approximately gaussian photopeak in the output energy spectrum. The intensity of line emission is proportional to the area under the peak. Estimation of energy resolution in the laboratory for the NaI(Tl) detector indicates a resolution proportional to the square root of the input photon energy.

In a Compton telescope the incident photon energy is shared between the upper and lower detectors subject to coincidence requirements. Hence, the total incident spectrum is not exhibited by either of the detectors. However, if we sum the two energy spectra for each incident event, the output resembles a broadened incident spectrum. The telescope energy resolution, affected by the individual detector resolutions, can be determined from this summed spectrum. The upper D1 cell has an energy resolution given by

$$\text{FWHM}(D1) = \frac{11.43}{\sqrt{E_{D1}}} + 1.2 \% \quad \dots(2-4)$$

where E_{D1} is energy deposited in D1 expressed in MeV. This is calculated from the D1 spectra obtained for different radioactive sources. At 1 MeV, the D1 resolution is $\approx 13\%$. The resolution of the lower D2 cell is also determined in a similar fashion and was found to be

$$\text{FWHM}(D2) \approx \frac{10}{\sqrt{E_{D2}}} \% \quad \dots(2-5)$$

where E_{D2} is energy deposited in D2 expressed in MeV. Tests carried out in the lab indicate a resolution of 9-10 % at 1 MeV. The telescope energy resolution is a function of the individual detector energy resolutions (Schönfelder *et al.*, 1982).

$$\Delta E_{\gamma} = \sqrt{ \left(\Delta E_{D1} \frac{E_{D1}}{E_{\gamma}} \right)^2 + \left(\Delta E_{D2} \frac{E_{D2}}{E_{\gamma}} \right)^2 } \quad \dots(2-6)$$

where ΔE_{D1} , ΔE_{D2} are the normalized FWHM of photopeaks in the detector pulse height spectra. Using (2-4) and (2-5), we can calculate the telescope efficiency from (2-6). The estimated telescope resolution for photons of energy 1.275 MeV scattering at 25° is ≈ 9.2 %, decreasing to ≈ 6.4 % at 3 MeV. Calibration measurements were carried out by illuminating the telescope using a Na^{22} gamma ray source placed at an angle of 25° from the telescope axis. The energy deposits E_{D1} and E_{D2} were determined. For totally absorbed events, the photon loses its energy within D1 and D2 and summing the two energy loss spectra, the incident gamma ray spectrum of Na^{22} was recreated (Figure 4-4). The energy resolution as determined from the reconstructed source spectra includes errors from energy calibration and was found to be ≈ 17 % for 1.275 MeV photons scattering at 25° zenith. The larger experimentally obtained value is partly due to the angular spread of $\pm 5^{\circ}$ about the scatter angle (25°) of accepted events which were included in the summed spectrum.

2). Angular Resolution

A telescope event can be determined to lie on the surface of a cone centered on the scattered photon direction. The scattered photon direction is given by the interaction locations in the two detectors. Thus, the angular resolution of a Compton telescope depends strongly on the spatial resolution attainable within each detector volume. The spatial resolution attainable within an Anger camera has no intrinsic limit, contrary to the case of an optically independent detector array where the individual detector size limits the spatial resolution. Thus improvements in interaction location algorithms and mapping

techniques can be used to constantly update spatial and angular resolutions of the telescope. The analysis presented here does not include position location of events in each detector. Under such conditions, the calculated scatter angle is considered equal to the zenith angle of the incident photon. The spatial resolution in D1 is determined to be 9.9 cm while that in the lower one to be 9.0 cm since events are known only to occur somewhere within each detector volume. The spatial resolutions in the two detectors translate into an angular uncertainty of 7.5° in the direction of the cone axis. Since scatter angle is a function of the energy deposits in the two detectors (equation 2-1), the angular resolution is also a function of energy resolution available in each detector (Schönfelder *et al.*, 1982). This is given by

$$\Delta\theta = \frac{180 E_0}{\pi \sin \theta} \sqrt{\left[\frac{1}{E_\gamma^2}\right]^2 \left[\frac{E_{res}^{D1}}{235.5} E_{D1}\right]^2 + \left[\frac{1}{E_{D2}^2} - \frac{1}{E_\gamma^2}\right]^2 \left[\frac{E_{res}^{D2}}{235.5} E_{D2}\right]^2} \quad \dots(2-7)$$

where $\Delta\theta$ (degrees) is the 1σ uncertainty of the scatter angle, $E_0 = 0.511$ MeV and E_{res}^{D1} , E_{res}^{D2} are the energy resolutions of D1 and D2, respectively. For a 3 MeV photon scattering at 20° , our telescope yielded $\Delta\theta$ to be 1.2° as a result of finite energy resolution. Adding in quadrature the energy and spatial contributions to the angular resolution, the total telescope angle resolution at 3 MeV and 20° scatter was found to be 7.5° , dominated by the spatial resolution effect.

The angular resolution of the telescope is significantly improved if event location is carried out in each detector. The detectors were mapped carefully using a Na^{22} source placed inside a carefully designed collimator developed for the GRO-COMPTEL project. The well collimated beam of gamma rays was positioned above a known detector location and the corresponding individual PMT signals were recorded on magnetic tape. This forms a signature for that specific interaction location. The measurements were repeated for various source locations forming a fine grid that covers the entire detector surface. The database containing all these signatures forms the mapping database for that detector. Assuming a one to one correspondence between PMT signature and source

location, any given signature can be translated into a specific interaction region using a location algorithm. Thus, the mapping database is necessary to determine the scattered photon direction. The analysis of the D1 mapping data for the science model of the GRO-COMPTTEL experiment along with the D2 map created at UNH indicates average spatial resolutions of ≈ 2 cm in D1 and ≈ 3 cm in D2 for 1.275 MeV photons incident on the detectors. The resulting spatial component of the angular resolution at 3 MeV and 20° scatter is 2.3° . Hence, the telescope has the potential to provide substantially improved angular resolution if event location is carried out. It would have also improved the background rejection capability of the telescope. However, the results being presented here do not include imaging with event location.

3). Background Reduction Methods

Gamma ray measurements in the MeV regions have always been troubled by the significantly large contribution of background events in the data under conditions of weak signals. Detection sensitivity of the telescope can be significantly improved by reducing the number of background events. In this respect, Compton telescopes for gamma ray measurements have been important. It is a unique feature that Compton telescope measurements also contain sufficient information to estimate most of the background contributions. We shall now discuss the various background reduction techniques applied to Compton telescope measurements.

a). Time of Flight (TOF) Discrimination

The time of flight signal provides the means to distinguish upward moving events from downward moving events. A photon incident on D1 with an energy deposit above D1 threshold generates a 'start' signal while the scattered photon interacting in D2 and satisfying D2 threshold requirement produces a 'stop' signal. These signals are used to convert the time difference into a voltage which can be used to distinguish upward and

downward moving events. The timing resolution available for the specific configuration determines how well the upward moving events can be separated from the downward moving ones. The resolution is jointly determined by the individual detectors involved. The individual timing resolutions are determined using a small test cell whose resolution is small and previously known. First D2 is replaced in the telescope configuration by the test cell and the timing resolution of the 'D1-test cell' configuration is determined. Similarly, D1 is replaced with the test cell and the timing resolution of the 'test-cell-D2' configuration is also determined. The timing resolution of the any pair of detectors acting as a telescope is given by the geometric mean of the individual resolutions. Since the resolution of the test cell is known, the timing resolutions of D1 and D2 can be separately determined. The fast scintillator in D1 produced a higher D1 timing resolution than in D2. The slower response of the NaI(Tl) crystal prevents a clear separation of the up and down TOF peaks (Figure 2-3). Increasing the distance between the detectors separates the peaks more clearly but

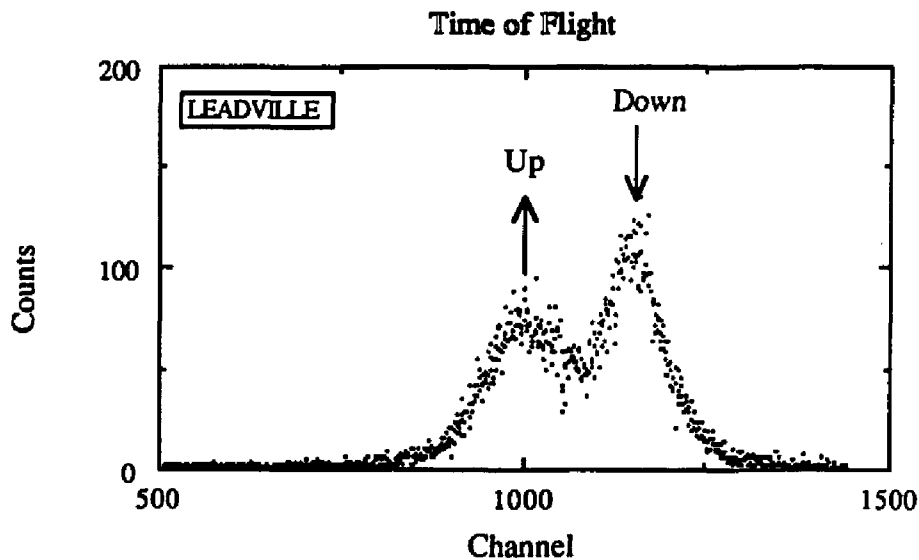


Fig. 2-3 : The TOF spectra is over a wide energy range of 1-12 MeV and has no PSD selection imposed upon it.

reduces the efficiency of the telescope. In our setup the upward peak is separated from the downward peak by 6.8 ns. The timing resolution of the D1-D2 telescope is ≈ 4.5 ns (FWHM). The overlap between the peaks is such that a clean downward scattering TOF window can be obtained if we consider only that half of the downward peak (Figure 4-6) which is farthest from the upward peak. The upward scattering event contribution to this window is determined to be below 5%. Since measurements were carried out over a long period of time, this 'half-window' does not statistically limit our data. The intrinsic symmetry of the TOF distribution allows us to double the counts under the cleaner half to obtain the number of downward events within our TOF window.

b). Pulse shape Discrimination (PSD)

Pulse shape discrimination is a technique used to distinguish pulses produced by different types of particles (Figure 2-4). NE213A produces scintillation pulses

PULSE SHAPE DISCRIMINATION

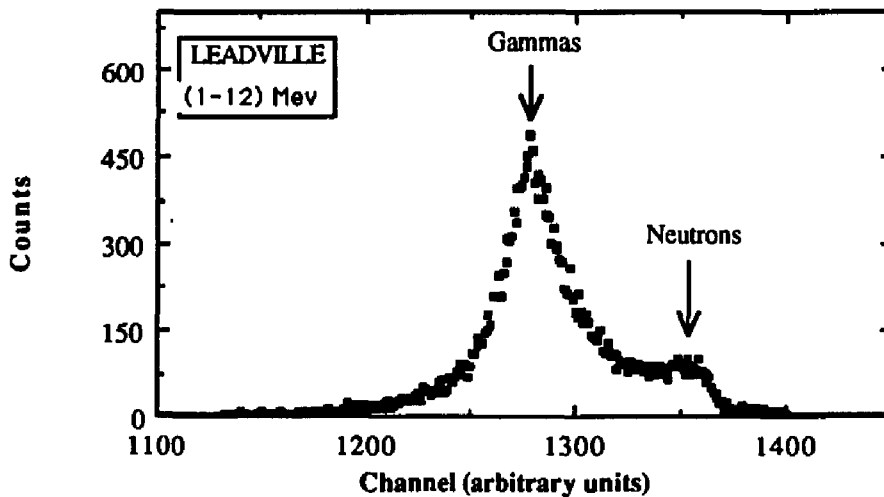


Fig. 2-4 : The PSD spectrum over a wide energy range of 1-12 MeV with no TOF selection. Gamma rays interactions lead to energy deposit by electrons while neutrons interactions result in energy deposit by protons in the scintillator.

composed of fast and slow components. Neutrons interacting in the liquid can give rise to energetic protons producing higher ionization density than electrons. This leads to significant *ionization quenching* for protons which reduces the intensity of the fast component (Birks, 1964). The integrated signal forming the basis for PSD combines the fast and slow components, producing a proton signal with a slower risetime than that of electrons. This difference in risetime is the basis for pulse shape discrimination utilized in rejecting neutron produced events and will be discussed later.

c). $\bar{\theta}$ Criterion

The limiting scatter angles (θ_{\min} , θ_{\max}) are determined by the detector threshold requirements (equations (2-2), (2-3)). A smaller scatter angle range can be imposed on the accepted events in order to define a field of view around the telescope axis. The constraining of events to a cone around the axis of the telescope significantly reduces the partial absorption event (D2 photon escape) contribution to the data. We have used a $\bar{\theta}$ criterion of $10^\circ \leq \theta \leq 40^\circ$ in our analysis.

4). Efficiency of Compton Telescopes.

Efficiency of a telescope is defined as the ratio of the number of events accepted to the number of events incident on the telescope. For a Compton telescope, the efficiency is strong function of photon energy and incident angle. An efficiency table enables us to convert measurements into absolute gamma ray intensities which can be compared with results obtained from other measurements. Thus, it is a very important telescope parameter and should be determined as accurately as possible.

The efficiency of the UNH Compton telescope was determined in two ways:

- a). Monte Carlo calculation
- b). Using sources of known radioactivity.

a). Monte Carlo Calculation

The Monte Carlo calculation was carried out using a simulation program 'MODEL' developed at UNH by G.Simpson (private communication). The model incorporates only photoelectric, Compton and pair production as photon interaction processes. Multiple scattering of photons in the upper NE213A liquid scintillator is allowed but the scattered electron in D1 is assumed to deposit all its energy at the scatter site. Restrictions on maximum scatter angle can be imposed on the simulated events. Full three dimensional geometry is incorporated for the detectors but photon interactions near the edges may give rise to some problems. The detectors D1 and D2 have aluminium cover plates (amounting to a total thickness of 0.25 inches) which lies in the path of the incident photon. The attenuation arising from this reduces the incident gamma ray intensity by 7.4%. Since the computer model does not include the aluminum shields, this is incorporated separately into the simulation results. The program was used to calculate the individual detector omnidirectional efficiencies as well as the telescope efficiency for energies in the range of 1-6 MeV and zenith angles of 10°-40°. These Monte Carlo simulation results are shown to be consistent with low energy efficiency measurements in the laboratory discussed below.

b). Determination with a Radioactive Source

A radioactive source with known activity can be used to measure the efficiency of a telescope. The sources used were Na²², Y⁸⁸ and Th²²⁸. The source strengths and associated photon energies are shown in table 2-2. A radioactive source placed at a distance from the telescope produced a nearly parallel beam of photons incident on the D1 detector. The sources were shielded passively to prevent direct exposure of D2 to the source as well as to reduce events resulting from room scattering. The source activity along with the geometry of the setup determine the number of incident photons on D1. The

Table 2-2

Radioactive sources used during efficiency measurements

Source	Energy	Activity (μCi)
Na ²²	1.275 MeV	20 \pm 20%
Y ⁸⁸	1.836 MeV	5.6 \pm 20%
Th ²²⁸	2.614 MeV	100 \pm 20%

same event selection criteria used in the data analysis (described in detail in chapter 4) are imposed on the telescope events to determine the number of accepted photons.

Using the relationship,
$$\text{Efficiency} = \frac{\text{number of accepted photons}}{\text{number of incident photons}}$$

the telescope efficiency is determined. The measurements were carried out carefully at various zenith angles and energies. Restrictions in TOF and PSD that are imposed on the laboratory data are often chosen to minimize background while maximizing the number of good events falling within the parameter windows. The selection criteria include acceptance windows in TOF and PSD which select most of the downward moving gamma rays but do not include events that fall in the tail of the two distributions. Using a 5th degree polynomial to fit the downward TOF distribution, it is found that 7% of the downward moving events fall outside the TOF selection window. A similar factor of 3% accounts for gamma ray interaction events that fall outside the 'gamma' PSD window resulting in a total of 10% decrease in the accepted events. Incorporating these into the calculation, absolute telescope efficiencies at low gamma ray energies were determined from the UNH laboratory measurements.

The telescope efficiencies obtained from Monte Carlo simulation and UNH laboratory measurements can be compared at low gamma ray energies to test the validity of

the Monte Carlo results. These are found to agree within 10%, with the Monte Carlo results being larger. This may partly be due to inherent problems in the particle propagation model used in the Monte Carlo program. The close agreement of efficiencies determined from

Table 2-3

Telescope efficiency (%) determined from Monte Carlo simulations. These agree within 10% to efficiency measurements carried out in the laboratory.

Zenith angle Energy (kev)	10 ⁰	15 ⁰	20 ⁰	25 ⁰	30 ⁰	35 ⁰	40 ⁰
1250			.211	.246	.264	.263	.240
1750		.275	.312	.281	.252	.226	.211
2250	.272	.316	.324	.278	.235	.210	.193
2750	.326	.328	.324	.275	.228	.203	.184
3250	.355	.344	.323	.272	.222	.193	.178
3750	.374	.349	.318	.268	.216	.190	.174
4250	.388	.354	.312	.260	.210	.187	.170
4750	.401	.354	.307	.260	.214	.187	.168
5250	.412	.355	.302	.251	.202	.176	.164
5750	.418	.330	.294	.238	.199	.173	.162

simulation studies and measurements at low energies permits the use of Monte Carlo results at higher energies where laboratory measurements are unavailable. The telescope efficiency provided by the Monte Carlo model for various gamma ray energies and incident

zenith angles are shown in table 2-3. For a 2 MeV gamma ray, the Monte Carlo telescope efficiency is plotted as a function of incident photon zenith angle in Figure 2-5. The efficiency is strongly dependent on the angle maximizing around 20°. The efficiency rapidly decreases beyond 35°. In Figure 2-6, the efficiency is plotted as a function of energy for events incident at a zenith angle of 20°. Near 1 MeV, the efficiency is sensitive to the detector threshold settings. Around 2-3 MeV, the efficiency reaches a maximum value, decreasing at higher energies. Beyond 10 MeV, Compton cross section is falling, decreasing the efficiency.

Advantages of a Compton Telescope

Compton telescopes provide a means to directly image the source of gamma rays using the principle of Compton scattering. In the few MeV range, the Compton interaction cross-section dominates other processes. The telescope is designed specifically to take advantage of this. The requirement of coincidence between signals in the two detectors reduces background events substantially. Consequently, the count rate is reduced to a minimum, reducing deadtime problems. The TOF system enables identification of upward and downward scattered photons. The accidental coincidence contribution can be easily estimated from the available data. PSD provides an additional technique criterion to reject many neutron-induced gamma ray events in the upper organic scintillator. The Anger camera principle minimizes loss of valuable detector area. The gain variations among PMTs is remains the most difficult problem. The zenith and azimuth angle of a source can be determined provided there are many events from the source. Thus the telescope provides real imaging capability. The wide field of view also provides the ability to simultaneously measure source and background. A source location of (ρ, δ) has a background location of $(\rho, \delta + 180)$ i.e., 180° shifted in azimuth angle. This automatically removes any gain variations in the background subtracted data and is effective under conditions of variable

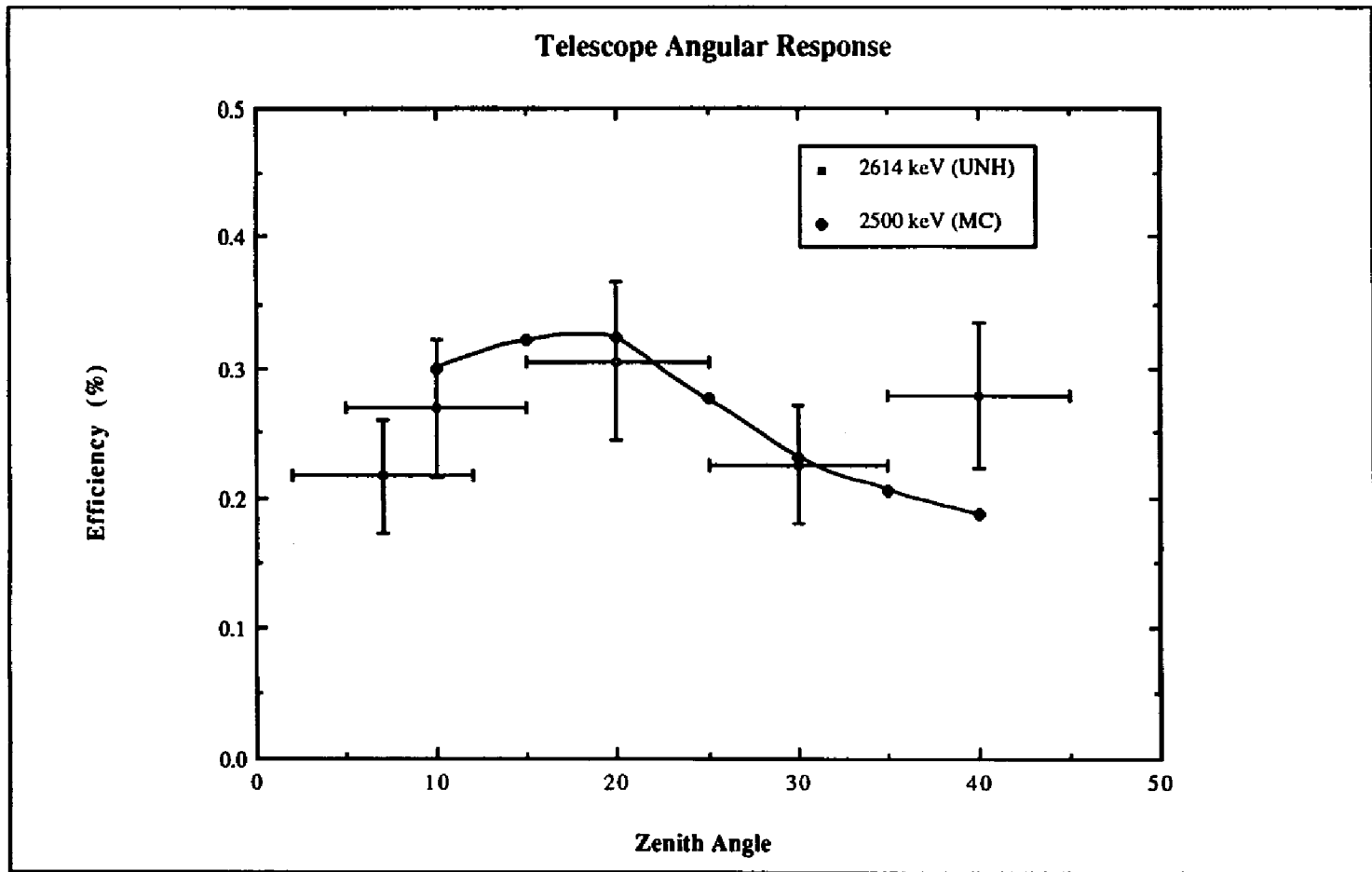


Fig. 2-5 : Telescope efficiency as a function of zenith angle for fixed photon energies. Monte Carlo (MC) results (interpolation line drawn through them) are compared with measured (UNH) efficiencies (20% error in activity).

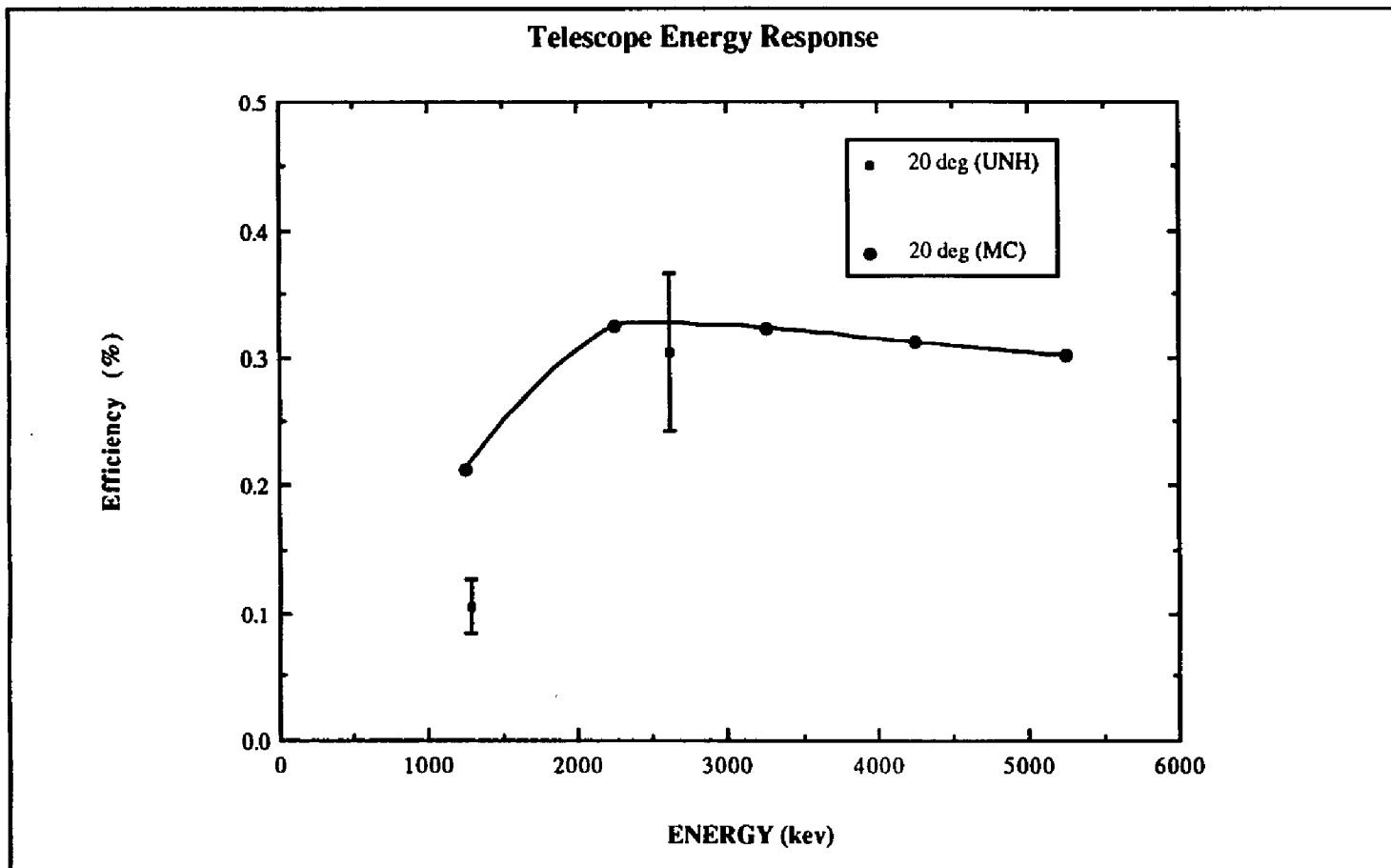
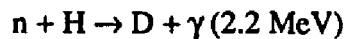
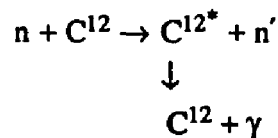


Fig. 2-6 : Telescope efficiency as a function of energy (Y-88 data point is missing due to error in runfile) for fixed zenith angle (20 deg). Monte Carlo results are compared with measured efficiencies (UNH).

background. Finally, the separation of gamma and neutrons makes it possible to obtain simultaneous measurements of both particle species.

Disadvantages of Compton Telescopes

The coincidence requirement puts a severe constraint on event acceptability resulting in low efficiency for the telescope. The telescope efficiency for this telescope is 0.1 % - 0.2 % at 2 MeV with a scatter angle of 20° . With this low efficiency it is difficult to obtain statistically significant results on weak sources of gamma rays. Furthermore, the efficiency is a strong function of energy and angle. The threshold on D1 implies a minimum scatter angle for acceptable events at any energy. This implies a blind spot at the detector axis, its size being a function of energy and D1 threshold. Scattered events that are not completely absorbed by D2 result in underestimation of the total photon energy and consequently overestimates the scatter angle. Neutron interactions in the organic scintillator result in events that simulate a gamma ray event in the telescope. Inelastic neutron scattering reactions with carbon result in particles that trigger D1 accompanied by a gamma ray which can trigger D2 within the TOF acceptance window. Inelastic neutron scattering interactions which result in proton emission can be rejected by PSD. The hydrogen present in organic scintillators take part in neutron capture reactions leading to the emission of gamma rays which interact in D1 and D2 and cannot be easily identified as a false event.



These have to be accounted for separately in the energy spectrum using their characteristic line features.

Position location of an event in a detector viewed by PMTs does not often yield a precise interaction point. Instead, one defines an interaction region, the extent of which is determined by scintillator characteristics, detector volume, number and positioning of the PMTs and energy deposited in the detector. The error in event location directly translates into an uncertainty in the scattered photon direction which reduces the resulting skymap resolution. The angular resolution is also significantly affected by the spatial resolution of the detectors.

Partial absorption of gamma rays by D2 can lead to errors in the energy and angular distribution. For a given energy, the probability for partial absorption decreases with increasing thickness of D2 and also for scintillation materials with larger atomic number since the photoelectric absorption is proportional to Z^5 . The relative probability for partial absorption increases with increasing energy of the scattered photon. For the case of an organic scintillator used as the lower detector, multiple scattering within the detector is required for the scattered photon to be completely absorbed. Thus the choice of a thick NaI(Tl) as the lower detector decreases the fraction of partially absorbed events. Partial absorption can be further reduced by the presence of a large veto detector below D2. Any photon escaping D2 can be detected by the veto detector. For our energy range of 1-6 MeV, the coincidence requirement between D1 and D2 along with simultaneous anti-coincidence with veto detector output, eliminates many partially absorbed events. A similar problem occurs when the scattered electron in the upper detector escapes. This results in underestimating both the energy and scatter angle.

A photon incident on D1 can occasionally undergo multiple scattering within the detector resulting in the scattered photon emerging along a direction different from that for a single scatter event. Our Monte Carlo simulation results give a multiple scattering probability of 6.6% in D1 for 1.275 MeV photons incident at 30° to the telescope axis and 4.4% at 5 MeV. The probability for one and only one scatter is a maximum for detector

thickness given by the reciprocal of the photon attenuation coefficient for Compton scattering (Hillier, 1984).

The coincidence requirement imposed on signals in D1 and D2 along with the time of flight acceptance window help in keeping the background rate down. However, there is a finite probability for two separate uncorrelated photons to trigger the detectors, producing a TOF signal within the downward acceptance window. These are called accidental events or chance coincidence events and they simulate a real Compton scattered gamma ray events. The accidental event rate can be estimated approximately as a function of individual detector count rates as well as to the width of the timing window and is given by

$$R_{acc.} = 2\tau R_1 R_2 \quad \dots(2-8)$$

where R_1 and R_2 are the individual detector count rates and τ is the coincidence interval (≈ 120 ns). The individual detector count rates are usually very large in comparison to the coincidence rate. The rates strongly depend on threshold and volume of detector. In our setup, the NE213A cell had a trigger count rate of 900 cts/sec while NaI(Tl) had a trigger count rate of 1250 cts/sec at Boulder. The accidental rate given by (2-8) at Boulder was 0.3 cts/sec. These accidental events are uniformly spread over all TOF channels and so the accidental events contained within the downward TOF window is small compared with the telescope count rate of ≈ 1 ct/sec. Since individual count rates decrease with increasing energy, the accidental count rate rapidly decreases with energy. Raising the detector thresholds decreases the accidental rate but it also restricts the range of energy and angle available to the telescope. The procedure used to account for accidental events in our analysis is discussed in chapter 4.

Other difficulties do arise in the context of producing skymaps depending on the method being used. Since this work did not involve source imaging, we shall not discuss it here. For a detailed discussion of the various imaging techniques used in Compton telescopes one can refer to the work published by O'Neill (1987).

Electronics Hardware

The upper and veto detectors are viewed by eight PMTs while the lower NaI(Tl) crystal has five PMTs mounted beneath the crystal (Figure 2-1). A PMT amplifies the input light signal producing a few microamp current signal at the anode. The accelerating potential between successive dynodes is determined by the bleeder string circuit at the base of the PMT. The anode as well as the last dynode signal are extracted from each PMT. The dynode pulse has a shorter risetime and is opposite in polarity to the anode signal. It forms the basis for the fast coincidence circuit which includes threshold circuitry and the fast trigger logic for TOF, PSD and veto function. If the signal satisfies threshold conditions, the fast Front End Electronics (FEE) box generates a trigger for the coincidence circuit. Also, the trigger produces a start/stop signal for the Time to Amplitude Converter (TAC). The FEE produces the PSD signal based on the risetime of the input signal.

The anode signals from all PMTs of a detector feed the individual Slow Front End box (SFE) which contains charge sensitive preamplifiers and a summing amplifier. The outputs for all input signals along with the sum signal are fed into a pulse shaping unit. The output pulse from the individual PMT preamplifiers are shaped in preparation for digitization. The pulse shaping circuit minimizes the pulse period and thus reduces dead time loss. It is also used to enhance the electronic signal to noise ratio leading to improved energy resolution (Tsoufanidis, 1972).

Front End Electronics (FEE)

The dynode outputs from individual PMTs form the core of the logic circuit used to select or veto events (Figure 2-9). Individual dynode signals of each detector fed into the FEE box are summed to provide a detector fast signal. These summed fast signals from the three detectors form the input for the fast logic circuit which determines the TOF and the coincidence/veto logic for each event. The most important requirement for the fast logic circuit, is the ability to precisely produce sharp timing signals indicating the arrival of a

pulse. The timing signals generated suffer from jitter and walk (Paulus, 1985). Jitter arises from statistical fluctuations of detector signals while walk arises due to the relative time variation between the input and output due to changes in amplitude or shape of the input pulse. Walk is significant for signals that barely exceed threshold. Aging components along with temperature fluctuations can lead to drift in the timing signal. It is important to minimize the dependence of the timing signal on pulse amplitude (ie., energy dependence) and noise riding on the fast signal. There are various techniques to produce a good timing signal viz., leading-edge, zero-crossing, constant-fraction, etc. These are discussed in detail in several books (Tsoufanidis (1972), Paulus (1985)). In our telescope electronics, we have incorporated the constant-fraction technique to produce fast timing signals making the timing signal roughly independent of pulse amplitude. In addition, pulses with the same risetime always give the same zero-crossing time, a property useful for the pulse shape discrimination circuit. The fast sum signal is fed to a discriminator determining the threshold requirement for incoming signals. For a well defined narrow input pulse, the threshold is defined as the input pulse height at which there are half the number of output triggers as input signals. The threshold is set externally using a reference current unit. The discriminator generates a fast logic signal for coincidence and timing circuits when thresholds are satisfied.

Coincidence Circuit

The coincidence condition in a Compton telescope is used to gate the energy loss measurement in each of the two detectors. Physically, the coincidence output signal gates the ADC system. The coincidence unit defines a coincident event as one where a second signal arrives within a set time interval τ after the arrival of initial signal. This time interval is generally referred to as the resolving time. We have used a resolving time of ≈ 120 ns. The system suppresses the coincidence output if a veto signal from the plastic scintillator arrives within the same time interval τ .

The fast logic outputs of D1 and D2 FEEs are fed into dual gate generator (LeCroy 222), the output of which is a logic NIM pulse (logic state : 0 = 0.0V, 1 = -0.8V) whose width can be set to any time interval from 3 nanoseconds to a few microseconds. They are timed appropriately and fed into a 4-fold logic unit (LeCroy 365AL) which executes the coincidence / veto algebra among the three different input signals. The output of the veto detector is fed into the 'veto' input of the coincidence unit. Upon satisfying the coincidence condition along with no veto signal within the set coincidence interval, the unit generates an event acceptance signal for further event processing.

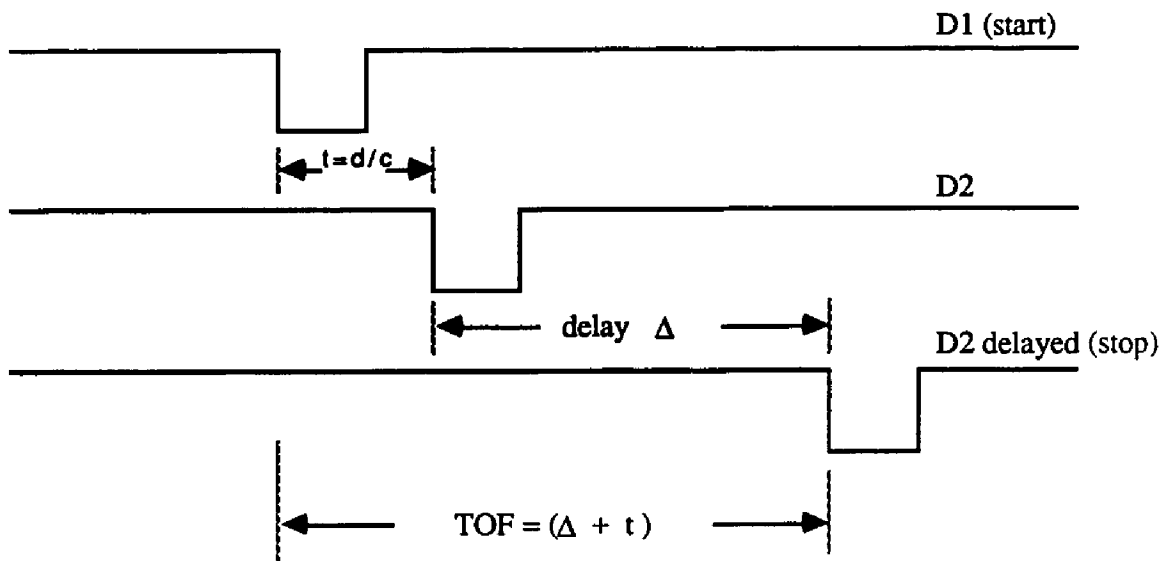
Time of Flight Circuit

The logic signals that are fed into the coincidence unit, are also shared by the Time to Amplitude Converter (TAC) unit which provides the Time of Flight (TOF) signal for the an event. Fast logic signals generated by the individual FEEs boxes are appropriately delayed and fed into the start and stop channels of a Time to Amplitude Converter (TAC). The D1 FEE output generates the 'start' pulse while the corresponding D2 FEE output generates the 'stop'. The D2 FEE output is delayed by a fixed delay to separate upward and downward moving events (Figure 2-7). Consequently, an upward moving event produces a smaller amplitude signal compared to a downward moving event. A variable nanosecond delay is connected to the 'stop' signal to facilitate timing calibration.

Pulse Shape Discrimination Circuit

The PSD property of NE213A is used to distinguish between electron-recoil and proton-recoil events. As stated earlier, the PMT output signal has different pulse shapes for electron-recoil and proton-recoil events. The leading-edge of the fast PMT signal is timed and used as the start of the zero-crossing. The fast signal is integrated to amplify the difference in pulse shape between gamma and neutron events in the form of a faster decay rate for gamma ray signals. Using a constant-fraction circuit on the integrated pulse,

Downward moving event



Upward moving event

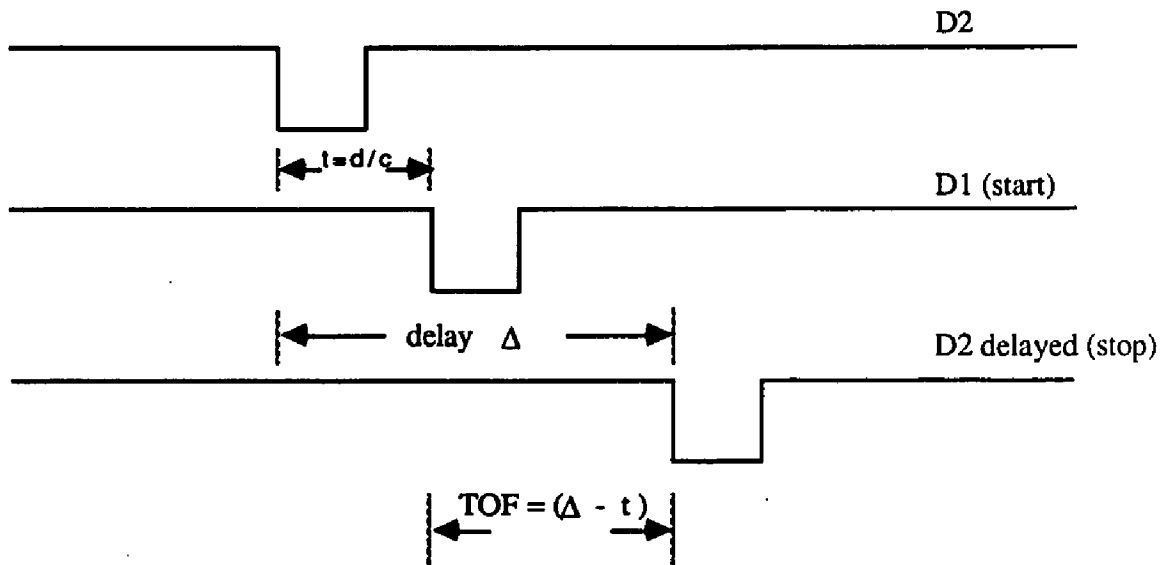


Fig. 2-7 : Principle of Time of Flight (TOF) measurement.

the zero-crossing time is determined. This crossover time is different for gamma and neutron events providing the PSD output to distinguish such events.

Track and Hold Circuit

The analog signals that correspond to all individual PMT outputs, the sum signals from D1 and D2, TOF and PSD signals all need to be digitized and stored into a

TRACK & HOLD TIMING DIAGRAM

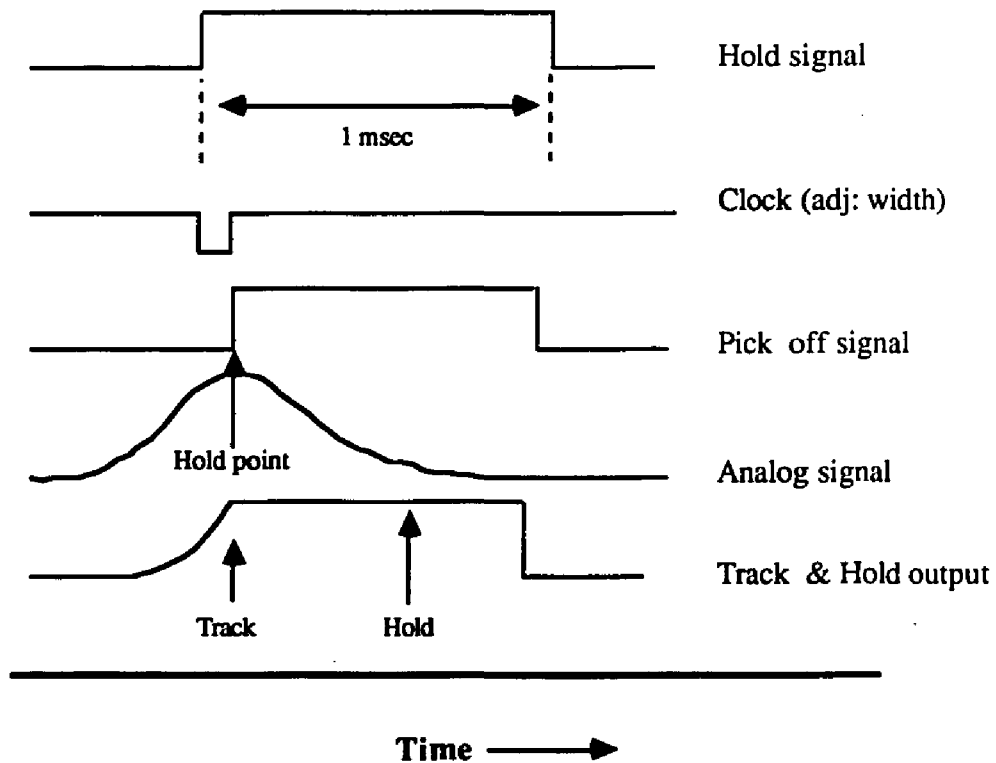


Fig . 2-8 : Timing signals involved with the Track & Hold circuit.

computer, using a data acquisition system. The 17 analog inputs need to be precisely timed in order to coincide with the coincidence output pulse. Since the digitizing of each analog signal requires a finite interval of time, it is necessary to retain the instantaneous value of each input signal over the time interval required to convert them to digital values. A Track and Hold circuit fulfills this requirement. During the *track* mode the circuit allows rapid charging of the storage capacitor while during the *hold* mode, the capacitor is disconnected from its charging source and retains its charge. Since we are interested in the peak value of pulses, the *hold* phase is switched on at the instant of time corresponding to the peak value of the analog signal, retaining the maximum of all 17 inputs. The *hold* signal is set long enough to allow the Analog to Digital Converter (ADC) to digitize all inputs through a multiplexer (Figure 2-8).

Data Acquisition System

The standard (STD) bus data acquisition system links the telescope outputs with a microcomputer (IBM PC/XT) controlling and storing the incoming data. The STD bus has a 56 pin configuration and operates on $\pm 5V$ and $\pm 12V$ DC power. The processor used is a 4 MHz Z80A chip on the CPU board (ProLog 7806). Additional cards attached to the bus include a serial input/output (SIO) card, a parallel input/output (PIO) card and additional memory cards. The BIOS and the raw data display software was developed by the Spectra Research Inc. of Dover, NH. A high speed serial interface board built at UNH connected to the IBM bus provides fast communication between the PC and the STD bus through two RS-232 serial ports with baud rates of 19.2 K or more. The acquisition software (courtesy Spectra Research Inc.) provided direct control of data collection and real time data display with the option of imposing selection conditions on events. The real time display can provide histograms and multiple scatter plots of various event parameters such as individual PMT pulse heights, PSD, TOF, LED flag, etc. The data are stored on a 20 megabyte hard disk and backed up on floppy diskettes and 60 megabyte tape cartridges.

Typically, a 24 hour run at Mt. Washington (823 g-cm²) generates ≈ 3-4 megabytes of raw data. Details of the data collection stations are discussed in the next chapter.

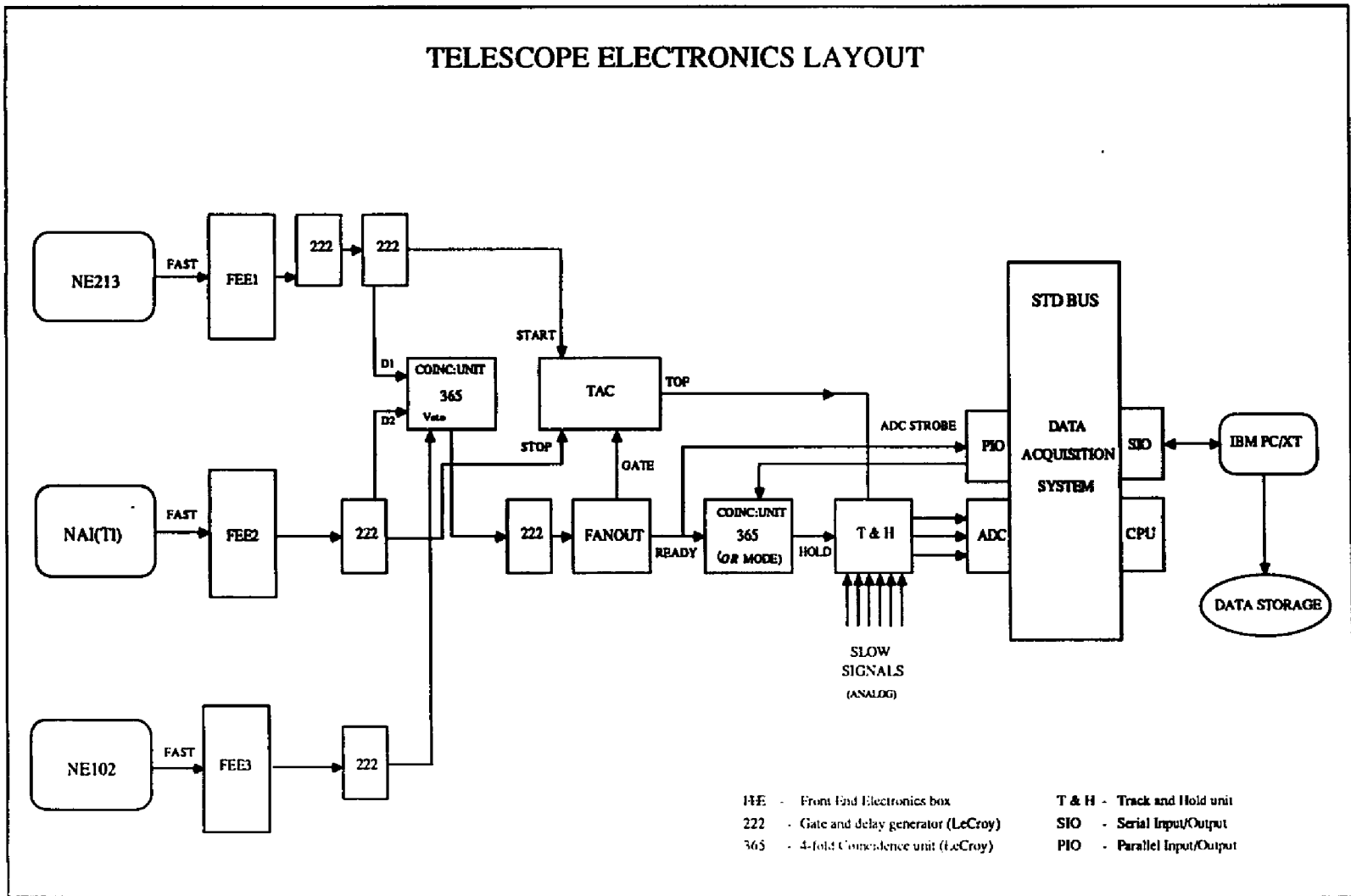


Fig. 2-9 : Fast logic layout and data acquisition system.

CHAPTER 3

ASPECTS OF DATA COLLECTION

The primary goal of our experiments is to study the low energy atmospheric gamma ray flux at ground level with the help of a simple Compton gamma ray telescope which provides good background suppression and modest angular information. The intrinsic low efficiency of Compton telescopes is disadvantageous in situations where the collection time is limited and the source is weak. We have partially overcome this problem by collecting data over long periods of time, roughly two weeks at each station providing us with a statistically significant dataset. The telescope and its support electronic systems were designed such that the system can be easily dismantled and reassembled. The data acquisition system was constructed to be rugged and was linked to a portable computer system. The modular construction made the complete system transportable, particularly important in transporting it to the summit of Mt. Washington. The measurements sites were Leadville and Boulder in Colorado and Mt. Washington and Durham. These sites provide a reasonable range of altitudes (sea level - 10,000 ft) and a small variation in latitude and geomagnetic cutoff rigidity (1.4 GV - 2.9 GV). Details of these locations are summarized in Table 3-1.

Leadville, Colorado

The first data collection station was in the small town of Leadville, Colorado, elevation 10,200 ft. The telescope was housed inside a small building with a wooden roof and brick walls which extended only 3 ft above the upper detector D1. The telescope after attaining temperature stability, was tested carefully for equal and consistent gains in all PMTs. LEDs mounted on D1 and D2 were triggered using an external pulse generator at

Table 3-1

Data on observation sites

Station	Altitude (ft)	Atmos: depth (gm/cm ²)	Geographic		Geomagnetic		Cutoff Rigidity (GV)
			lat.	long.	lat.	long.	
Leadville	10200	720	39.10N	106.20W	48.05N	43.93W	2.97
Mt. Washington	6072	823	44.16N	71.18W	55.77N	2.33W	1.43
Boulder	5430	851	40.01N	105.17W	48.89N	43.00W	2.90
Durham	80	1033	43.08N	70.56W	54.57N	1.71W	1.61

the rate of 1 Hz to constantly monitor PMT gains. These LED events were flagged as calibration events in the data stream to distinguish them from gamma ray events. During the first trip data were collected from February 10, 1987 to February 23, 1987. Temperature was maintained to within $\pm 4^\circ$ F and was regularly monitored manually. Simultaneously, the barometric pressure was continuously monitored by a precision digital barometer attached to a neutron telescope experiment which was operating nearby. Energy calibrations were conducted frequently during the day using radioactive sources as well as using the omnipresent K^{40} and Th^{228} naturally occurring sources of gamma radiation. The PSD calibration was conducted occasionally using an Am^{241} - Be^9 gamma-neutron source. Quick analysis of data from this trip indicated a need to conduct more careful energy calibration measurements. On a second trip from June 1 to June 6 1987, we obtained more gamma ray data in conjunction with more careful calibration runs. Excluding calibration runs, a total of 121 hrs of data were collected. The results presented here use 39 hrs of error-free data runs obtained during the second trip to Leadville. The average barometric pressure during the first trip was 691 millibars with an average temperature was 74° F. Corresponding values for the second trip were 706 millibars and 74° F, respectively.

Boulder, Colorado

The experiment was moved to Boulder, Colorado, altitude 5430 ft, in June 1987. The experiment was setup once again inside a single storied building with a corrugated roof in an attempt to minimize material above the telescope. Preliminary checkouts indicated that the NaI(Tl) detector gains had changed slightly since the Leadville runs. High voltages were fine tuned to maintain gain stability between Leadville and Boulder. Data were collected from July 13 to July 23 1987. The temperature stability was improved from that at Leadville with the help an industrial cooling system. Calibration runs were carried out daily. Data runs totaled to 168 hrs of which 115 hrs were used in this analysis. The

temperature was maintained at 72° F and the average barometric pressure averaged 835 millibars.

Mt. Washington, New Hampshire

The experiment was shipped back to New Hampshire and was placed inside a rented truck. The truck was insulated and temperature was well maintained using a thermostatically controlled heater, air conditioner and a dehumidifier. The truck was parked below the main summit building in an isolated spot to shield the electronics from possible radio noise interference generated in the TV and radio facilities at the summit. The telescope was maintained within the truck with only the power cables protruding out. Data were collected from Aug 8 to Aug 19 1987. Calibration runs were conducted daily. Barometric pressure data were obtained from the dynamic pressure system at the Mt. Washington Observatory since the changing wind patterns could have biased our standard barometer output in the truck. An average temperature of 71° F was maintained at the instrument. The pressure averaged 807 millibars. In all 229 hrs of data were collected. Results from 176 hrs of data are presented here.

Durham, New Hampshire

The same configuration inside the truck was maintained for the Durham data runs. Once again care was taken to see that there were no large masses in the vicinity such as a brick building in order to minimize the effect of splash gamma rays. The data were collected from August 20 to August 23 1987 and later from October 23 to November 2 1987. The raw data rate at Durham was about 50% of that measured atop Mt. Washington. The average barometric pressure was 1013 millibars and temperature was maintained at 71°

F A total of 186 hrs of data were collected of which 88 hrs of clean runs were analysed in obtaining the results presented here.

The collected event rate decreased with increasing atmospheric depth. At Leadville, the raw accepted event rate was ≈ 3.2 cts/sec while at Durham it was ≈ 1.2 cts/sec. This decrease in event rate is expected from the attenuation processes in the intervening atmosphere.

CHAPTER 4

ANALYSIS PROCEDURE

The atmospheric gamma ray data gathered at various locations were processed using a series of transformations and selection criteria to obtain quantities of scientific interest. The data collected at each station were recorded on 5¹/₄ and 3¹/₂ inch floppy diskettes on the IBM XT personal computer. The raw data were stored in binary format with each file characterized by a header containing housekeeping data and any relevant comments followed by a continuous stream of event data. Each event is characterized by 18 output readings from the analog to digital converter (ADC) board. These are

- 1). eight D1 PMT outputs
- 2). D1 sum signal
- 3). five D2 PMT outputs
- 4). D2 sum signal
- 5). TAC output
- 6). PSD signal
- 7). Veto/LED flag

The raw data need to be reduced from count rate into the more interesting quantities such as differential (photons/sec-cm²-sr-MeV) and integral photon flux (photons/sec-cm²-sr). As a first step, energy calibration is carried out to convert the raw pulse heights into energy deposits. The scattering angle corresponding to an event is unambiguously determined by equation (2-1). Timing calibration is necessary to separate upward and downward moving events while PSD calibration provides a means to separate gamma rays from neutrons. Any

energy dependence of PSD or TOF calibration (commonly referred to as 'walk') needs to be corrected, before imposing any event selection criterion on the data.

Energy Calibration

Radioactive sources emitting gamma ray lines in the MeV region are used in the calibration procedure. The sources along with photon energies and activities are listed in table 4-1.

Table 4-1

Radioactive sources used in energy calibration.

Source	Energy(MeV)	Activity(μ Ci)
Cs ¹³⁷	0.667	6.9
Na ²²	1.275	.09
Co ⁶⁰	1.117 1.332	1.2
Y ⁸⁸	0.896 1.836	10
Tl ²⁰⁸	2.614	100
Am ²⁴¹ -Be ⁹	4.43	10000

Gamma ray lines from K⁴⁰ (1.461 MeV) and Th²²⁸ (2.614 MeV) which are emitted by terrestrial material around the telescope were also used as calibration sources. It needs to be

pointed out that the maximum photon energy available for calibration was 4.43 MeV while the high energy limit of the telescope is ≈ 12 MeV. This is adequate for the work being presented here, since the maximum energy considered is 6 MeV. On an average, the calibration runs were conducted twice daily. These runs also serve as systematic checks to monitor variations in detector gain.

Energy Calibration of NE213A Detector

The energy loss spectrum in an organic scintillator is dominated by the Compton scattering process in the low energy gamma ray regime. The significant features of such a spectrum consists of a Compton edge, the Compton continuum and the backscatter peak. There is no prominent photopeak in the energy loss spectrum corresponding to the incident photon energy. In an ideal spectrum, the sharp Compton edge of the distribution can be used for energy calibration. Unfortunately, the edge is generally smeared out due to the finite detector resolution, making calibration a more difficult task. However, the peak of the Compton edge and the half-count point (where the peak count falls to half its value) are two clearly identifiable features that can be of use in a calibration. Dietze and Klein (1982) have conducted detailed studies on the Compton energy loss spectrum in NE213A scintillators using detectors of various sizes. They determined the position of the actual Compton edge in the presence of finite energy resolution using a multiparameter fit to the spectra. The ratios

$$\alpha = \frac{\text{peak channel}}{\text{Compton edge channel}} ; \quad \beta = \frac{\text{half count channel}}{\text{Compton edge channel}}$$

provide the peak and half-count point locations relative to the Compton edge. They conclude that the position of the Compton edge is nearer to the half-count point for small detectors than for large ones. The parameters α and β are a function of detector resolution. Interpolation of the data of Dietze and Klein (1982) along with proper scaling provide us

with a means to convert the peak and half-count point from channel number into energy. It can be pointed out that a direct calibration of organic scintillators at low energies can be carried out using the backscatter peak in the energy loss spectrum assuming that the detector threshold is not set too high. Our D1 energy calibration data indicates a best fit power law relationship between the photon energy and pulse height for energies below ≈ 200 keV and a straight line fit at higher energies (Figure 4-1). The D1 calibrations differ slightly among the various sites, most likely due to local variations in temperature and small gain changes in the system.

Energy Calibration of NaI(Tl) Detector

Inorganic crystals produce a clear photopeak in their energy loss spectra due to the large photoelectric cross-section at MeV energies, thus allowing a direct and accurate energy calibration. Calibration data for NaI(Tl) was obtained by illuminating the detector with standard radioactive sources (table 4-1). As in the case of the NE213A detector, a power law in energy is observed to fit the calibration data at low energies while a straight line fits the high energy regime (Figure 4-2). As in the case of D1 there were small changes among the calibrations obtained at various locations consistent with variations in gain and operating temperature. The NaI(Tl) detector gain was observed to be more sensitive to temperature variations than that observed in the NE213A detector.

A good telescope event is one in which the photon scatters in D1 and the scattered photon completely deposits its energy in D2. Thus, summing the energy deposits in D1 and D2 should yield the total energy of the incident photon. A good test of the calibration procedure is indicated by the reproduction of the incident spectrum through this summing process. Our calibration runs are in good agreement with the standard input spectrum of many of the radioactive sources. In Figure 4-3, the summed spectrum displays the K^{40} (1.461 MeV) and Th^{228} (2.614 MeV) lines that occur naturally on Earth.

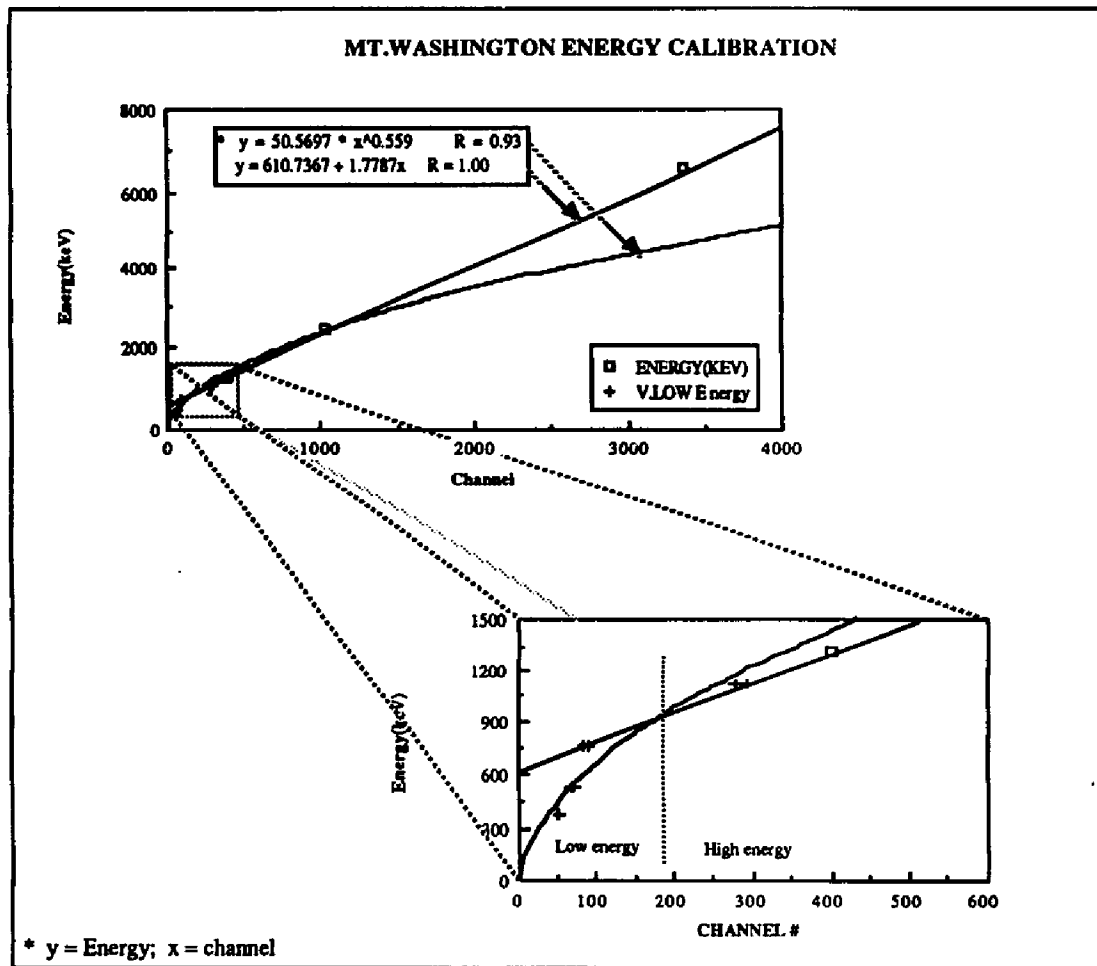


Fig. 4-1 : Energy calibration in NE213

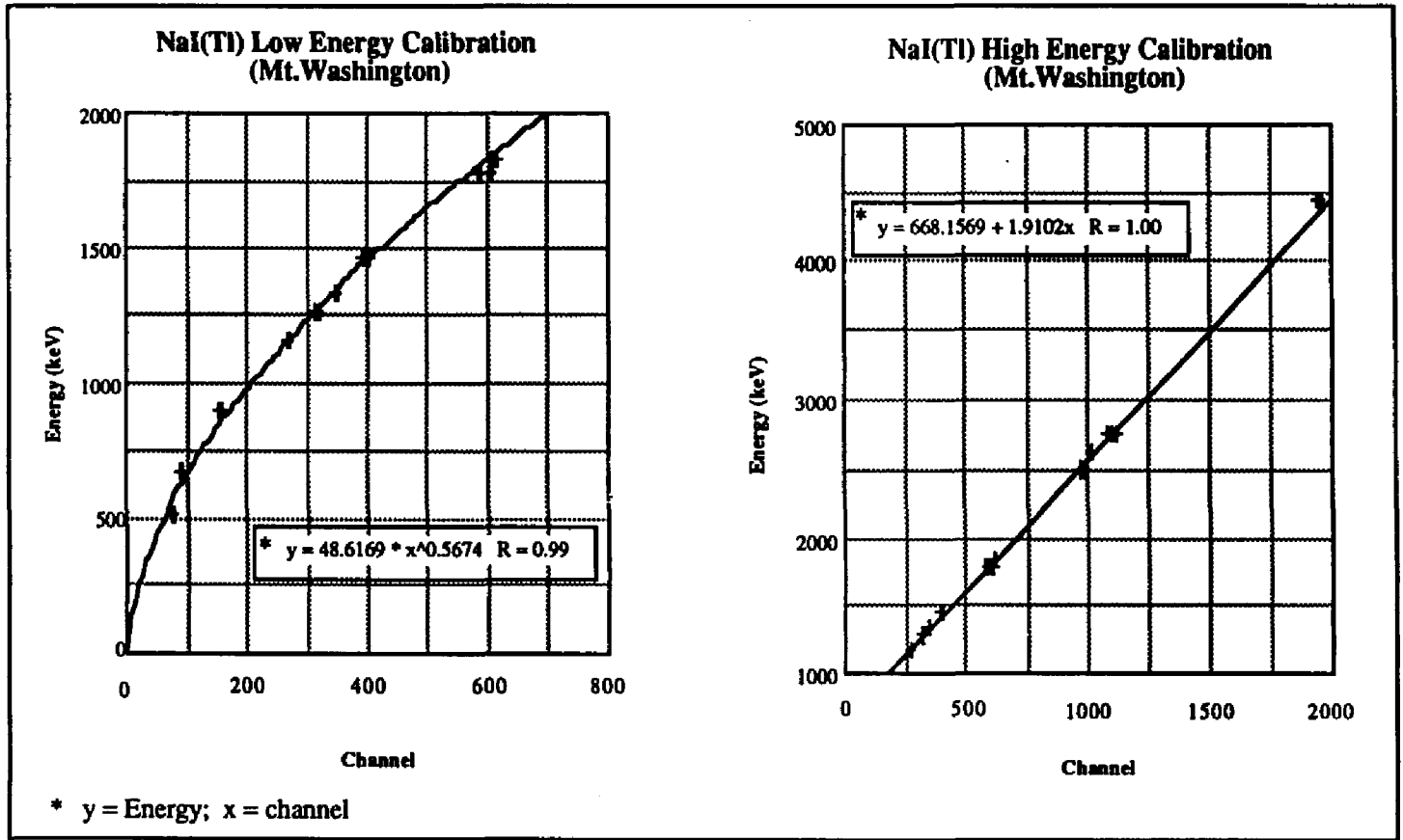


Fig 4-2 : Energy calibration in NaI(Tl)

Figure 4-4 shows the energy loss spectrum in D1 and D2 along with the summed spectrum for a Na²² source placed at 20° zenith angle.

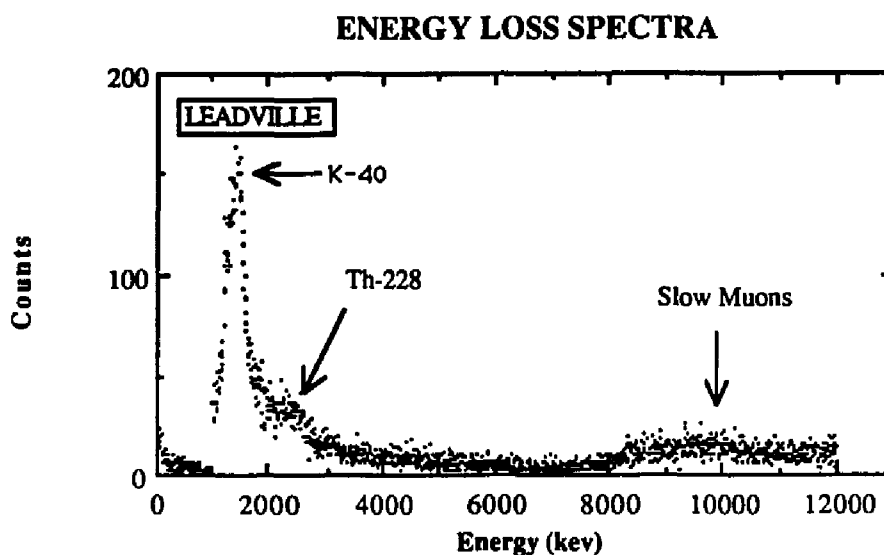


Fig. 4-3 : The energy loss spectrum ($E1+E2$) without any TOF or PSD selection for events in the 10°-40° range.

TOF Calibration

The TOF calibration is carried out using input pulses from an external pulse generator into the 'start' and 'stop' of the Time to Amplitude Converter. The calibration of the time scale is accomplished by using a variable nanosecond delay in the 'stop' signal line of the TOF circuit (Figure 4-5). The TOF peak position is noted for various delay settings. The calibration curve indicates a slope of ≈ 50 channel/ns. A source (Co^{60}) positioned above the telescope provided the downward TOF signal and placing it below D2 provided the upward signal (Figure 4-6). A Na²² radioactive source emits two 0.511 MeV photons moving 180° to each other. By placing such a source at the midpoint between the two

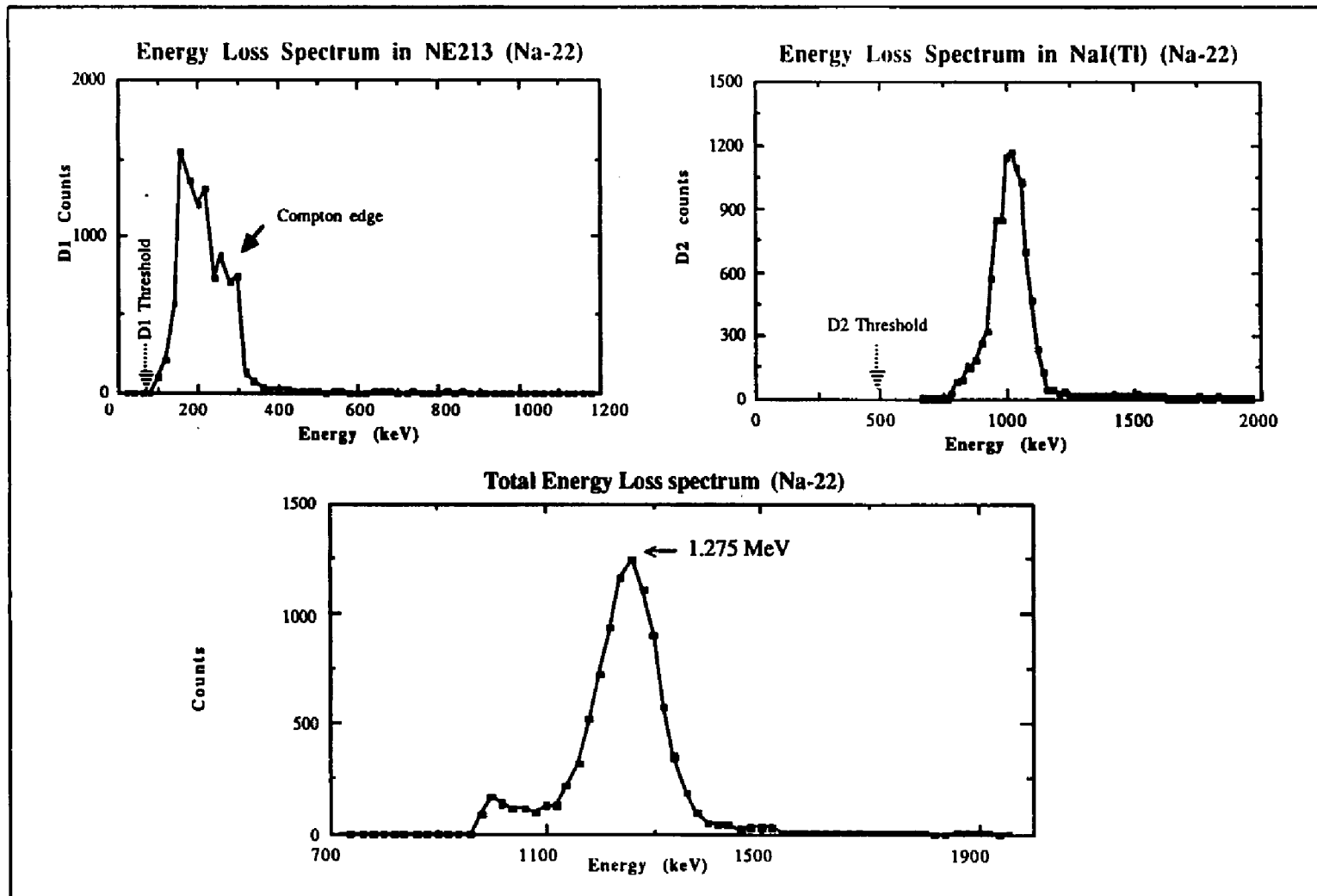
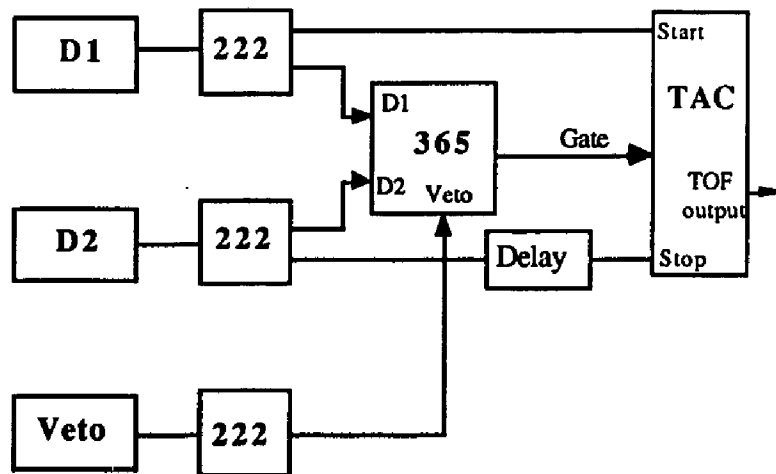


Fig. 4-4 : Energy Loss Spectrum in NE213 and NaI(Tl) along with the summed total energy spectrum (Na-22 source - 1.275 MeV ; 20 degree scatter)

detectors, the zero point in timing can be determined. The TOF spectrum shows no indications of *walk* in the system.

Accidental TOF Event Correction

A background contribution from accidental coincidences between independent events in D1 and D2 was discussed in chapter 2. Since the accidental coincidence occurs between random events, the corresponding TOF value is also a random value within the allowed



222- Gate and delay amplifier (LeCroy)

365 - Coincidence unit (LeCroy)

TAC - Time to Amplitude Converter

Fig. 4-5 : Time of flight calibration setup.

TOF signal range ie., it produces a uniformly distributed TOF spectrum. This allows simultaneous determination of the accidental spectrum by examining events in a TOF window far away from the upward and downward peaks of the spectrum. We are

interested in determining the number of accidental events contained within the downward TOF acceptance window in each runfile. This is directly obtained if we replace the proper TOF selection window in the event selection criterion by a window of identical width but shifted to a region of the spectrum far away from the up and down distributions (Figure 4-6).

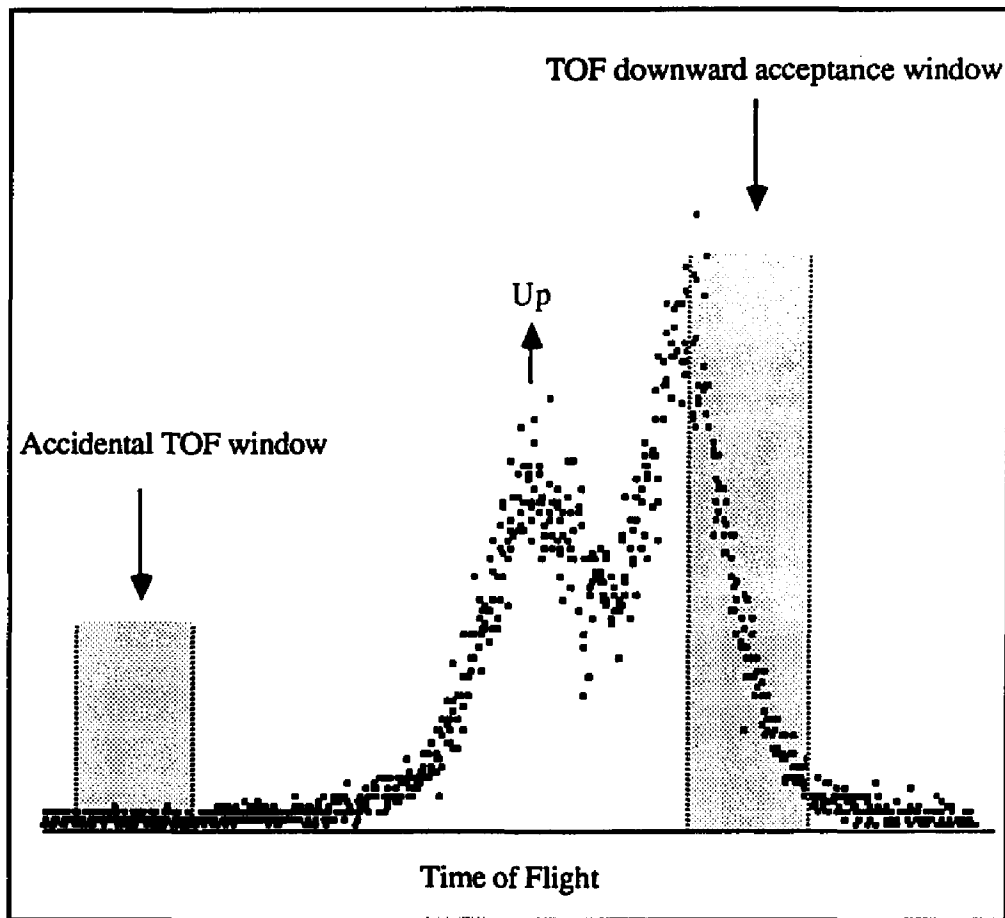


Fig. 4-6 : Time of Flight windows (equal widths) for downward (good events) and accidental events.

The accidental coincidence contribution to the event data is found to be under 5% at all data collection sites except in the lower energy region of 1-2 MeV where it was under 10%. The

accidental contribution determined for each data run file was subtracted from the event counts under the downward window to obtain the background corrected counts.

PSD Calibration

PSD calibration must be conducted using a source of gamma rays and neutrons, e.g. $\text{Am}^{241}\text{-Be}^9$. The neutrons emitted along with the 4.43 MeV gamma rays were used to check the PSD circuit and to determine the gamma and neutron acceptance windows or more correctly the electron and proton scintillations windows. The scatter plot of D1 energy deposit against PSD output indicates a strong correlation implying a walk in the circuit. A knowledge of the dependence of PSD on D1 energy deposit was used to remove walk. The fit separates in two regimes, one with a stronger energy dependence at low energies. The quadratic fit covering most of the D1 energy regime is shown in Figure 4-7.

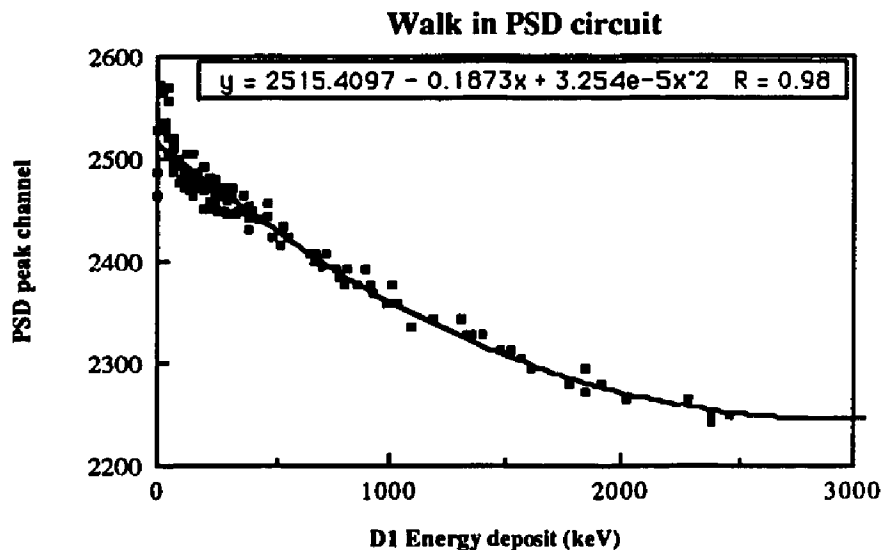


Fig 4-7 PSD walk correction plot. A quadratic fit is indicated for the all energies except for the smallest D1 energy deposits.

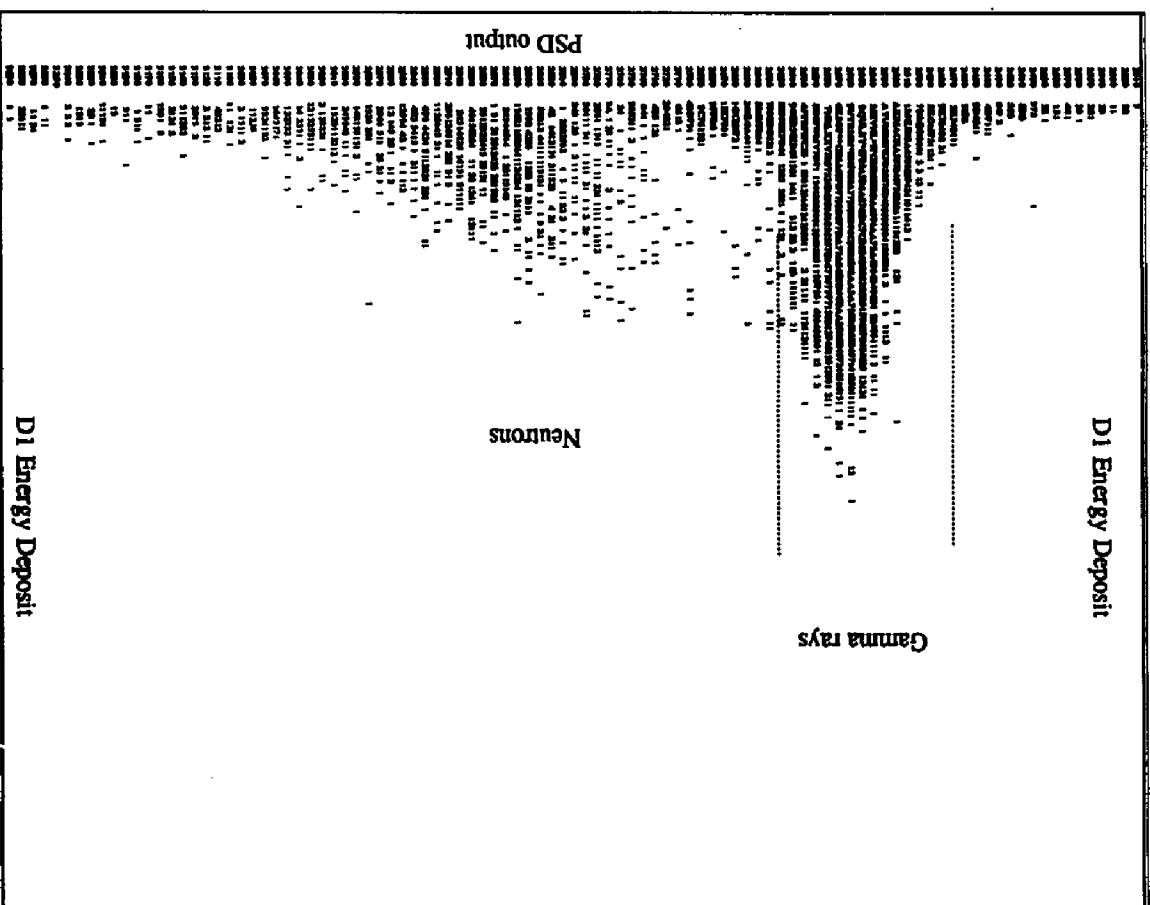


Fig. 4-8 : PSD - D1 (energy deposit) scatter plot indicating PSD selection window.

Figure 4-8 shows a walk corrected 'PSD-D1 energy deposit' scatter plot. It clearly indicates that a separation between gamma ray and neutron events can be achieved.

Event Selection Criterion

An event is acceptable if it satisfies all the requirements set forth in energy, scatter angle, TOF and PSD parameter space. These constraints are defined below:

Energy range	1.0 - 12.0 MeV
Scatter angle	10 ⁰ - 40 ⁰
TOF window	4.6 ns wide downward TOF window (ref. Figure 4-6)
PSD window	Gamma window (ref. Figure 4-8)

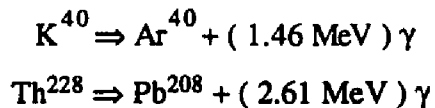
The energy range has been further reduced to (1-6) MeV to prevent contamination of data by slow muon events which stop in the lower detector completely. It is not possible to identify these muon events from the high energy gamma rays due to the absence of any clear differences in their signatures. Also at lower energies the data has significant contributions from the background lines of K⁴⁰ and Th²²⁸. The cleanest energy range is hence from 3 to 6 MeV. All least square fits have been carried out only on this relatively clean dataset.

After carrying out energy calibration, PSD walk correction and scatter angle calculations on each runfile, it was converted from its original binary format into ASCII and loaded into a database manager RBASE on the IBM PC. The database environment provided flexibility in carrying out calculations on the data and in imposing any selection criterion on events. Those that satisfy the selection criterion were accumulated into subsets for further analysis. The photon energy range of 1-6 MeV was subdivided into 10 bins of

500 keV, maintaining good statistical significance. In scatter angles, three 10° bins covered the range of 10° to 40° . For each runfile, the counts in each energy-angle bin were counted. The downward TOF acceptance window was then replaced by the accidental window and the process was repeated to determine accidental event contribution to each energy-angle bin. The corrected bin counts were averaged over all runfiles to obtain final counting rates as a function of photon energy and scatter angle.

Observational Difficulties

There were strong indications of undesirable events satisfying the event selection criterion in the 1-3 MeV range leading to errors in the estimated atmospheric gamma ray flux measurements. Ground level measurements are plagued by gamma rays arising from terrestrial radioactivity. These gamma rays are mainly from radioactive K^{40} and Th^{228} in nearby rocks and, in the case of thorium, from igneous rocks and uranium rich geological areas. Thus, the contribution of radioactivity to the measured atmospheric spectrum can vary with the geology of the site (Figure 4-9).



The summed spectrum (E1 + E2) shows the presence of K^{40} (1.461 MeV) and Th^{228} (2.614 MeV) peaks even after event selection criteria are applied to the data. This implies that these events are mostly propagating in the downward direction fulfilling all selection criteria. The higher background rate from accidental coincidence is accounted for throughout the analysis since the accidental event contribution discussed in the previous section, is determined for each run file separately. Even though most of the K^{40} and Th^{228} emission is from the ground below, there is a small contribution from building materials sufficiently high above the telescope to emit photons into the telescope field of view. In Figure 4-10, the energy loss spectrum is plotted before and after TOF selection is imposed

on the data. In Figure 4-11, K^{40} and Th^{228} line features in the energy loss spectra corresponding to the upward and downward TOF windows show different spectral shapes. This supports the argument that most of the line contributions seen in the downward TOF window do not arise from the tail of the upward TOF distribution. The line contributions in the downward TOF window are corrected using factors determined as described below. The energy loss spectrum of events that satisfy all event selection criteria is assumed to be made up of a continuum component produced by atmospheric gamma rays which falls off with increasing energy and line components from K^{40} and Th^{228} radioactivity. A quadratic polynomial function is used to fit the continuum on either sides of the K^{40} and Th^{228} line emissions. The continuum is subtracted from the energy loss spectrum to obtain the line contributions. The lines are fitted using gaussian distributions (Figure 4-12). Contributions from the lines and the continuum within the 1-2 MeV and 2-3 MeV energy bins are determined separately from the corresponding fits. The scaling ratios,

$$f(E)_i = \left[\frac{\text{continuum contribution}}{(\text{line} + \text{continuum}) \text{ contribution}} \right]_i$$

where index 'i' represents (1-2) or (2-3) MeV energy bins, are determined for each case. Using the relation $(\text{Corrected flux})_i = f(E)_i \times (\text{measured flux})_i$, the background corrected values are obtained in the 1-3 MeV range. The ratios $f(E)_i$ are determined for each location and are shown in table 4-2. Thus the method described above has been successful in dealing with the background line contribution in the data.

All measurements were carried out within thin roofed buildings, maintaining good temperature stability, minimizing gain variations and thermal stress to the sensitive NaI(Tl) crystal. The thin roof minimizes attenuation of atmospheric gamma ray photons. Nevertheless, it must be pointed out that the distribution of material around the telescope varied with each site. At Mt. Washington and Durham, this effect was minimized by placing the telescope in the same truck. The K^{40} contamination was found to be greatest at Boulder where the amount of material above the upper detector was large (Figure 4-9). Thus it is

very important to reduce material around the telescope to a minimum in order to obtain absolute measurements in the 1-3 MeV energy range and using the same housing unit for the telescope at all locations will allow better comparison of results from various sites.

Table 4-2.

Correction factors used to account for background contributions from K^{40} (1.46 MeV) and Th^{228} (2.61 MeV) lines in the (1-2) and (2-3) MeV energy bins respectively. Corrected flux = correction factor * measured flux.

Location	Atmos. depth (g/cm ²)	Correction factor	
		(1-2) MeV	(2-3) MeV
Leadville	720	0.78	0.92
Mt. Washington	823	0.79	0.92
Boulder	851	0.68	0.80
Durham	1033	0.77	0.97

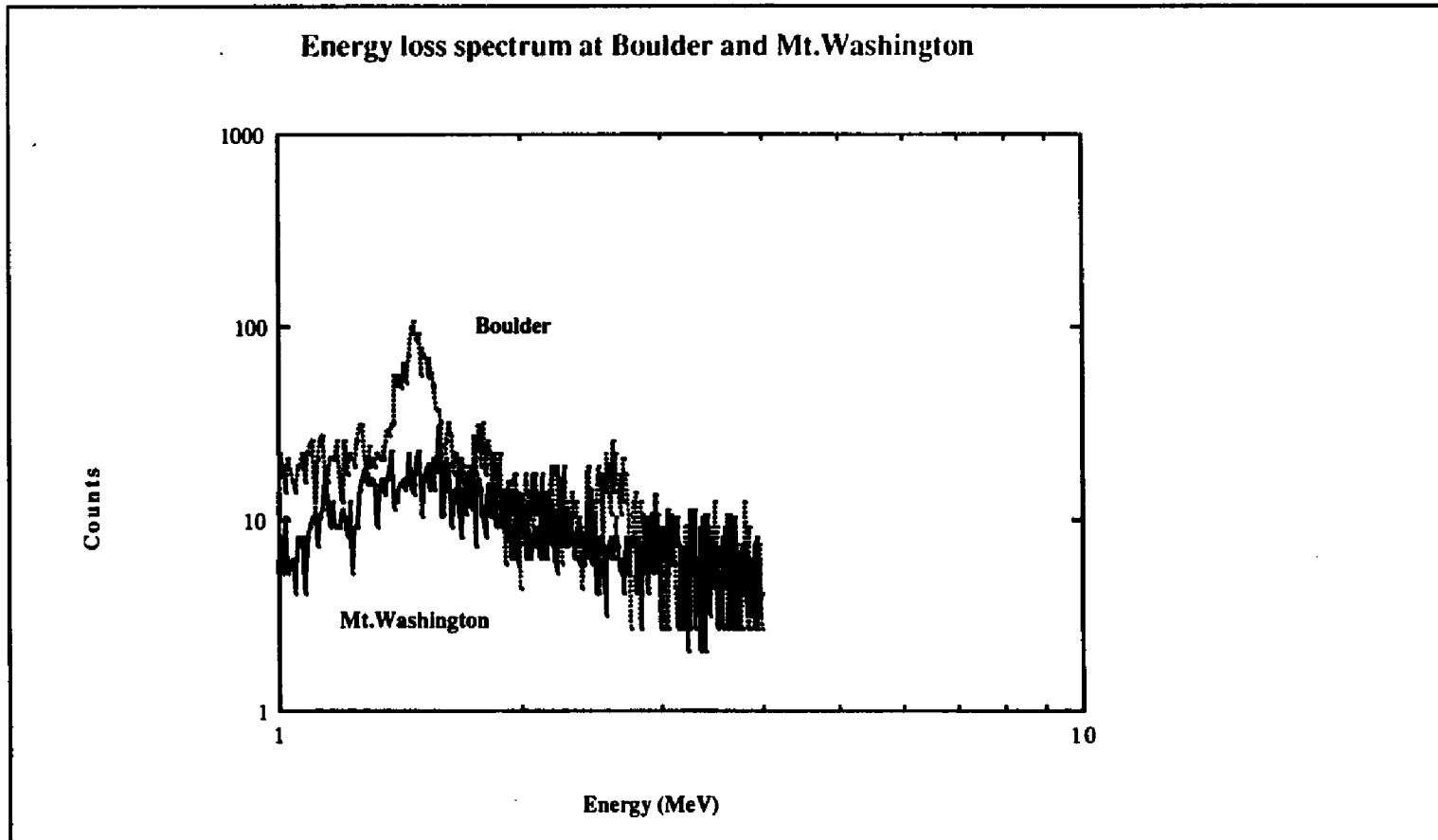


Fig. 4-9 : Comparison of energy loss spectrum in the downward TOF window at Boulder (dotted line) and Mt.Washington (solid line). Enhanced presence of K-40 at Boulder can be clearly observed.

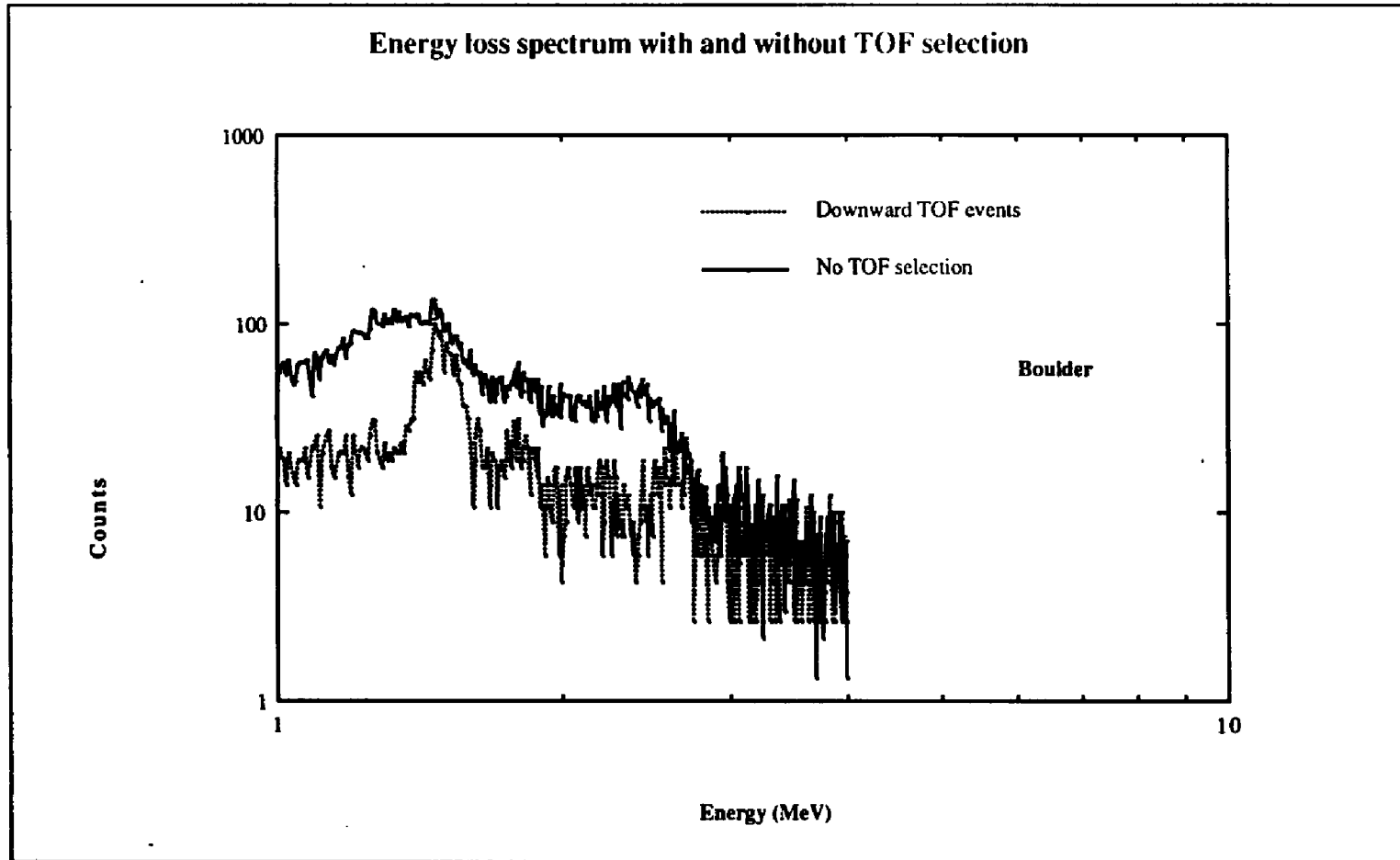


Fig. 4-10 : The energy loss spectrum is plotted with and without selection in TOF.

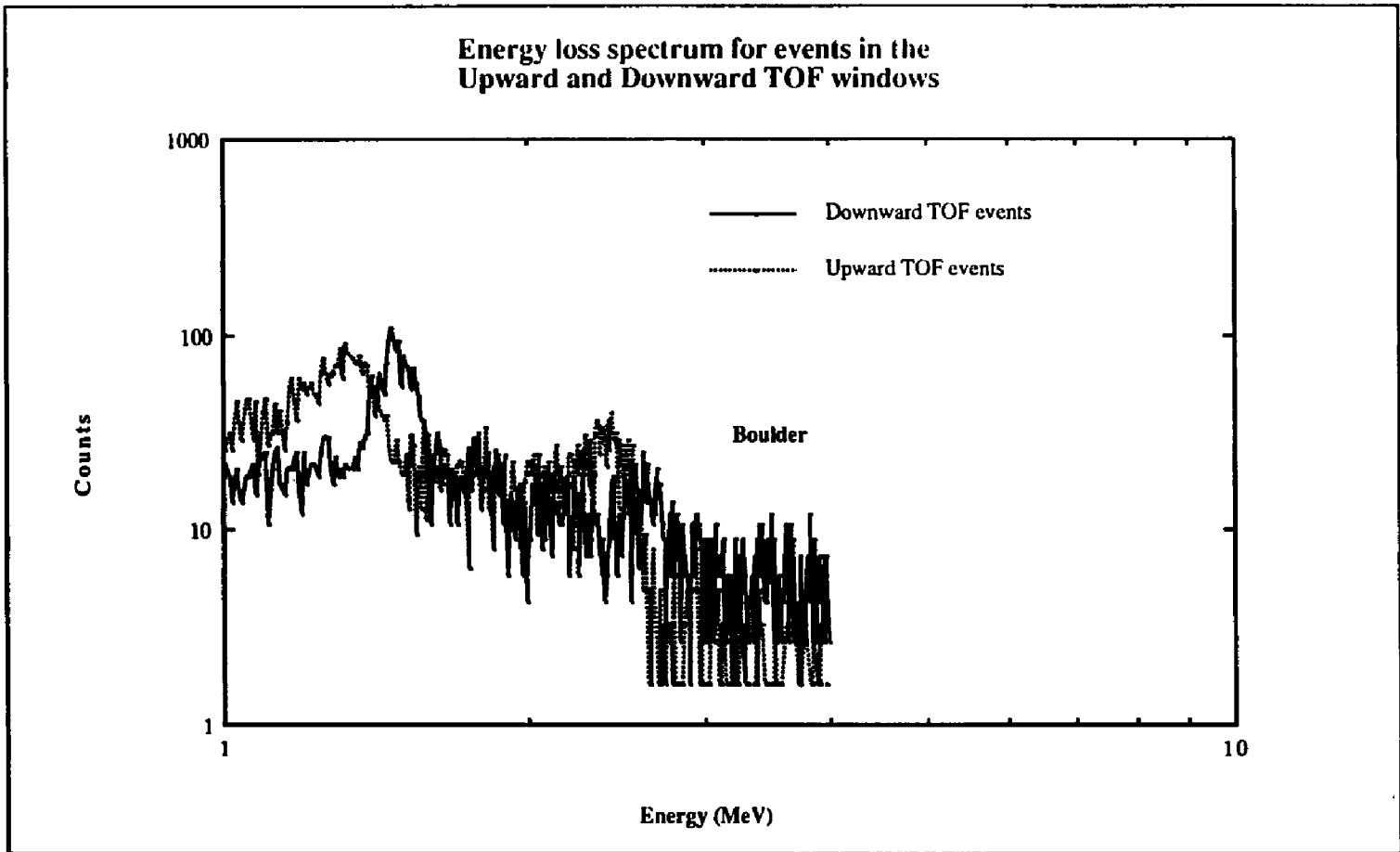


Fig. 4-11: The energy loss spectrum corresponding to events in the upward and downward TOF windows (24 hr run). There are significant differences between the spectral shapes of the two distributions.

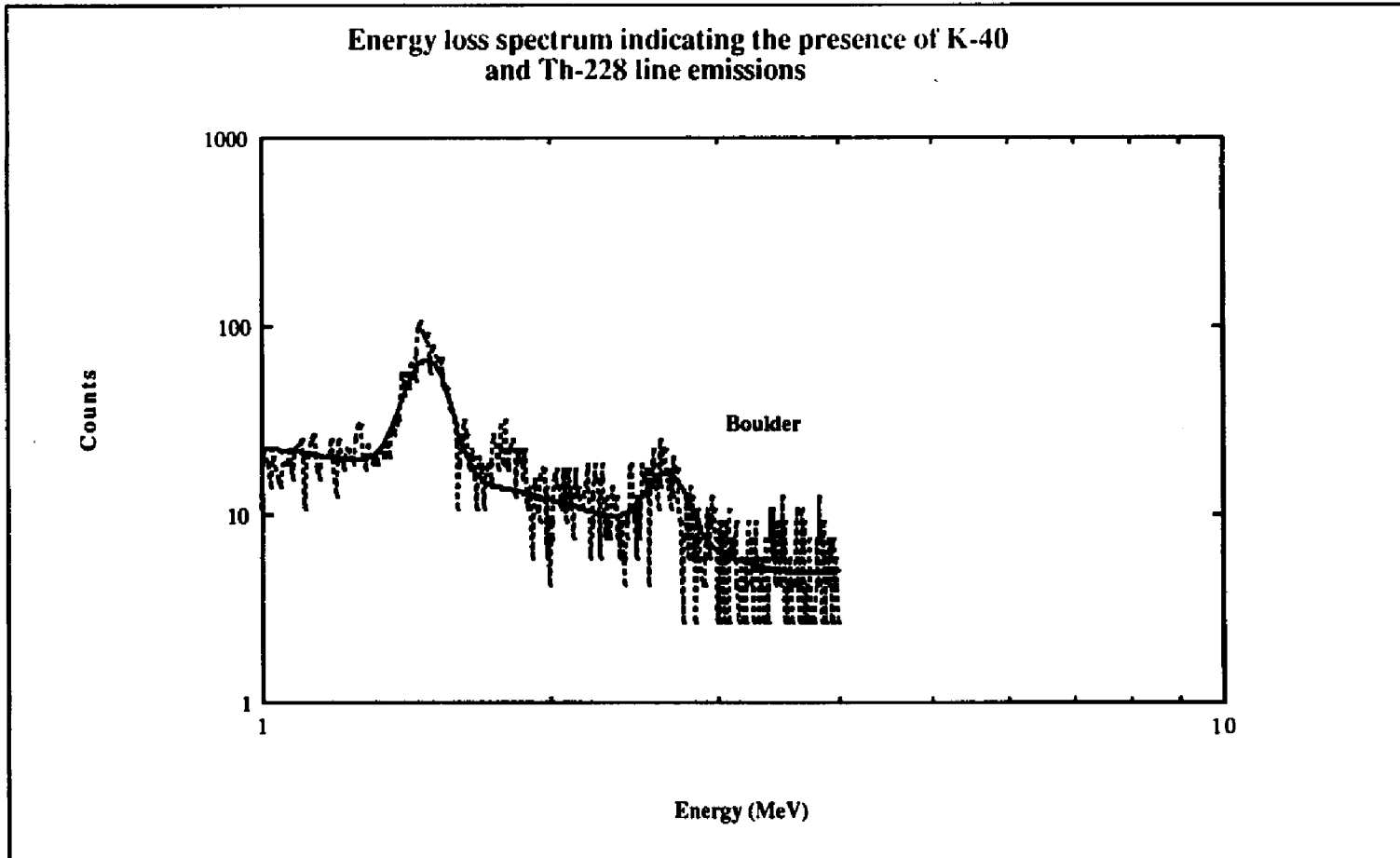


Fig. 4-12 : The energy loss spectrum corresponding to the downward TOF window is fitted using a (polynomial + gaussian) distribution

CHAPTER 5

RESULTS AND DISCUSSION

The UNH gamma ray measurements carried out deep in the atmosphere are best compared with observations of the University of California, Riverside (UCR) (Ryan *et al.*, 1979, Radwin 1978) and those of Schönfelder and Lichti (1975) of the Max Planck Institute (MPI). In all these cases it was possible to determine the directional gamma ray flux. The most comprehensive set of observations on atmospheric gamma rays was by Ryan *et al.* (1979) for various zenith angles and atmospheric depths ranging from sea level to the top of the atmosphere. Measurements of the atmospheric gamma ray flux were carried out during the ascending phase of a balloon launch of the UCR double scatter Compton telescope from Palestine, Texas on May 13th 1975. The sea level measurements were carried out at Riverside, California on July 2nd 1977 (Radwin, 1978; Ryan *et al.*, 1979). The telescope provided significant reduction of background events and clear identification of upward and downward moving gamma ray events in the energy range of 2-25 MeV. Contributions from neutron induced events is significant at float altitudes but deeper in the atmosphere the contribution is small. Hence, no correction was applied to the UCR results at large depths. The MPI group had flown one of their early versions of a Compton telescope from Palestine, Texas. Measurements were carried out in the energy range of 1.5 -10 MeV on Feb 27, 1973 during the ascent of the balloon. The telescope could not separate neutron from gamma induced events. The neutron contribution was estimated using the calculations of White and Schönfelder (1975). Results on vertical atmospheric gamma ray intensities in the 1-10 MeV range have been published for depths of 600 g-cm⁻² and above. Our results are also compared with theoretical calculations by Daniel and Stephens (1974) Morris (1984) at large atmospheric depths.

Angular distribution

The UNH results are restricted to the energy range of 1-6 MeV and zenith angles of 10-40 degrees. The differential gamma ray flux (ph/cm²-s-sr-MeV) in the vertical direction (zenith angle = 0°) at any given atmospheric depth is determined by extrapolating the measured angular distribution in the 10°-40° interval to 0° (Figure 5-1). This approach is necessary in Compton telescopes due to the uncertainty in efficiency estimates at very small scatter angles. In Figure 5-1, the 1-2 MeV bin has not been corrected for K⁴⁰ and the 2-3 MeV bin for that of Th²²⁸. Data from these two energy bins were not used in the determination of the angle dependence. At the top of the atmosphere measurements by Ryan *et al.* (1979) indicate an increasing gamma ray flux towards the horizon, consistent with the predicted zenith angle dependence of various models (Morris 1984, Graser and Schönfelder, 1977, Thompson 1974). At larger zenith angles, the primary cosmic rays incident on the top of the atmosphere traverse greater depths and hence, the secondary gamma ray emission near the top increases towards the horizon. However, our measurements at large residual atmospheric depths, show the differential intensity decreasing with increasing zenith angles (Figure 5-2). Using a $\cos^n \theta$ function for the angular dependence, we found $n \approx 2.8 \pm 0.13$ for the higher altitudes of Leadville and Mt. Washington and $n \approx 2.0 \pm 0.27$ for the lower altitudes of Boulder and Durham (Table 5-1). This is in contrast to the $\sec \theta$ dependence reported by Ryan *et al.* (1979) at 820 g-cm⁻² and by Radwin (1978) for sea level. The low energy gamma rays at large residual depths arise primarily from bremsstrahlung of electrons and positrons which are the result of muon decay. The angular dependence observed deep in the atmosphere can be compared to the dependence observed for muons and electrons. Beedle (1970) carried out a study of low energy electron component of cosmic rays and found a $\cos^2 \theta$ zenith angle dependence at sea level. In a review of various experiments, Thompson (1973) reports that muons tend to obey a $\cos^2 \theta$ dependence at sea level. Charakhch'yan *et al.* (1975) measured a $\cos^n \theta$

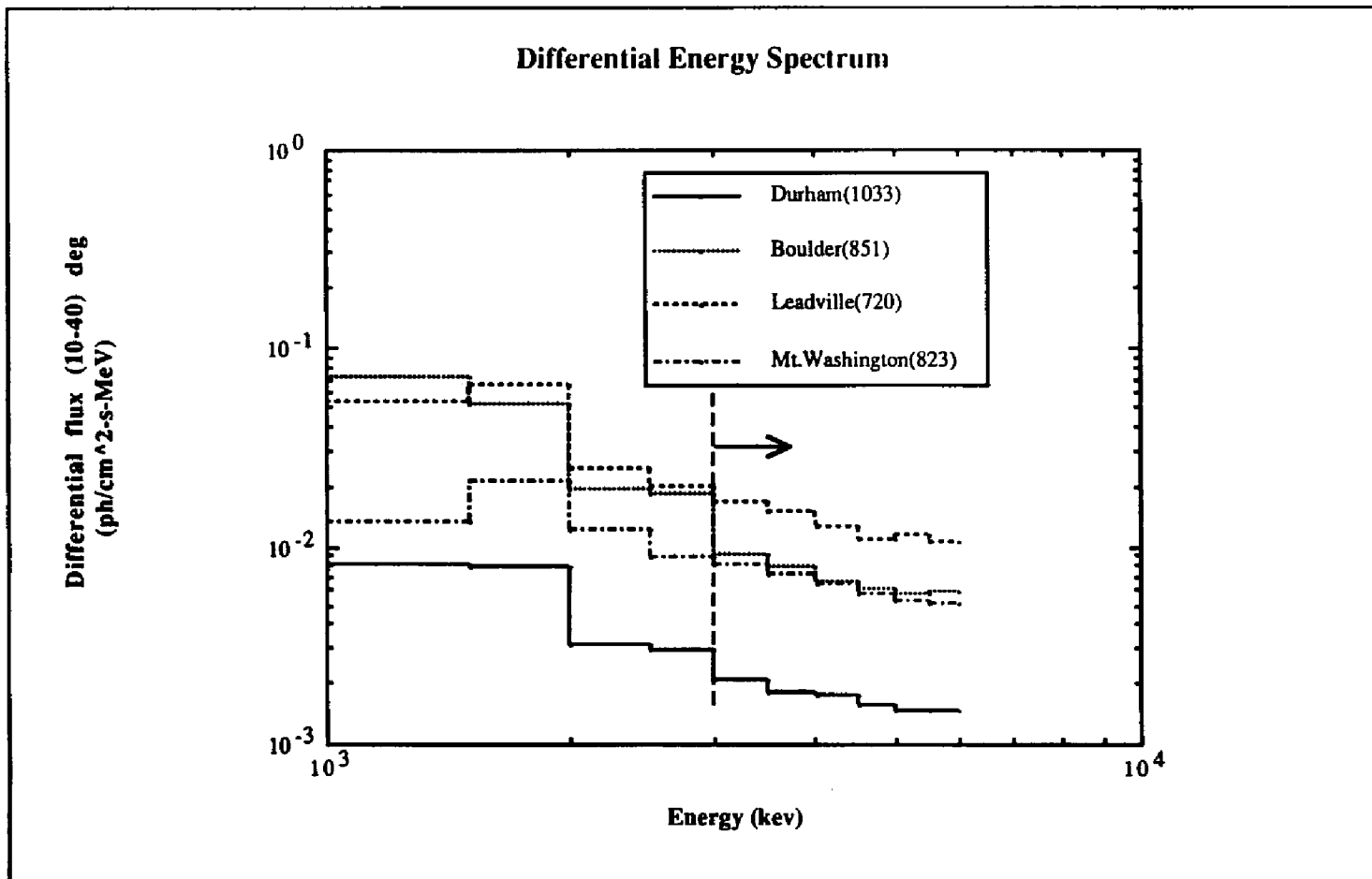


Fig. 5-1 : Flux integrated over (10-40) degrees uncorrected for K-40 (1-2) MeV and Th-228 (2-3) MeV.

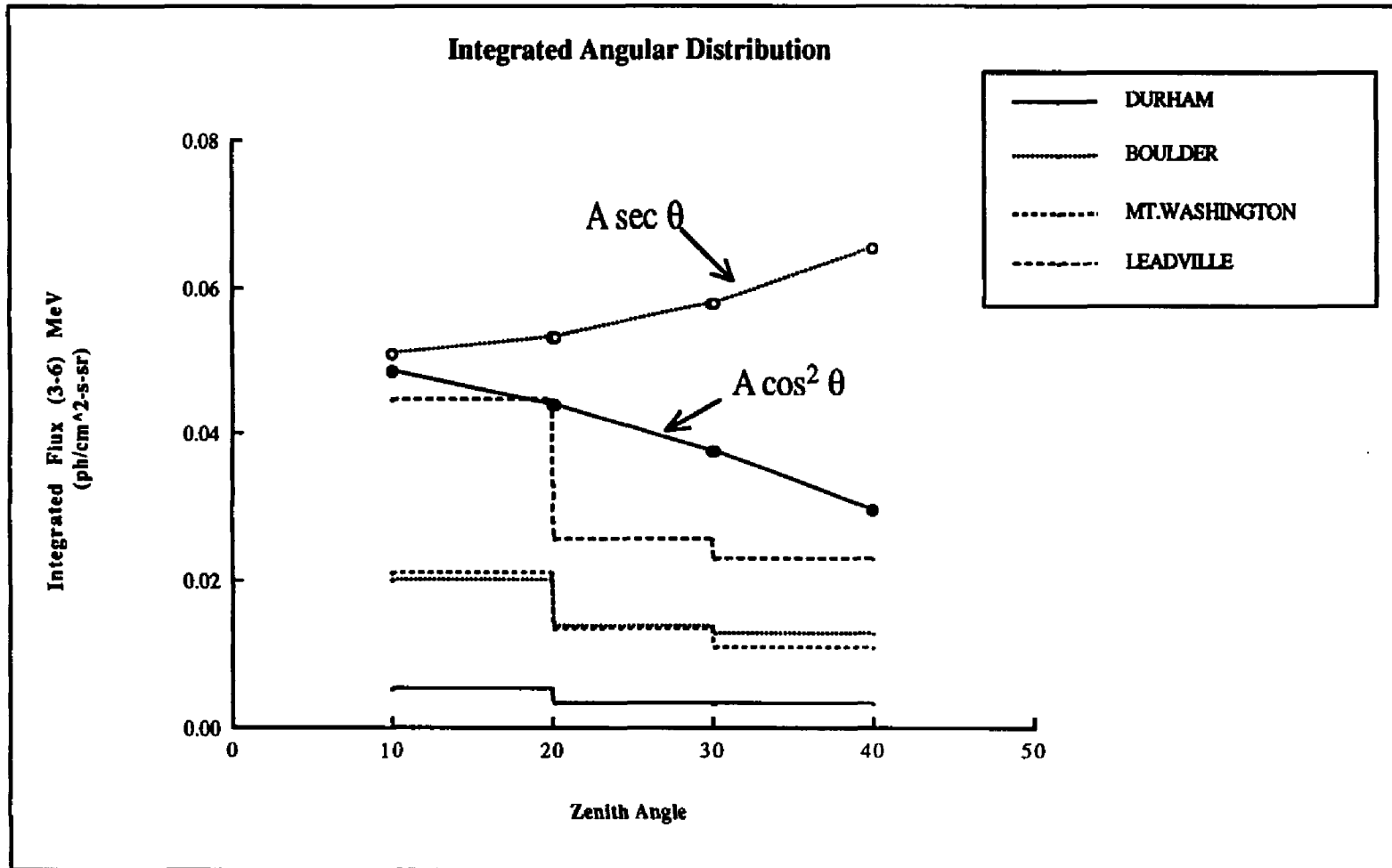


Fig. 5-2: Zenith angle dependence ($\cos^2 \theta$) in the 3-6 MeV range. These can be compared with $\cos^2 \theta$ and $\sec \theta$ distributions (scale factor $A = .05$)

dependence for muons with $n = 2$ and for the case of electrons with energy greater than 5 MeV, they found $n > 2$ because of small contributions from the π^0 decay process. Takahashi (1979) reports secondary cosmic ray measurements from an airplane and found a $\cos^n \theta$ dependence where $n = 2.0$ in the lower atmosphere and Staib *et al.* (1974) used a cosine series expansion $\sum a_n \cos n\theta$ to fit the high energy gamma ray measurements above 50 MeV which is steeper than $\cos \theta$ for $n > 1$. Thus, the observed zenith angle dependence indicated by our data for low energy gamma rays agrees with that of related secondary particles at large atmospheric depths. It can be concluded that the $\cos^n \theta$ dependence where n lies in the range of 2-3 is a good fit to the low energy gamma rays at atmospheric depths below 700 g-cm^{-2} .

Table 5-1

Variation of exponent 'n' of $\cos^n \theta$ angular distribution as a function of atmospheric depth.

Atmos. Depth (g-cm^{-2})	Location	Rigidity (GV)*	Exponent (n)**
720	Leadville	2.97	$2.89 \pm .13$
823	Mt. Washington	1.43	$2.84 \pm .10$
851	Boulder	2.90	$1.97 \pm .14$
1033	Durham	1.61	$1.97 \pm .27$

* Shea and Smart (1987)

** The error in the exponent corresponds only to statistical and angular uncertainty ($\pm 5^\circ$) and does not include contribution from efficiency estimates

Vertical Intensity

The vertical intensity was determined by extrapolating the angular dependence to $\theta = 0^\circ$ (Figure 5-3). The sea level measurements at Riverside (5.4 GV) by Ryan *et al.* (1979) are $\approx 7\%$ lower than our sea level measurements at Durham (1.5 GV). This can be understood in the light of the lower cutoff rigidity at Durham (Figure 5-4). The measurements at Boulder (851 g-cm⁻², 2.9 GV) and at Mt.Washington (823 g-cm⁻², 1.4 GV) are in good agreement with the measurements of Ryan *et al.* (1979) at Palestine, Texas (820 g-cm⁻², 4.5 GV). Power law fits were constructed using the least square technique. The indices at various locations are given in Table 5-2.

Table 5-2

$$I \propto E^{-\gamma}$$

Vertical intensity spectral index of atmospheric gamma rays at various depths

Atmos. Depth (g-cm ⁻²)	Location	Rigidity (GV)	Power law Index(γ)
720	Leadville	2.9	0.87 (r=.87)
823	Mt.Washington	1.4	1.12 (r=.95)
851	Boulder	2.9	1.29 (r=.97)
1033	Durham	1.5	1.50 (r=.99)

Table 5-2 indicates a steepening of the power law spectrum at larger depths in the atmosphere i.e., the number of photons above a certain energy decreases with depth below 700 g-cm⁻². Bezus *et al.*(1969) carried out measurements on electrons in the energy

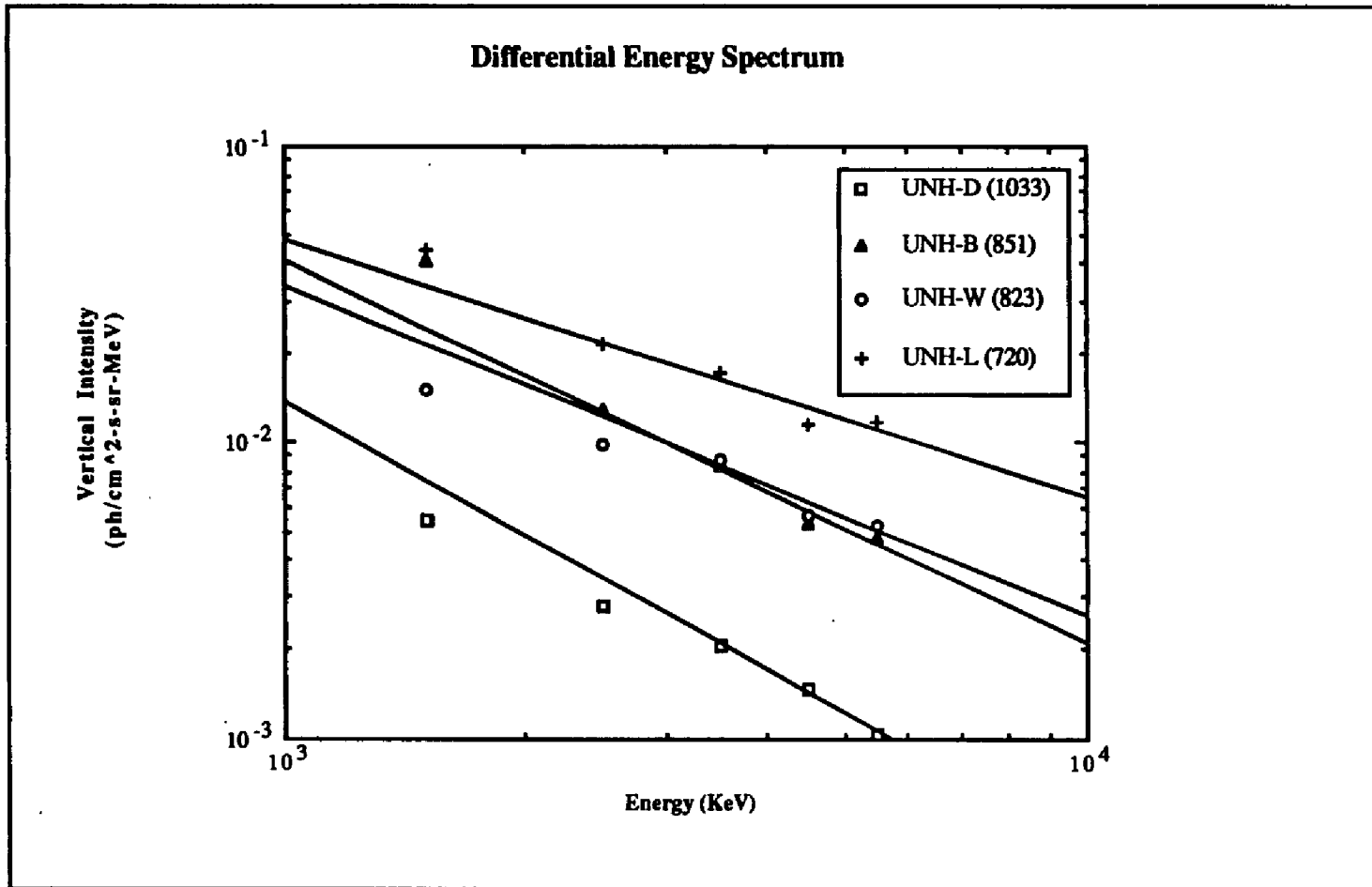


Fig. 5-3 : Vertical intensity fitted to a power law using (3-6) MeV data (ref. Table 5-2). Corrected (1-2) and (2-3) MeV bins for K-40 and Th-228.

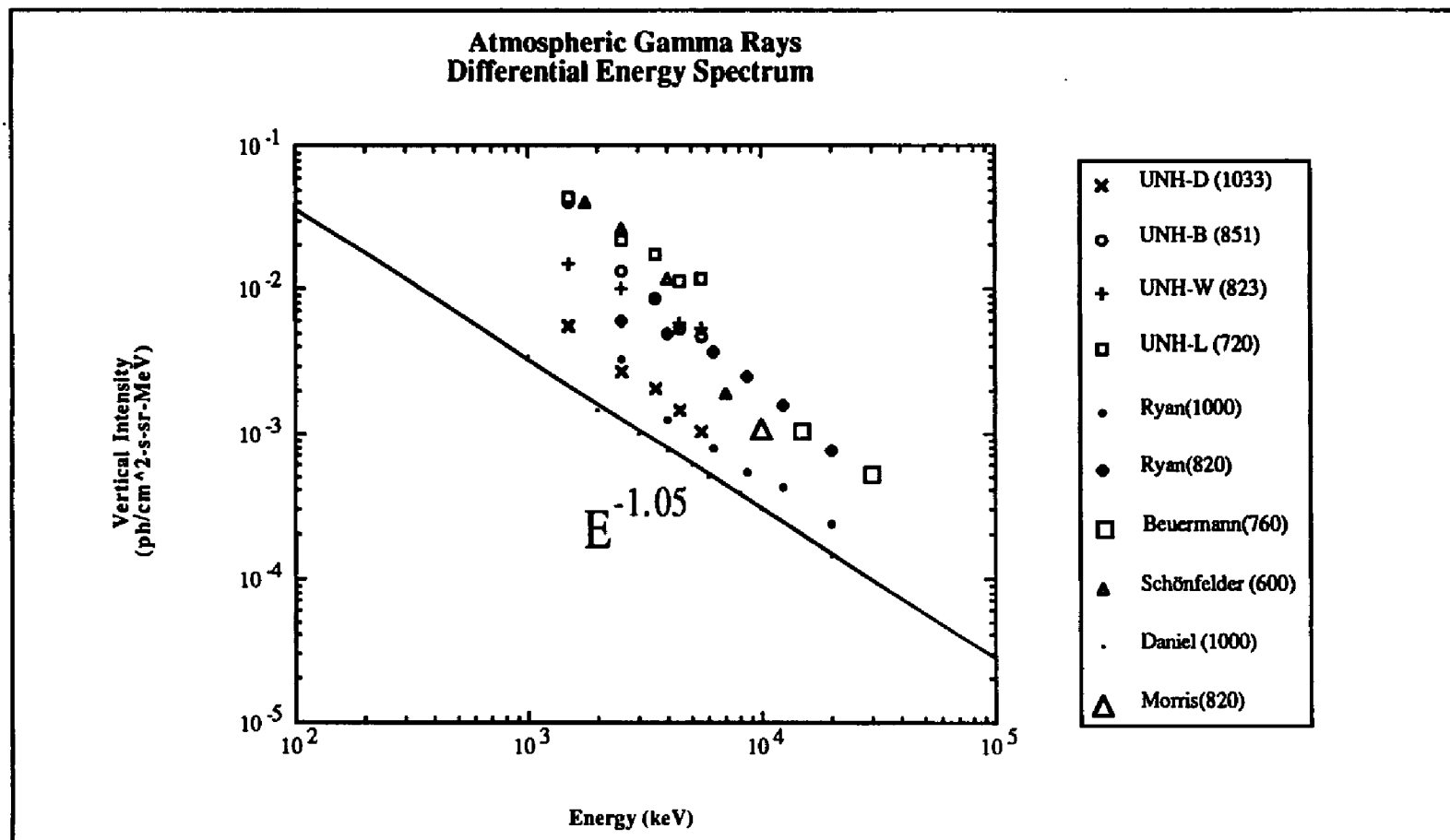
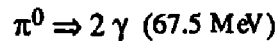
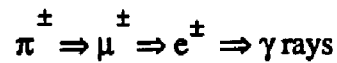


Fig. 5-4: Vertical Intensity measurements at various atmospheric depths (>600 g/cm²) are plotted together. Least square fit is drawn on calculations of Daniel et al. (1974) (1000 g-cm²).

range of 100-1500 MeV and photons of energy greater than 100 MeV. In the case of electrons, they report a steepening of the energy spectral index from 1.9 ± 0.2 at 150 g-cm^{-2} to 2.7 ± 0.3 at sea level. Since, gamma ray production at high altitudes is mainly determined by the pion decay process,



with its relative strength varying with depth, the energy spectra of electrons and photons must vary. Deeper in the atmosphere, the gamma ray production is dominated by electron bremsstrahlung resulting in spectral similarity between electrons and photons. Indeed, Beuermann and Wibberenz (1968) found good agreement between electron and photon spectra at large atmospheric depths.

Atmospheric Depth Dependence

The vertical intensity of atmospheric gamma rays varies with residual depth in the atmosphere. In the following discussion, all depths are expressed in units of g-cm^{-2} , indicating the amount of the air mass above the instrument. The UNH measurements indicate an exponential decrease in intensity with depth below 700 g-cm^{-2} . The corresponding e-folding depth is approximately 150 g-cm^{-2} (Figure 5-5). Rocchia *et al.*(1965) used an unshielded NaI gamma ray detector and obtained a mean absorption length of 170 g-cm^{-2} for depths between 200 g-cm^{-2} and 500 g-cm^{-2} , in the energy range of 0.1 to 1.5 MeV. Apparao *et al.*(1968) made omnidirectional neutron and gamma ray measurements using a CsI(Na) detector and reported an absorption mean free path of $247 \pm 25 \text{ g-cm}^{-2}$ between 400 and 700 millibars. Ryan *et al.*(1979) reports an e-folding depth of $188 \pm 12 \text{ g-cm}^{-2}$ for photons in the energy range of 3-10 MeV and $196 \pm 10 \text{ g-cm}^{-2}$, in the

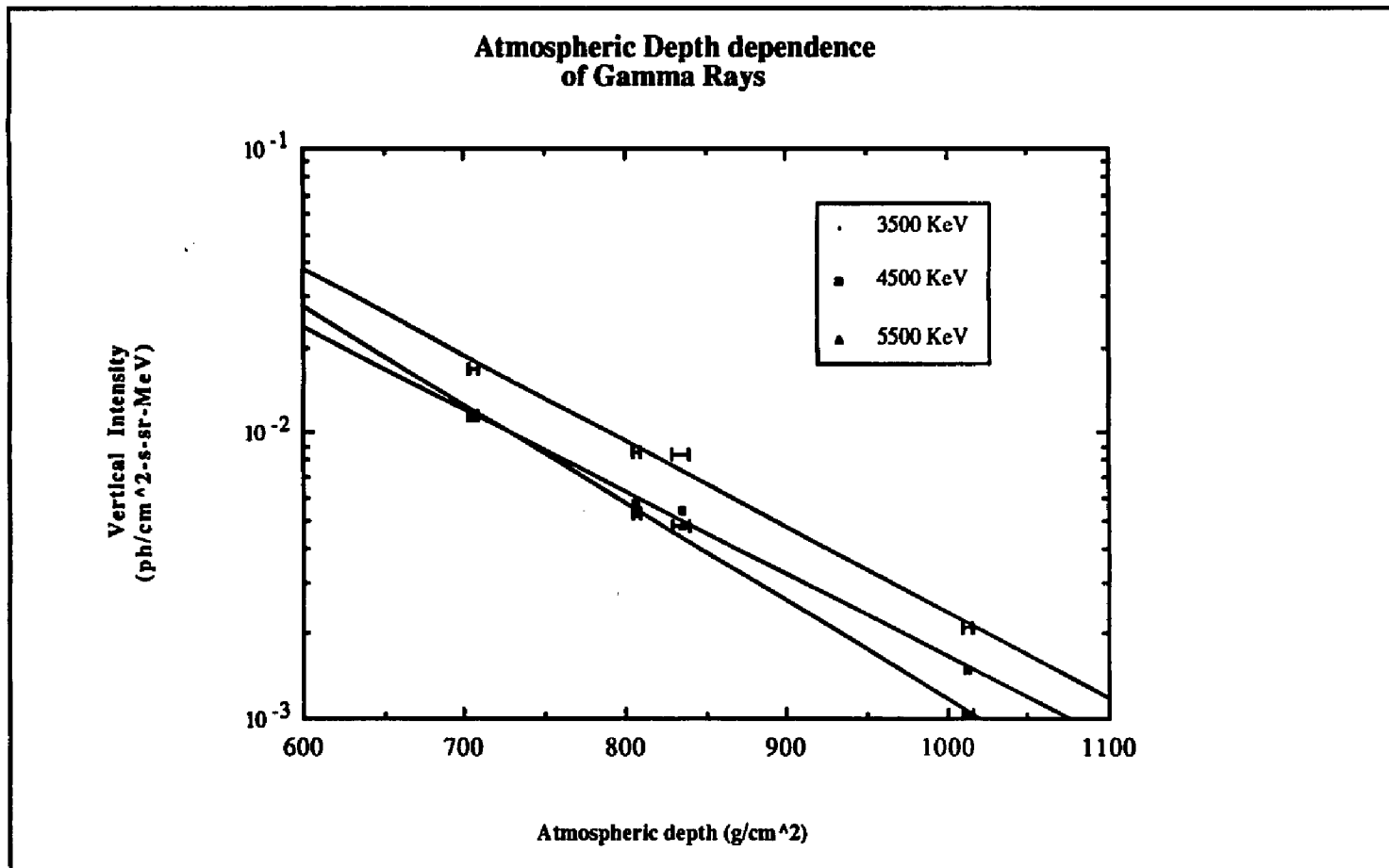


Fig.5-5 : Exponential dependence of vertical intensity on atmospheric depth.
 Attenuation mean free path (g/cm²) is 145 (3500 keV); 150 (4500 keV)
 and 127 (5500 keV)

10-25 MeV energy range. Takahashi *et al.*(1985) found that attenuation mean free path for the soft component and electrons to be $\approx 140 \text{ g-cm}^{-2}$ at a depth of 600 g-cm^{-2} , consistent with the calculations of Rossi (1948). Contributions by the various gamma ray production and attenuation processes vary with depth and energy. This will partly explain the scatter in the measured attenuation lengths at various energies and atmospheric depths. A 5 MeV gamma ray has a mean free path of $\approx 36 \text{ g-cm}^{-2}$ in air (Hubbell,1969). The measured gamma ray attenuation length L , is greater than the mean free path stated above due to generation of gamma rays from other higher energy electrons. At a depth $\lambda \text{ g-cm}^{-2}$, the intensity is given by,

$$I = I_0 e^{-\frac{\lambda}{L}}$$

$$\frac{I}{I_0} = (1 - \frac{\lambda}{L})$$

If we now introduce $f(\alpha)$, as the fraction of surviving photons which determines the difference between L and λ , then

$$f(\alpha) = (1 - \frac{\lambda}{L})$$

or

$$\frac{1}{L} = \frac{1 - f(\alpha)}{\lambda} \quad \text{..... (Hayakawa, 1969)}$$

is a function of the spectral power law index. From our observations, we conclude that the energy spectrum becomes steeper with depth. It is also clear that the gamma ray production rate is a decreasing function of depth primarily due to the decrease in the average secondary particle energy. Thus, $f(\alpha)$ is a decreasing function of depth. Hence, the measured value of gamma ray attenuation lengths at large residual depths should on the average be smaller than those measured higher up in the atmosphere. This is evident from the results presented above, where the data of Ryan *et al.*(1979) can be considered as an average over depths below the Pfozter maximum.

The variation of atmospheric gamma ray flux with atmospheric depth is shown in Figure (5-6) (courtesy J.M.Ryan, 1978). The intensity at the top of the atmosphere increases with depth down to the Pfozter maximum. Lavigne *et al.* (1984) reported a linear depth dependence of atmospheric gamma ray flux from the top of the atmosphere down to about 10 g-cm⁻². The dependence varies significantly below the Pfozter maximum in response to the decreasing contribution of primary component and the varying relative strengths of the various secondary production mechanisms. The depth dependence seen in our data can be approximated by an exponential relation with a decay constant of ≈ 153 g-cm⁻².

$$I \propto e^{-\left(\frac{\text{depth}}{153}\right)}$$

where depth is expressed in g-cm⁻² (Figure 5-5). This growth curve indicated by our data is used to normalize the vertical intensities to that at sea level. The normalization factor is given by

$$e^{-\left(\frac{1033 - \text{depth}}{153}\right)}$$

with the corrected values given by

$$I_{\text{sea level}} = I \times e^{-\left(\frac{1033 - \text{depth}}{153}\right)}$$

The above relationship is applied to the measurements of Ryan *et al.* (1979), Radwin (1978) and Schönfelder *et al.* (1977) enabling a comparison of these various depth measurements. The calculated values of Daniel and Stephens (1974) at 700, 800, 900 and 1000 g-cm⁻² along with Morris (1984) estimates at 10 MeV and 820 g-cm⁻² were also normalized to sea level using the above relation. These results are plotted in Figure 5-7. It shows reasonable agreement among the various datasets with a relatively narrow spread indicating proper scaling of the datasets. The finite spread is a result of the uncertainties

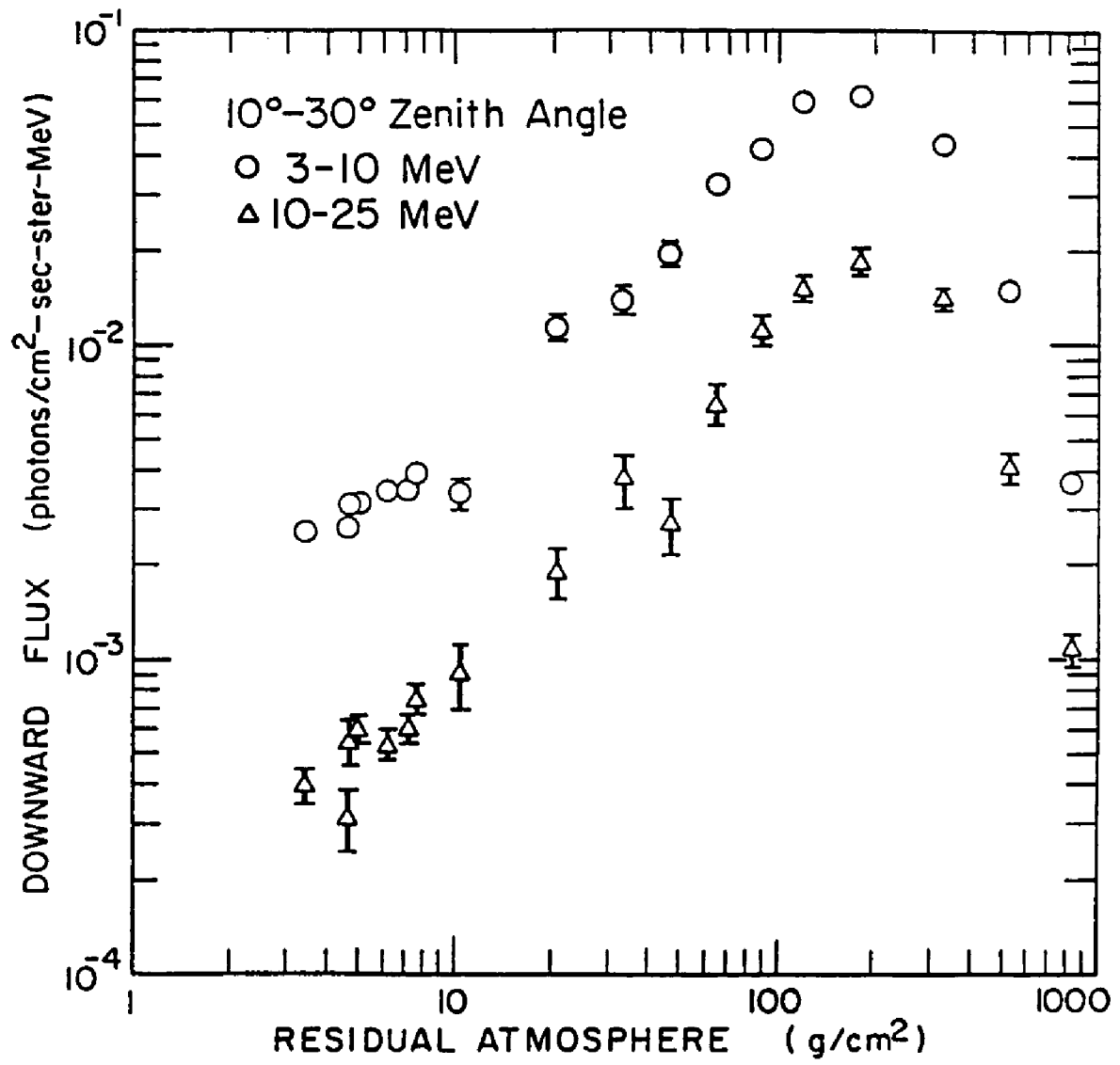


Fig. 5-6 : Integrated downward moving gamma ray flux growth curve (reproduced with permission from J.M.Ryan, 1978)

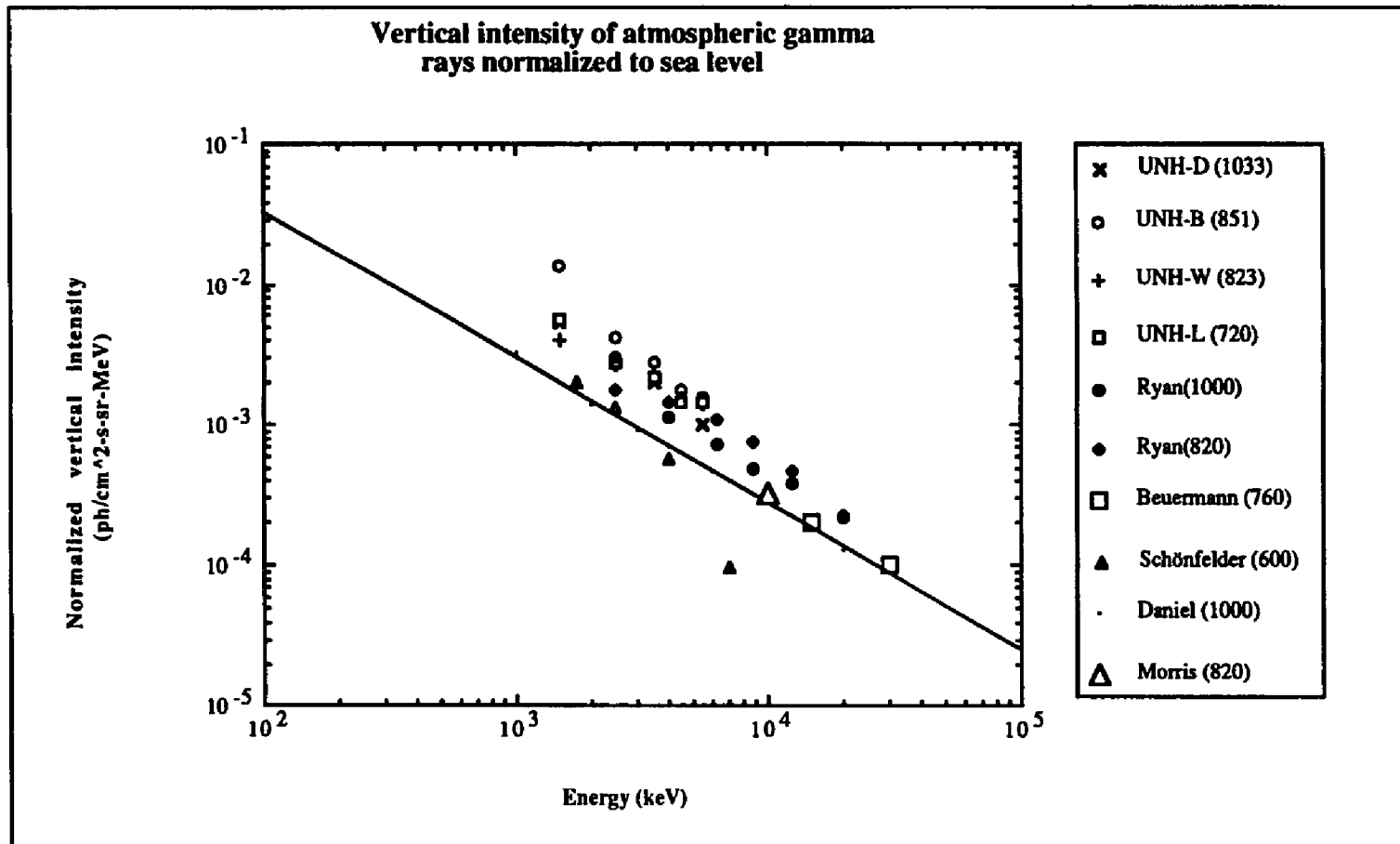


Fig. 5-7 : Vertical intensity measurements normalized to sea level. The least square fit is carried out only on calculations of Daniel et al.,(1974) at 1000 g/cm².

associated with each measurement, error associated with the normalization factor and rigidity dependence of the various datasets. The results of the MPI group (Schönfelder and Lichti, 1975) clearly seem to deviate from the rest of the observations at higher energies. This is most certainly due to the overcompensation of the original photon spectrum for neutron induced events that escape the event selection criterion (Schönfelder *et al.*, 1980). The neutron induced event contribution is based on the calculations of White and Schönfelder (1975). The early designs of the MPI Compton telescopes did not have the pulse shape discrimination feature which can reduce the neutron induced contribution. The measurements of Ryan *et al.* (1979) at 520 g-cm^{-2} and the results from the semi-empirical calculations of Ling (1975) at 520 g-cm^{-2} were also reduced to sea level using our normalisation factor. As expected, there is considerable deviation from the rest of the lower altitude values. This clearly points to the fact that the depth dependence relation based on UNH measurements is limited to depths below 700 g-cm^{-2} . Further, the calculations of Ling (1975) are based on the assumption of an isotropic gamma ray source function. This is not an appropriate assumption.

It is important to point out that these measurements do not completely agree with existing calculations. In Figure 5-8, data points corresponding to all measured values of normalized vertical intensity are compared with those calculated by Daniel and Stephens (1974) and Morris (1984). Least square fits on the calculated and measured data yield power law exponents of 1.0 and 1.3 respectively. In the energy range of 1-10 MeV there are a large number of nuclear line emissions from excited nitrogen and oxygen nuclei (Peterson *et al.*, 1973). Letaw *et al.* (1986) reported relative line intensities at the top of the atmosphere from the SMM satellite observations but measurements deeper in the atmosphere are not available. These line contributions are predicted to be small but they could partially explain the increase in the experimental values over the theoretical predictions.

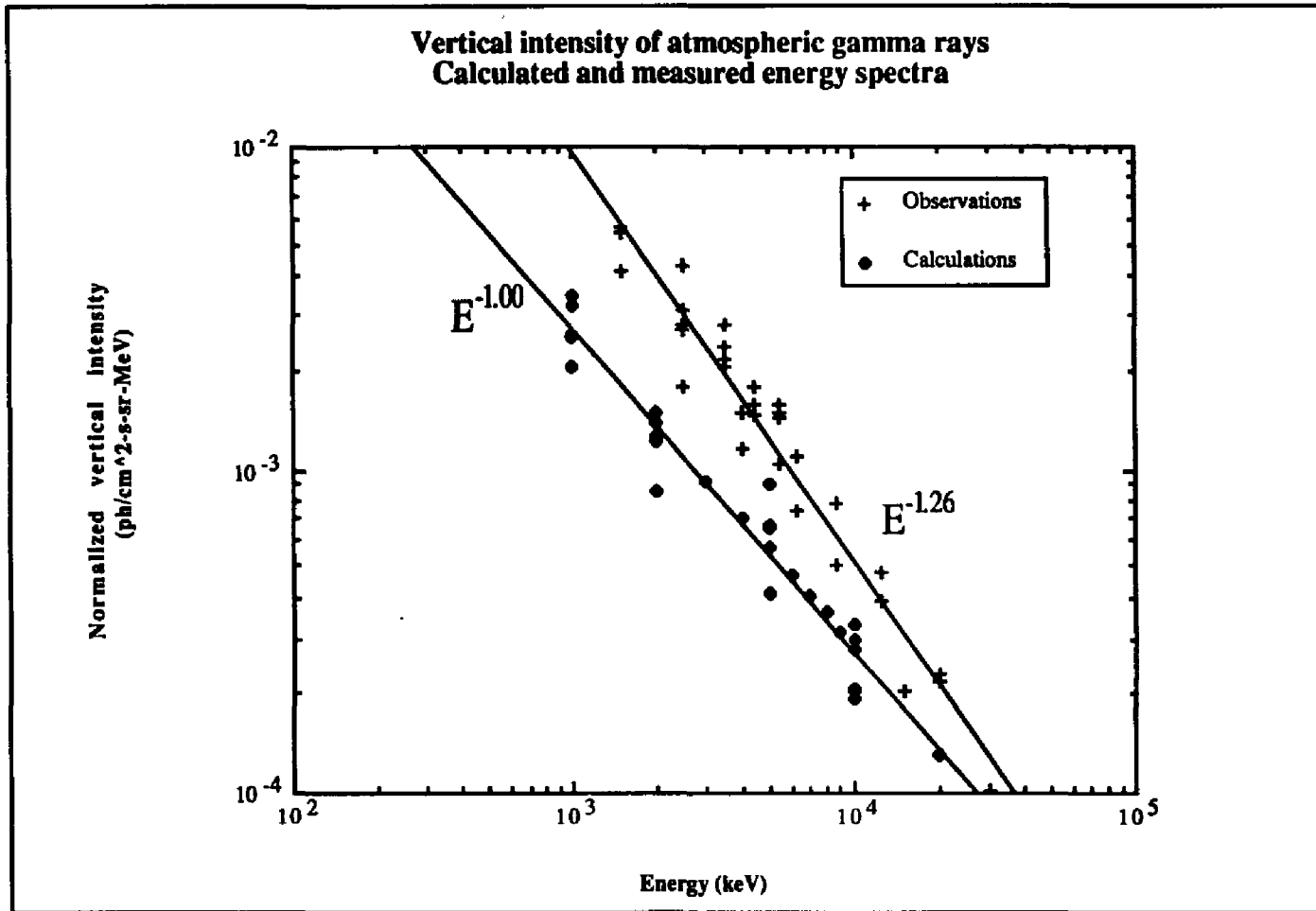


Fig. 5-8 : Comparing normalized vertical intensity measurements (UNH, Ryan, Beuermann) with calculations (Daniel, Morris)

Rigidity Dependence

It was stated earlier that the finite spread in the normalized values from different experiments might be due to the variations in cutoff rigidity amongst them. In the 3-5 MeV range where data from Ryan *et al.*(1979), Radwin (1978) and UNH measurements overlap, the rigidity dependence of the normalized flux is examined. The rigidity range over values of 1.4 GV at Mt.Washington to 5.4 GV at Riverside. This is a narrow range but sufficient to provide indications of rigidity dependence at large atmospheric depths. Figure 5-9 shows a plot of normalized vertical intensity as a function of local cutoff rigidity. The UNH measurements alone do not indicate any clear dependence on cutoff rigidity but combined with the other data from the UCR experiment, one can conclude that there is an indication of a rigidity dependence at sea level. The flux increases with decreasing cutoff rigidity consistent with the behaviour of the primary cosmic ray flux at the top of the atmosphere. These sea level measurements were conducted during times of differing solar activity. Fluctuations in primary cosmic ray intensity could contribute to the observed rigidity dependence. The variation between primary cosmic ray intensities during 1987, 1977 and 1975 were examined using ground based neutron monitor readings at Mt.Washington, NH (Lockwood, private communication). It was concluded that the variations during observation times were within 5% of the average and hence, determined to be not significant.

The variation of atmospheric gamma ray flux with cutoff rigidity has been conducted by numerous groups at balloon altitudes and at satellite orbits. Golenetskiy *et al.*(1975) obtained atmospheric gamma ray emission flux measurements from the Kosmos 461 satellite in the energy range of 28 keV to 4.1 MeV over a rigidity range of 3-17.5 GV. They observed a rigidity dependence of flux given by

$$F_{\gamma}(E,R) = A(E) f(R)$$

where $f(R) = (0.046 \pm 0.017) + e^{-\frac{R}{8.5}}$

With increasing atmospheric depth the secondary particles retain less and less of the primary information. Beyond the Pfozter maximum, much of this information is lost. The primary cosmic ray flux increases with decreasing rigidity or increasing latitude due to the lower momentum threshold imposed on the particles. There is a corresponding increase in the secondary particle flux at higher latitudes. Numerous observations have confirmed this dependence at various depths in the atmosphere. Neutron flux measurements by Potgieter *et al.*(1979) indicate decreasing rigidity dependence with increasing residual depth. Comparing our results with measured rigidity dependence of neutron count rate at sea level (Potgieter *et al.*, 1979), it is clear that the gamma ray data indicate a much weaker dependence (Figure 5-9). Nevertheless, it is interesting to note that our inferred normalized gamma ray flux at sea level along with data of Ryan *et al.*(1979), seem to indicate a weak rigidity dependence even at such large depths. Unfortunately, the UNH measurements were not conducted at locations varying widely in cutoff rigidity but at the same atmospheric depth in order to estimate this effect more precisely. This would have eliminated the need to normalize the higher altitude values and the uncertainties arising from differences in instrument response function. It should also be pointed out that the data points in Figure 5-9 are subject to large uncertainties. The greatest amount of uncertainty arises from the estimation of the efficiency of the telescope. The overall uncertainty is determined to be $\approx 25\%$. Hence, these inferred results presented here should only be considered indicative of a weak rigidity dependence at large atmospheric depths.

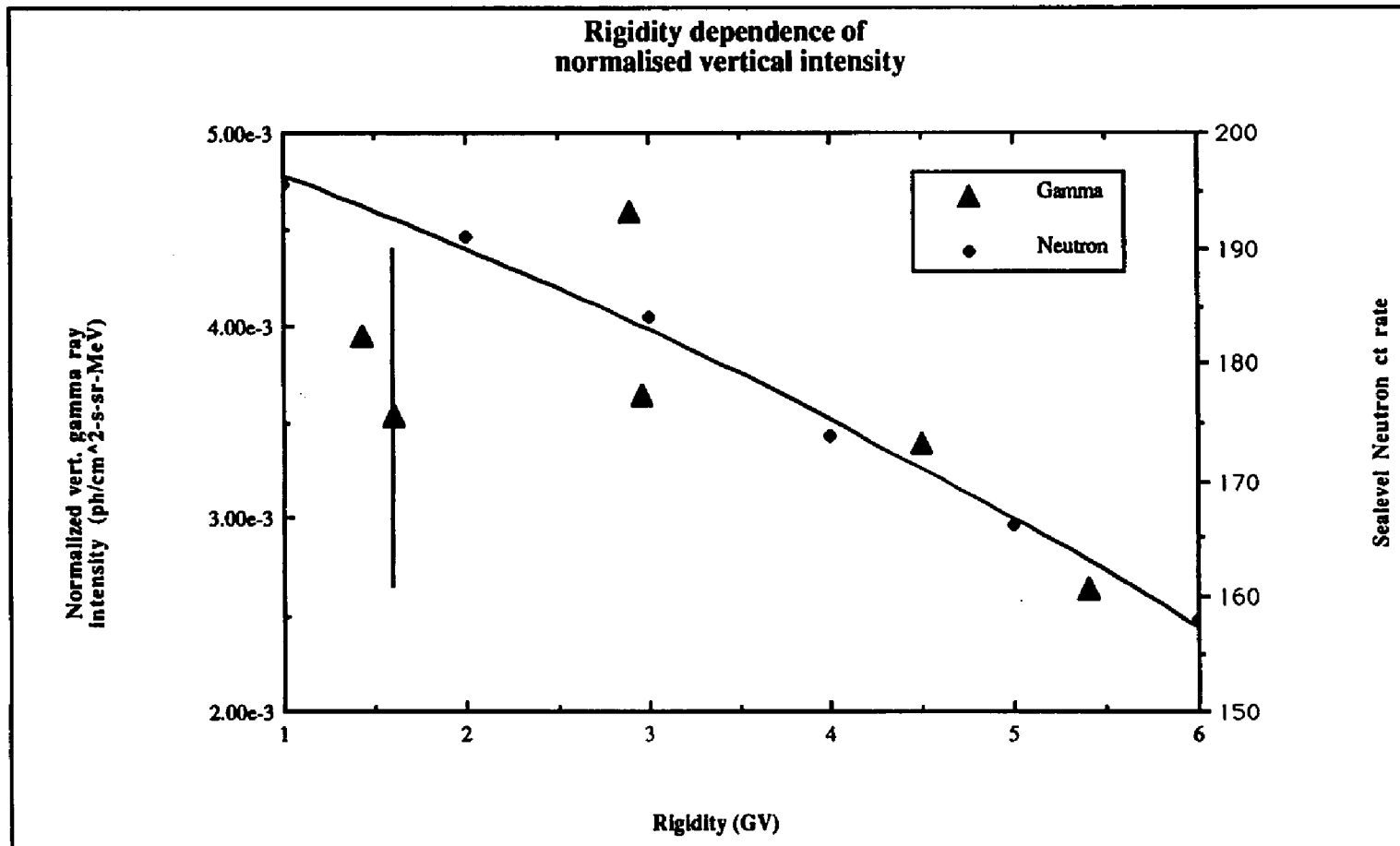


Fig. 5-9 : Observed rigidity dependence in the normalized vertical gamma ray intensity is compared with sea level neutron counting rate (Potgieter, 1979). A 25% error is indicated for UNH-Durham data point to represent uncertainty in efficiency.

CONCLUSIONS

A study has been made of atmospheric gamma rays in the energy range of 1-6 MeV at large atmospheric depths. The measurements were made using a simple Compton telescope at four locations around the country. Cosmic rays interacting with nitrogen and oxygen nuclei in the earth's atmosphere give rise to these low energy gamma rays. The primary source of low energy gamma rays at large atmospheric depths are considered to be bremsstrahlung of muon-decay electrons.

Measurements were carried out during 1987 at four locations, viz., Leadville (720 g/cm²), Mt. Washington (823 g/cm²), Boulder (851 g/cm²) and Durham (1033 g/cm²). The telescope was placed within temperature controlled enclosures and data were collected over a two week period at each location. Calibration runs were periodically conducted to monitor the overall system gain variations.

The event selection criterion imposed on the data during analysis provided downward moving events incident within a zenith angle range of 10⁰-40⁰. Above 7 MeV, contributions from slow muons that stop in the lower NaI(Tl) detector and do not get rejected are significant. Hence, the data are restricted to a range of 1-6 MeV. The angular distribution is binned into three bins of 10⁰ each. The differential flux follows a cosⁿ θ angle dependence with n = 2.8 at the higher altitudes of Leadville and Mt. Washington and with n = 2.0 at the lower elevations of Boulder and Durham. This conflicts with the sec θ dependence observed by Ryan *et al.* (1979) at a depth of 820 g/cm². Our observations which show a decreasing flux at larger zenith angles are consistent with high energy gamma ray, electron and muon angular distributions observed at sea level. This indicates good coupling between the electron, muon and gamma ray components at large residual depths in the atmosphere.

The vertical differential intensity is determined by interpolating the angle distribution to $\theta=0^\circ$. Our measurements agree well with those of Ryan *et al.* (1979) at sea level and 820 g/cm^2 which were also made using a Compton telescope. All these measurements lie above the theoretical calculation of Daniel *et al.* (1974). Our measurements yield a power law spectrum of index about unity with the spectrum steepening with increasing atmospheric depth.

Our observation sites range in atmospheric depth from $700 - 1000 \text{ g/cm}^2$ and $1.4 - 2.9 \text{ GV}$ in rigidity. The measured vertical intensity variation over atmospheric depths is used to determine the atmospheric depth dependence of low energy gamma rays in the lower atmosphere. The attenuation mean free path is found to be $\approx 153 \text{ g/cm}^2$ and the vertical intensity was found to be proportional to $\exp^{-(\text{depth}/153)}$. This allows normalization of fluxes at different depths ($> 600 \text{ g/cm}^2$) to sea level values. General agreement is found among the various experiments. Differences between our normalized vertical intensities at different locations are attributed to possible rigidity dependence in the data. Together with measurements from the University of California, Riverside group, our results indicate only a weak rigidity dependence considering the large uncertainties involved with the normalized dataset.

The normalization of all available experimental and theoretical data, including Monte Carlo simulation results, indicate that the experimental data tend to exhibit a steeper power law spectrum than the calculations. In the energy range of $1-10 \text{ MeV}$ there are a large number of nuclear line emissions from excited nitrogen and oxygen nuclei (Peterson *et al.*, 1973; Letaw *et al.*, 1986). These line contributions are predicted to be small but they could partially explain the increase in the experimental values over the theoretical predictions.

Our understanding of cosmic ray interactions in the atmosphere would be enhanced by more detailed and reliable measurements of the various secondary and primary particles

over all energies, angles and atmospheric depths. There have been extensive measurements in the upper atmosphere from balloon-borne experiments while the measurements in the lower atmosphere have been limited. The results presented here strengthen the observational data of low energy gamma rays at large atmospheric depths. Comparison with the limited calculations and simulations that are available indicate a need for further refinements in the atmospheric gamma ray production and propagation models. Our results from a statistically rich dataset should be valuable in achieving a better model. Additional work needs to be done in determining the evolution of the gamma ray angular distribution with energy and atmospheric depth along with similar measurements on secondary electrons to understand the strong coupling existing between electrons and photons. These should be available in the coming years with the help of improved gamma ray instruments.

REFERENCES

- Apparao, M.V.K., R.R.Daniel, G.Joseph, G.S.Gokhale, P.J.Lavakare and R.Sunderrajan, Gamma rays and high energy neutrons in the atmosphere, *Can. J. Phys.*, 46, S1030 (1968)
- Beedle, R.E., A study of the low energy electron component of the cosmic radiation, *UNH-10-14*, University of New Hampshire, Durham, NH (1970)
- Beuermann, K.P., Secondary electron and photons in the upper atmosphere, *J. Geophys. Res.*, 76, 4291 (1971)
- Beuermann, K.P. and G.Wibberenz, Secondary spectra of electrons and photons in the atmosphere, *Can. J. Phys.*, 46, S1034 (1968)
- Bezus, V.A., A.M.Galper, V.V.Dmitrenko, V.G.Kirillov-Ugryumov, B.I.Luchkov, Yu.V.Ozerov, I.L.Rozental, E.M.Shermanzon, N.L.Grigorov, L.F.Kalinkin, A.S.Melioransky and I.A.Savenko, Measurement of the spectra of cosmic ray electrons and photons at different altitudes in the atmosphere, *Proc. Int. Cosmic Ray Conf. (Budapest)*, MQ-123, 761 (1969)
- Birks, J.B., The theory and practice of scintillation counting, *Pergamon Press* (1964)
- Chupp, E.L., A.A.Sarkady and H.P.Gilman, The 0.5 MeV gamma ray flux and the energy loss spectrum in CsI(Tl) at 4 g/cm², *Planet. Space Sci.*, 18, 939 (1970)
- Charakhch'yan, A.N., G.A.Bazilevskaya, A.F.Krasotkin and T.N.Charakhch'yan, Cosmic-ray intensity in the near-earth atmosphere and at the surface of the earth, *Geomag. Aeronomy*, 15, 164 (1975)
- Daniel ,R.R. and S.A.Stephens, Cosmic electrons and related astrophysics, *Space Sci. Rev.*, 10, 599 (1970)
- Daniel ,R.R. and S.A.Stephens, Cosmic ray produced electrons and gamma rays in the atmosphere, *Rev. Geophys. Space Phys.*, 12, 233 (1974)
- Dietze,G. and H.Klein, Gamma calibration of NE213 scintillation counters, *Nucl. Instr. Meth.*, 193, 549 (1982)
- Evans, R.D., The atomic nucleus, *McGraw-Hill Book Company*, (1955)
- Fichtel, C.E., D.A.Kniffen and H.B.Ogelman, Results of gamma-ray balloon astronomy, *Astrophys. J.*, 158, 193 (1869)
- Fishman, G.J., J.W.Watts, JR., and C.A.Meegan, Observation of a North-South anisotropy of atmospheric radiation at balloon altitudes, *J. Geophys. Res.*, 81, 6121 (1976)
- Graser, U. and V.Schönfelder, Theoretical zenith angle distribution of atmospheric MeV gamma radiation at high balloon altitude, *J. Geophys. Res.*, 82, 1055 (1977)

- Golenetskiy, S.V., Yu.A.Gur'yan, V.N.II'inskiy, Ye.P.Mazets and M.P.Proskura, Gamma emission of the atmosphere in the vicinity of the earth, *Geomag. Aeronomy*, 15, 169 (1975)
- Hayakawa, S., Cosmic ray physics: Nuclear and astrophysical aspects, John Wiley & Sons, (1969)
- Herzo, D., R.Koga, W.A.Millard, S.Moon, J.Ryan, R.Wilson, A.D.Zych and R.S.White, A large double scatter telescope for gamma rays and neutrons, *Nucl. Instr. Meth.*, 123, 583 (1975)
- Hillier, R., Gamma ray astronomy, *Clarendon Press, Oxford* (1984)
- Hubbell, J.H., Photon cross sections, attenuation coefficients and energy absorption coefficients from 10 keV to 100 GeV, *NSRDS-NBS*, 29, (1969)
- Kasturirangan, K., U.R.Rao and P.D.Bhavsar, Low energy atmospheric gamma rays near geomagnetic equator, *Planet. Space Sci.*, 20, 1961 (1972)
- Kelley, R.L., C.P.Horne, M.J.Losty, A.Rittenberg, T.Shimada, T.G.Trippe, C.G.Wohl, G.P.Yost, N.Barsh-Schmidt, C.Bricman, C.Dionisi, M.Mazzucato, L.Montanet, R.L.Crawford, M.Roos and B.Armstrong, Review of particle properties, *Rev. Mod. Phys.*, 52, S1 (1980)
- Lavigne, J.M., M.Niel and B.Agrinier, A comparison of experimental results at 4.5 GV and 11.7 GV, *J. Geophys. Res.*, 89, 5636 (1984)
- Letaw, J.R., G.H.Share, R.L.Kinzer, R.Silberberg, E.L.Chupp, D.J.Forrest and E.Rieger, Measurement of gamma-ray line intensities from the earth's atmosphere, *Adv. Space Res.*, 6, 133 (1986)
- Ling, J.C., A semiempirical model for atmospheric gamma rays from 0.3 to 10 MeV at $\lambda = 40^\circ$, *J. Geophys. Res.*, 80, 3241 (1975)
- Morris, D.J., Production of high-energy gamma rays by cosmic ray interaction in the atmosphere and lunar surface, *J. Geophys. Res.*, 89, 10685 (1984)
- O'Neill, T.J., Gamma ray sources in the 1 to 30 MeV range, *Ph.D Thesis*, University of California at Riverside (1987)
- Paulus, T.J., Timing electronics and fast timing methods with scintillation detectors, *IEEE Trans. Nucl. Sci.*, NS-32, 1242 (1985)
- Peterson, L.E., D.A.Schwartz and J.C.Ling, Spectrum of atmospheric gamma rays to 10 MeV at $\lambda = 40^\circ$, *J. Geophys. Res.*, 78, 7942 (1973)
- Potgieter, M.S., B.C.Raubenheimer and P.H.Stoker, The latitude distribution of cosmic rays at sealevel during the recent period of minimum solar activity, *Proc. Int. Cosmic Ray Conf. (Kyoto)*, MG 9-7, 352 (1979)
- Puskin, J.S., Low-energy gamma rays in the atmosphere, *Res. Sp. Sci., SAO Sp. Rpt.* 318, 1 (1970)

- Radwin, M.D., A sea-level measurement of 2-25 MeV atmospheric gamma rays, *Masters Thesis*, University of California at Riverside, (1978)
- Rocchia, R., J.Labeyrie, G.Ducros and D.Boclet, Gamma ray generation in the high atmosphere, *Proc. Int. Conf. Cosmic Rays 9th*, 423 (1965)
- Rossi, B., Interpretation of cosmic-ray phenomena, *Rev. Mod. Phys.*, 20, 537 (1948)
- Ryan, J.M., Energy and angle distributions for atmospheric and cosmic diffuse gamma rays from 2 to 25 MeV, *Ph.D Thesis*, University of California at Riverside (1978)
- Ryan, J.M., M.C.Jennings, M.D.Radwin, A.D.Zych and R.S.White, Atmospheric gamma ray angle and energy distributions from sea level to 3.5 g/cm² and 2 to 25 MeV, *J. Geophys. Res.*, 84, 5279 (1979)
- Schönfelder, V. A.Hirner and K.Schneider, A telescope for soft gamma ray astronomy, *Nucl. Instr. Meth.*, 107, 385 (1973)
- Schönfelder, V. and G.Lichti, Atmospheric vertical gamma ray flux in the MeV range, *J. Geophys. Res.*, 80, 3681 (1975)
- Schönfelder, V., U.Graser and J.Daugherty, Diffuse cosmic and atmospheric MeV gamma radiation from balloon observations, *Astrophys. J.*, 217, 306 (1977)
- Schönfelder, V., F.Graml and F.P.Penningsfeld, The vertical component of 1-20 MeV gamma rays at balloon altitudes, *Astrophys. J.*, 240, 350 (1980)
- Schönfelder, V., U.Graser and R.Diehl, Properties and performance of the MPI balloon borne Compton telescope, *Astron. Astrophys.*, 110, 138 (1982)
- Shea, M.A. and D.F.Smart, Vertical cutoff rigidities calculated using the estimated 1985 geomagnetic field coefficients, *Proc. Int. Cosmic Ray Conf., (Moscow)*, SH 8.1-5, 204 (1987)
- Staib, J.A., G.M.Frye, Jr., and A.D.Zych, The atmospheric gamma ray spectrum from 50 MeV to 1 GeV at 3 mbar for 4.5- and 12-GV cutoffs and sea level, *J.Geophys. Rev.*, 79, 929 (1974)
- Takahashi, K., Altitude variations of various cosmic-ray components observed by airborne detectors at a middle latitude region, *Proc. Int. Cosmic Ray Conf., (Kyoto)*, MG9-4, 342 (1979)
- Thompson, D.J., A three dimensional study of 30-300 MeV atmospheric gamma rays, *J. Geophys. Res.*, 79, 1309 (1974), .
- Thompson, M.G., Cosmic rays at ground level, (ed A.W.Wolfendale), 17 (1973)
- Tsoufanidis, N., Measurement and detection of radiation, McGraw-Hill Book Company, (1972)
- Vette, J.I., Low-energy gamma rays produced in air and in lead by cosmic rays, *J.Geophys. Res.*, 67, 1731 (1962)

White, R.S. and V.Schönfelder, Neutron and proton interaction backgrounds in compton-telescopes used for gamma ray astronomy, *Astrophys. Space Sci.*, 38, 19 (1975)